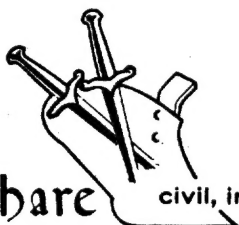


DI
PNE - 115



Plowshare

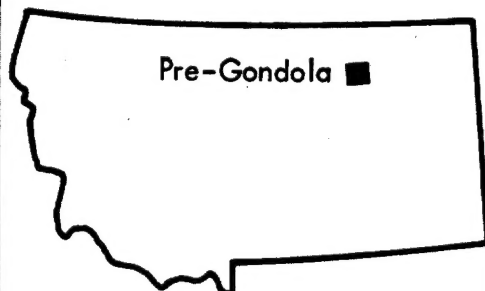


civil, industrial and scientific uses for nuclear explosives

Mr. Brown

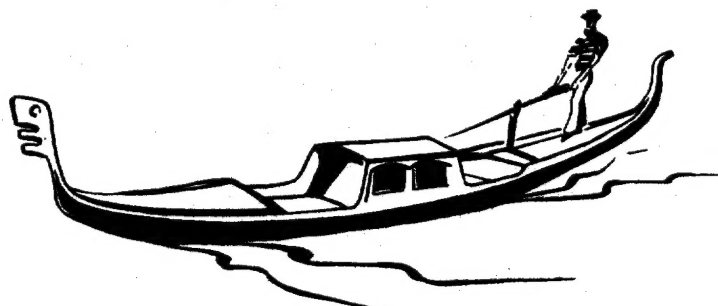
UNITED STATES ARMY CORPS OF ENGINEERS

FORT PECK RESERVOIR
MONTANA



DISTRIBUTION STATEMENT A
Approved for Public Release
Distribution Unlimited

PROJECT ***PRE-GONDOLA***



**INTERMEDIATE RANGE GROUND MOTIONS
FOR PRE-GONDOLA II AND ASSOCIATED EVENTS**

Lawrence Radiation Laboratory
Livermore, California

Reproduced From
Best Available Copy

20011105 100

ISSUED: OCTOBER 14, 1968

LEGAL NOTICE

This report was prepared as an account of Government sponsored work. Neither the United States, nor the Commission, nor any person acting on behalf of the Commission:

A. Makes any warranty or representation, expressed or implied, with respect to the accuracy, completeness, or usefulness of the information contained in this report, or that the use of any information, apparatus, method, or process disclosed in this report may not infringe privately owned rights; or

B. Assumes any liabilities with respect to the use of, or for damages resulting from the use of any information, apparatus, method, or process disclosed in this report.

As used in the above, "person acting on behalf of the Commission" includes any employee or contractor of the Commission, or employee of such contractor, to the extent that such employee or contractor of the Commission, or employee of such contractor prepares, disseminates, or provides access to, any information pursuant to his employment or contract with the Commission, or his employment with such contractor.

This report has been reproduced directly from the best available copy.

Printed in USA. Price \$3.00. Available from the Clearinghouse for Federal Scientific and Technical Information, National Bureau of Standards, U. S. Department of Commerce, Springfield, Virginia 22151.

PNE-1115

NUCLEAR EXPLOSIONS-PEACEFUL
APPLICATIONS (TID-4500)

INTERMEDIATE RANGE GROUND MOTIONS FOR PRE-GONDOLA II AND ASSOCIATED EVENTS

Dean V. Power

Lawrence Radiation Laboratory
Livermore, California

April 1968

This report has been issued as UCRL-50433.

Acknowledgments

The author wishes to express his gratitude to all those who contributed to this effort. In particular, the efforts of John Lane (Mechanical Engineering), Kenneth Olsen (Electronics Engineering), and Thomas Tami (Nuclear Cratering Group) are gratefully acknowledged.

Abstract

Ground motion records from seven high explosive cratering events in northeastern Montana were analyzed for peak velocity, power spectral density, and velocity spectra. The events included four 20-ton single charges at depths of burst which varied from 42 to 57 ft, a 140-ton row charge consisting of three 20-ton charges and two 40-ton charges at optimum depths of burst, and a fully coupled charge of 0.5 tons and a decoupled charge of 0.5 tons at optimum depths of burst. It was found that at these depths and charge weights an increase in depth of burst resulted in an increase in peak velocities and power spectral densities as measured at distant points (>5 km), while no significant frequency shifts were noted. Power spectral density was found to be approximately proportional to the first power of yield. For this region it was determined that power spectral densities varied inversely as radius to the 3.55 power, and peak velocities varied inversely as radius to the 1.6 power. An increase in both velocities and power spectral densities for small decoupling factors was found to occur for a certain explosive-cavity configuration. Three analysis techniques, peak velocity, velocity spectra, and power spectral density, are compared and it is shown that power spectral density is the most consistent method when comparing records from different measuring stations.

Contents

| | |
|--|--------|
| ACKNOWLEDGMENTS | ii |
| ABSTRACT | iii-iv |
| INTRODUCTION | 1 |
| Description of Project Pre-Gondola II | 1 |
| Description of Events Associated with Pre-Gondola II | 3 |
| Description of Other Events Related to Pre-Gondola II | 3 |
| Objectives | 3 |
| Background | 4 |
| PROCEDURE | 6 |
| Station Selection | 6 |
| Seismic Instrumentation | 8 |
| Recording and Timing | 9 |
| Information Retrieval and Reduction | 10 |
| Data Analysis | 11 |
| RESULTS | 13 |
| Data Recovery and Reduction | 13 |
| Peak Velocity and Vector Addition | 13 |
| Comb Filter Peak Velocity | 13 |
| Power Spectral Density | 23 |
| ANALYSIS OF RESULTS, DISCUSSION, AND INTERPRETATION | 56 |
| Time History Variances | 56 |
| Velocity in the Frequency Domain | 57 |
| Power Spectral Density and Seismic Energy | 58 |
| CONCLUSIONS | 61 |
| REFERENCES | 62 |
| APPENDIX A. A Discussion of the Transmission of Seismic Signals and Their Measurement | 63 |
| APPENDIX B. A Discussion of Comb Filter Peak Velocity and Vector Addition Analysis Techniques | 65 |
| APPENDIX C. A Discussion of the Power Spectral Density Code | 67 |

Figures

| | | |
|----|---|----|
| 1 | Map showing environs of Pre-Gondola II and associated events. | 2 |
| 2 | Map showing location of free-field seismic stations for Pre-Gondola II 140-ton row charge. (Station 2BN was operated for Alfa, Charlie, Delta, and Bravo Events, and Stations 3N, 4N, and 5N were occupied on Bravo Event during Pre-Gondola series; Stations 2BN and 6W were occupied on decoupling series during Pre-Gondola II.) | 7 |
| 3 | Response of HS-10-1 velocity geophone at 35 and 70% damping. | 8 |
| 4 | Three-component instrument package during set-up and prior to insertion into outer canister (canister is partly visible behind metal drum on right). | 9 |
| 5 | Top view of tape recorder used for recording geophone signals (tape cartridge is shown in place at right). | 10 |
| 6 | Partly dismantled recorder, showing its size, portability, etc. | 11 |
| 7 | Peak velocities for Pre-Gondola I Bravo Event as a function of distance (large value at 96 km is due to single pulse of very high amplitude in velocity-time signature; rest of signature is of relatively low amplitude). | 15 |
| 8 | Peak velocities for Pre-Gondola II 140-ton row charge as a function of distance. | 15 |
| 9 | Comb filter peak velocity as a function of frequency for Station 2BN, Pre-Gondola II SD-1 Event. | 16 |
| 10 | Comb filter peak velocity as a function of frequency for Station 2BN, Pre-Gondola II SD-2 Event. | 16 |
| 11 | Comparison of comb filter peak velocities of radial motion at Station 2BN for SD-1 and SD-2 Events. | 17 |
| 12 | Comparison of comb filter peak velocities of transverse motion at Station 2BN for SD-1 and SD-2 Events. | 17 |
| 13 | Comparison of comb filter peak velocities of vertical motion at Station 2BN for SD-1 and SD-2 Events. | 18 |
| 14 | Comb filter peak velocity as a function of frequency for Station 6W, Pre-Gondola II SD-1 Event. | 18 |
| 15 | Comb filter peak velocity as a function of frequency for Station 6W, Pre-Gondola II SD-2 Event. | 19 |
| 16 | Comparison of comb filter peak velocities of radial motion at Station 6W, for SD-1 and SD-2 Events. | 19 |
| 17 | Comparison of comb filter peak velocities of transverse motion at Station 6W for SD-1 and SD-2 Events. | 20 |
| 18 | Comparison of comb filter peak velocities of vertical motion at Station 6W for SD-1 and SD-2 Events. | 20 |
| 19 | Comb filter peak velocity as a function of frequency for Station 2BN, Pre-Gondola II 140-ton row charge. | 21 |
| 20 | Comb filter peak velocity as a function of frequency for Station 3N, Pre-Gondola II 140-ton row charge. | 21 |
| 21 | Comb filter peak velocity as a function of frequency for Station 4N, Pre-Gondola II 140-ton row charge. | 22 |
| 22 | Comb filter peak velocity as a function of frequency for Station 5N, Pre-Gondola II 140-ton row charge. | 22 |

Figures (Continued)

| | | |
|----|--|----|
| 23 | Comb filter peak velocity of radial components for all stations, Pre-Gondola II 140-ton row charge. | 23 |
| 24 | Comb filter peak velocities for all stations of transverse components, Pre-Gondola II 140-ton row charge. | 24 |
| 25 | Comb filter peak velocity of vertical components for all stations, Pre-Gondola II 140-ton row charge, as a function of frequency. (Note that at low frequencies attenuation is about as expected; at high frequencies the short duration-high amplitude pulses in signals on Station 5N considerably alter the relationship of V_p vs distance.) | 25 |
| 26 | Plot of $\alpha(\text{frequency})$ from equation: $\text{CFPV}(R, f) = K_f R^{-\alpha(f)}$; this represents attenuation slope for comb filter peak velocity as a function of frequency (Pre-Gondola II). | 25 |
| 27 | Radial components at Station 2BN for three yields. | 27 |
| 28 | Transverse components at Station 2BN for three yields. | 28 |
| 29 | Vertical components at Station 2BN for three yields. | 29 |
| 30 | Resultant power spectral densities at Station 2BN for three yields. | 30 |
| 31 | Radial components at Station 6W for two source configurations. | 31 |
| 32 | Transverse components at Station 6W for two source configurations. | 32 |
| 33 | Vertical components at Station 6W for two source configurations. | 33 |
| 34 | Resultant power spectral densities at Station 6W for two source configurations. | 34 |
| 35 | Radial components at Station 2BN for two source configurations. | 35 |
| 36 | Transverse components at Station 2BN for two source configurations. | 36 |
| 37 | Vertical components at Station 2BN for two source configurations. | 37 |
| 38 | Resultant power spectral densities at Station 2BN for two source configurations. | 38 |
| 39 | Radial components for Pre-Gondola I Bravo Event at various distances. | 39 |
| 40 | Transverse components for Pre-Gondola I Bravo Event at various distances. | 40 |
| 41 | Vertical components for Pre-Gondola I Bravo Event at various distances. | 41 |
| 42 | Resultant power spectral densities for Pre-Gondola I Bravo Event at various distances. | 42 |
| 43 | Radial components for Pre-Gondola II 140-ton row charge at various distances. | 43 |
| 44 | Transverse components for Pre-Gondola II 140-ton row charge at various distances. | 44 |
| 45 | Vertical components for Pre-Gondola II 140-ton row charge at various distances. | 45 |
| 46 | Resultant power spectral densities for Pre-Gondola II 140-ton row charge at various distances. | 46 |

Figures (Continued)

| | | |
|-----|---|----|
| 47 | Radial components at Station 2BN for four 20-ton events at different depths of burst. | 47 |
| 48 | Transverse components at Station 2BN for four 20-ton events at different depths of burst. | 48 |
| 49 | Vertical components at Station 2BN for four 20-ton events at different depths of burst. | 49 |
| 50 | Resultant power spectral densities at Station 2BN for four 20-ton events at different depths of burst. | 50 |
| 51 | Peak power spectral densities plotted against radius for Pre-Gondola I Bravo Event (α comes from the equation: $PSD_p(R) = KR^{-\alpha}$). | 51 |
| 52 | Peak power spectral densities plotted against radius for Pre-Gondola II 140-ton row charge (α comes from the equation: $PSD_p(R) = KR^{-\alpha}$). | 51 |
| 53 | Energy in seismic signal for components and total energy as a function of radius for Pre-Gondola I Bravo Event (α comes from the equation: $\sum E(R) = KR^{-\alpha}$). | 51 |
| 54 | Energy in seismic signal for components and total energy as a function of radius for Pre-Gondola II 140-ton row charge (α comes from the equation: $\sum E(R) = KR^{-\alpha}$). | 51 |
| 55 | Slope of power spectral density attenuation as a function of frequency for Pre-Gondola I Bravo Event (i. e., slope α comes from the equation: $PSD(R, f) = K_f R^{-\alpha(f)}$). | 52 |
| 56 | Slope of power spectral density attenuation as a function of frequency for Pre-Gondola II 140-ton row charge (i. e., slope α comes from the equation: $PSD(R, f) = K_f R^{-\alpha(f)}$). | 52 |
| 57 | Comparison of attenuation for resultant power spectral densities plotted as a function of frequency for Pre-Gondola I and II. | 52 |
| 58 | Comparison of slopes of attenuation of comb filter peak velocities to one-half of slopes of attenuation of power spectral density resultant for Pre-Gondola II 140-ton row charge as a function of frequency. | 53 |
| 59 | Total station energy ($\sum E$) at Station 2BN (Pre-Gondola I) showing transmitted energy dependence upon actual depth of burst (Bravo datum is neglected—see text); curve is extrapolated to DOB's for 40-ton and 0.5-ton events to obtain comparisons for Pre-Gondola II. | 53 |
| 60 | Total station energy ($\sum E$) vs yield after depth of burst effect has been removed. | 53 |
| 61a | Radial and transverse components at Station 2BN for Pre-Gondola I (all events). | 54 |
| 61b | Vertical component at Station 2BN for Pre-Gondola I (all events). | 54 |
| 61c | Resultant velocity at Station 2BN for Pre-Gondola I (all events). | 55 |
| 62 | Signals recorded at Station 2BN for three different yields (0.5- and 20-ton single bursts and 140-ton row charge). | 55 |

INTERMEDIATE RANGE GROUND MOTIONS FOR PRE-GONDOLA II AND ASSOCIATED EVENTS

Introduction

DESCRIPTION OF PROJECT PRE-GONDOLA II

Project Pre-Gondola II was a row-charge cratering experiment in weak, wet clay-shale conducted by the U. S. Army Engineer Nuclear Cratering Group (NCG) as a part of the joint Atomic Energy Commission-Corps of Engineers nuclear excavation research program. The primary purpose of this nominal 140-ton five-charge experiment was to gain row-charge cratering experience in a weak, wet medium. In addition, this experiment tested techniques for connecting a row-charge crater to an existing crater and for over-excavating to accept throwout from a follow-on connecting row-charge crater.

Project Pre-Gondola II was detonated at Valley County, near the edge of the Fort Peck Reservoir approximately 18 mi south of Glasgow, Montana, at 0800 hr (MDT), 28 June 1967 (see Fig. 1). Coordinates of the center charge were W106°38'31", N47°55'51". The orientation of the row was along an alignment 10° East of North to 10° West of South. This alignment extended through the center of the Charlie crater (an existing crater created during the Pre-Gondola I series).

The average lip crest-to-lip crest dimensions after connection to the Charlie crater were 640 ft × 280 ft. Individual charge yields, depths, spacing, and resulting apparent crater dimensions are given in Table I.

Table I. Pre-Gondola II charge yields, depths, spacing, and resulting apparent crater dimensions.

| Charge | Tons NM ^a | Emplacement configuration (ft) | | Apparent crater dimensions (ft) | |
|--|----------------------|--------------------------------|--------------------|---------------------------------|----------------------|
| | | Depth of burst | Spacing | Width W _a | Depth D _a |
| Charlie (existing crater) ^b | (19.62) | (42.5) | — | (160.8) | (32.6) |
| E (connecting charge) | 38.61 | 59.7 | 105.5 ^c | 206.5 | 55.5 |
| F | 19.70 | 49.4 | 79.8 | 152.5 | 37.5 |
| G (center charge) | 19.55 | 48.8 | 79.9 | 164.0 | 36.9 |
| H (over-excavating charge) | 39.56 | 59.9 | 79.9 | 214.5 | 57.0 |
| I | 20.00 | 48.8 | 79.9 | 173.0 | 33.5 |

^aSpherical charges of liquid explosive nitromethane (CH₃NO₂). Actual total charge weight was 137.42 tons.

^bDimensions for Charlie crater are those existing prior to row-charge event.

^cDistance between this charge and charge on line above.

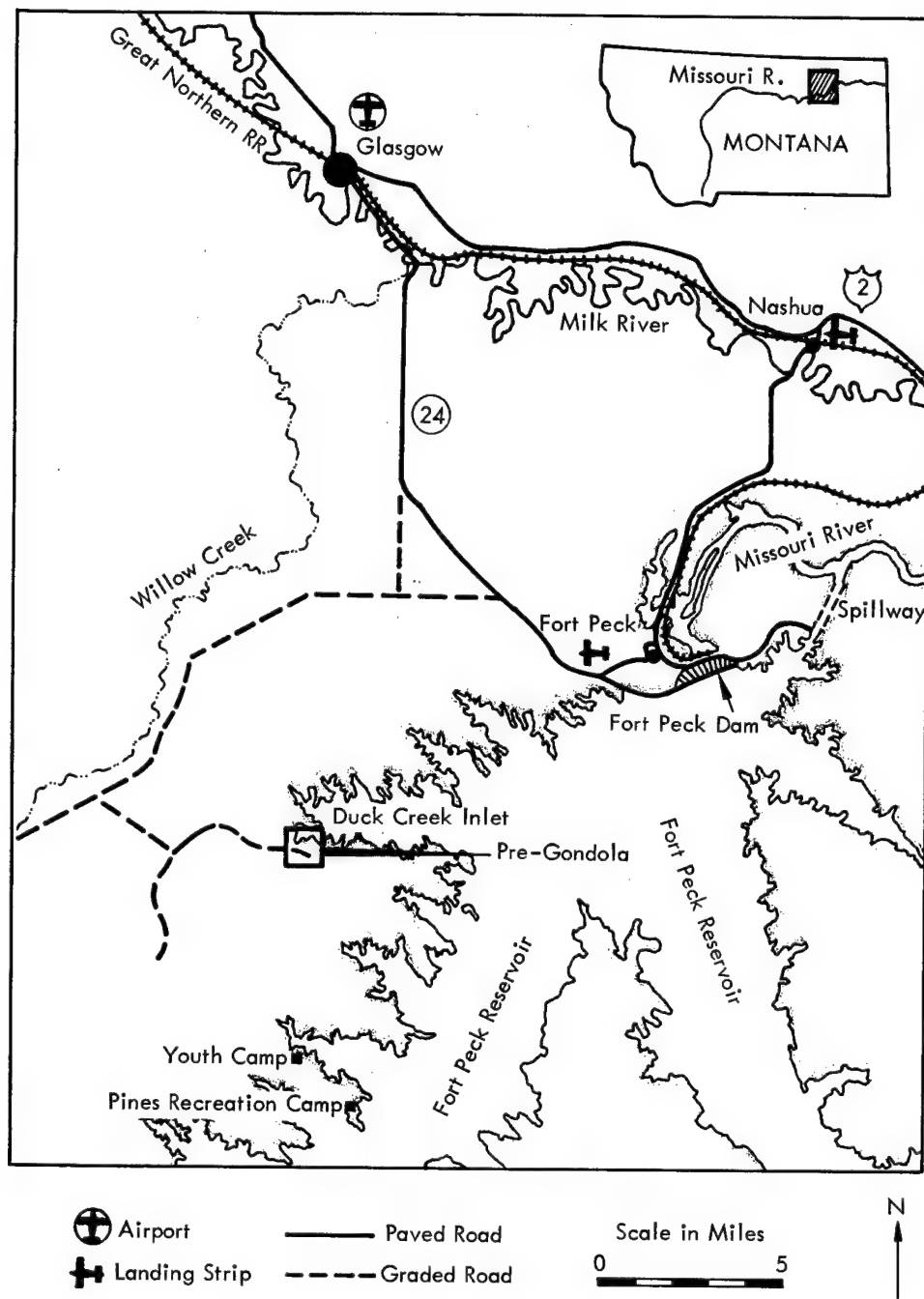


Fig. 1. Map showing environs of Pre-Gondola II and associated events.

DESCRIPTION OF EVENTS ASSOCIATED WITH PRE-GONDOLA II

Prior to the row-charge detonation, two 1000-lb shots were fired to investigate the effects of small-magnitude decoupling factors. These events were SD-1 (fully

coupled) and SD-2 (decoupled, $V_{\text{cavity}}/V_{\text{exp}} = 2.0$). These events were both detonated on 14 June 1968 at the same site as the 140-ton event. Cratering data for these two events are summarized as follows:

| Event | Charge (tons NM) | Cavity volume explosive volume | DOB (ft) | Apparent crater dimensions (ft) | |
|-------|---------------------|-----------------------------------|-------------|------------------------------------|-------------|
| | | | | Width W_a | Depth D_a |
| SD-1 | 0.50 | 1.0 | 17.3 | 50.2 | 10.5 |
| SD-2 | 0.50 | 2.0 | 17.7 | 47.4 | 10.5 |

DESCRIPTION OF OTHER EVENTS RELATED TO PRE-GONDOLA II

In addition to the above events, considerable additional analysis has been made of seismic records taken during Pre-Gondola I, located at the same site as the Pre-Gondola II events. This analysis is reported here. The work was

originally reported in PNE-1105.¹ Since the writing of that report additional analysis techniques have become available, and it is imperative that for a complete understanding of the results of Pre-Gondola II, these data and results be included at this time. A summary of the Pre-Gondola I cratering data is as follows:

| Event | Charge (tons NM) | DOB (ft) | Apparent crater dimensions (ft) | |
|---------|---------------------|-------------|------------------------------------|-------------|
| | | | Width W_a | Depth D_a |
| Charlie | 19.62 | 42.49 | 160.8 | 32.6 |
| Bravo | 19.36 | 46.25 | 157.0 | 29.5 |
| Alfa | 20.35 | 52.71 | 152.2 | 32.1 |
| Delta | 20.24 | 56.87 | 130.2 | 25.2 |

OBJECTIVES

In order to provide a knowledgeable basis to plan for possible large scale geonuclear projects in the future, it is necessary to gather information on the characteristic behavior of various earth materials at the shot point and in the vicinity of subsurface explosions. The Pre-Gondola series of explosions offers an opportunity to study the effect of several important parameters on the transmitted

seismic signals. The variety of yields, depths of burst, and shot configurations, all being detonated at essentially the same geographical location, makes it possible to make repeated measurements at the same locations. This process means that the effect of transmission path can, to a large extent, be normalized out of the data at any given station. (This is not entirely true since the "transmissibility" of the transmission path is frequency-dependent and, therefore,

may "change" if the source function is altered drastically with respect to frequency—see Appendix A.)

The explosions were detonated in a wet clay-shale media which is characteristic of several locations of interest to the nuclear cratering program. This region of northeastern Montana is also of interest because it appears to be relatively simple from a physical properties standpoint. Flat-lying, extensive, thick layers of sedimentary materials exist to depths of over 8,000 ft and distances of over 100 km. In view of the above, the following objectives were chosen for this study:

1. Dependence of velocity time history of ground motion upon yield, depth of burst, and various shot configurations (single charge, row-charge, and small decoupling ratios).
2. Dependence of peak velocity spectra and power spectral densities upon yield, depth of burst, and shot configuration.
3. Identification of those properties of explosively induced seismic signals which scale uniformly and consistently over large ranges of yield, depth of burst, and variations in shot configurations.
4. Empirical measurements of seismic motion from cratering explosions in an extensive water-saturated clay-shale material.
5. A study of the attenuation with distance of peak signal amplitudes, velocity spectra, and power spectral density in a simple geology.

BACKGROUND

A word of explanation is necessary at this point. Although this report is technically a report on Pre-Gondola II, it also

contains much information gathered during Pre-Gondola I. The reasons for this are two-fold: (1) the events from the separate programs are meaningful to the fullest extent only when correlated and presented as a unit, and (2) the power spectral density analysis technique (PSD) was not available when the Pre-Gondola I work was reported. It was the conclusion of that report (PNE-1105) that, when the analysis technique did become available, the data should be reported. It is included in this report to simplify the task of both the reader and writer.

Figure 1 shows the location of the Pre-Gondola experiments in northeastern Montana. The ideal geology for seismic propagation studies would be a simple two-layer medium, flat, and of infinite extent in the horizontal directions. This is the simplest geometry that would allow for propagation of surface waves, direct p and s arrivals and refracted arrivals. The author is unaware of the existence anywhere of such a geologic setting of appropriate dimensions.

The geology of northeastern Montana is however relatively simple.² Massive sedimentary beds make up the surface geology. These vary in thickness up to 2000 ft and comprise in total thickness about 5000-8000 ft. Structural features such as the Williston Basin are of the order of hundreds of miles across and of relatively shallow relief, resulting in relatively flat bedding planes.

Previous work on seismic attenuation has been primarily concerned with peak amplitudes of motion in the wave trains with little or no regard for the total frequency content of the motion.^{3,4} The reasons for this condition have been twofold.

Until recently there has been a lack of good instrumentation and analysis capabilities to do this work. More important, most of the experience to date has been in such complicated geologic settings that meaningful frequency analysis has been almost impossible. The relatively simple geology offers an opportunity to investigate both the frequency content and the amplitude as a function of distance from the source and for variations in yield and depth of burst of the source.

Most explosions with yields greater than 5 tons have fallen into three categories:

1. Industrial explosions of all kinds with usually little or no instrumentation.
2. Well-instrumented, completely contained single-event explosions.
3. Well-instrumented cratering experiments.

For the most part the larger cratering experiments prior to Pre-Gondola have been single events. Where there have been several events, the layout and seismic instrumentation offered no opportunity to study coupling of energy into the seismic signal.

A requirement for a dynamic cratering condition (as opposed to a subsidence crater*) is that the cavity communicates with the atmosphere before the cavity growth has stopped. This means that the

overburden must fail in tension, and the thus-isolated blocks of overburden will be ejected along a ballistic trajectory. Seismically, this differs from the completely contained situation by allowing the cavity pressure to drop at early times, thus preventing the coupling of some fraction of the energy into the seismic signal at late times. The possible decrease in seismic energy is an unknown, and previous estimates of seismic motions for cratering shots have been based on results for the completely contained case.

If there is an effect due to cratering it could be proportional to a function of either the actual depth or the scaled depth ($D/W^{1/3,4}$). In either case some effect would be noticed for a shallow, low-yield explosion. If coupling is a function of actual depth (in other words, a function of the total time before breakout), one would expect to see a less marked effect for deeper, high-yield events. If the effect is a function of the scaled depth, then it should be the same for all yields. Pre-Gondola II and associated events offer a suitable variety of events to study these possibilities.

*A subsidence crater occurs when an explosively created subsurface cavity collapses resulting in a surface depression without any direct cavity-atmosphere interaction.

Procedure

STATION SELECTION

The number and location of seismic stations for Pre-Gondola II were essentially the same as for Pre-Gondola I, since the criteria were identical.¹ Figure 2 is a map showing the location of stations for the events reported herein. All stations, their locations with respect to SGZ, and the events during which they were occupied are given in Table II along with other information. This coverage is sufficient to provide the following:

1. Five stations on a radius for two different yields (one of them a row charge)
2. One station repeated for a single yield at four depths of burst
3. Two stations repeated for the decoupling sequence
4. One station repeated for three yields at optimum depth of burst
5. Stations 90 deg apart with respect to SGZ to study the asymmetry of seismic radiation from a row charge.

Table II. Events reported and data analyses used for velocity geophone measurements.

| Event | Station | Station location | | Quality of data | Analysis techniques used ^a |
|-------------------------------|---------|------------------|-----------|-----------------|---------------------------------------|
| | | Distance | Azimuth | | |
| Pre-Gondola I | | | | | |
| Alfa | 2BN | 11.65 | 8°E of N | Excellent | VA, PSD |
| Charlie | 2BN | 11.65 | 8°E of N | Excellent | VA, PSD |
| Delta | 2BN | 11.65 | 8°E of N | Excellent | VA, PSD |
| Bravo | 2BN | 11.65 | 8°E of N | Excellent | VA, PSD |
| Bravo | 3N | 29.3 | 9°E of N | Poor | VA, PSD |
| Bravo | 4N | 52.0 | 8°E of N | Good | VA, PSD |
| Bravo | 5N | 95.9 | 6°E of N | Excellent | VA, PSD |
| Pre-Gondola II | | | | | |
| SD-1 | 2BN | 11.65 | 8°E of N | Fair | VA, CFPV, PSD |
| SD-1 | 6W | 6.39 | 90°W of N | Good | VA, CFPV, PSD |
| SD-2 | 2BN | 11.65 | 8°E of N | Fair | VA, CFPV, PSD |
| SD-2 | 6W | 6.39 | 90°W of N | Good | VA, CFPV, PSD |
| Row charge (E, F, G, H, I) | 2BN | 11.65 | 8°E of N | Excellent | VA, CFPV, PSD |
| | 3N | 29.3 | 9°E of N | Excellent | VA, CFPV, PSD |
| | 4N | 52.0 | 8°E of N | Excellent | VA, CFPV, PSD |
| | 5N | 95.9 | 6°E of N | Excellent | VA, CFPV, PSD |
| | 1N | ~5.0 | 8°E of N | Very poor | None |
| | 6W | 6.39 | 90°W of N | Very poor | None |

^aVA = vector addition, PSD = power spectral density, CFPV = comb filter peak velocity.

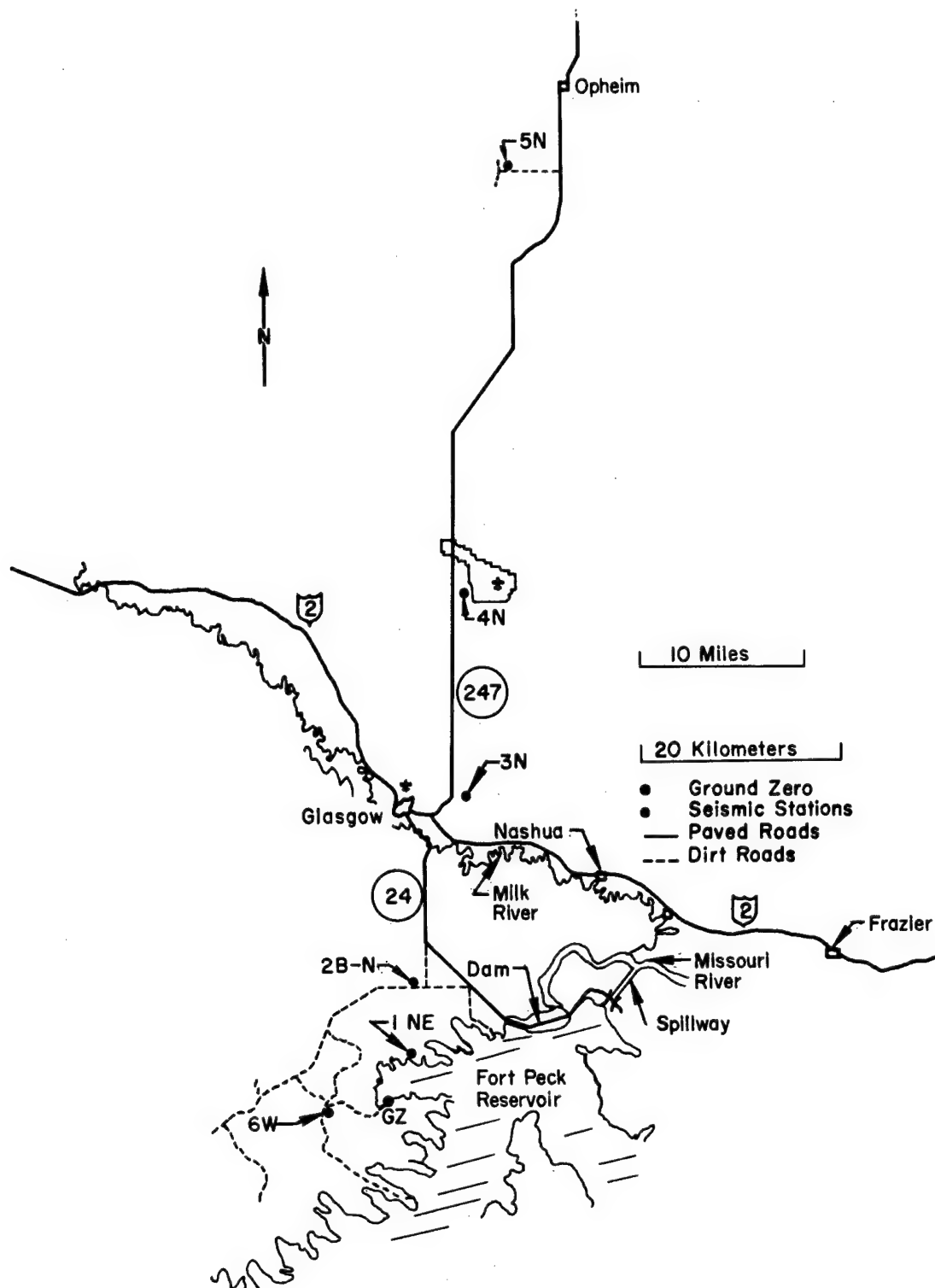


Fig. 2. Map showing location of free-field seismic stations for Pre-Gondola II 140-ton row charge. (Station 2BN was operated for Alfa, Charlie, Delta, and Bravo Events, and Stations 3N, 4N, and 5N were occupied on Bravo Event during Pre-Gondola series; Stations 2BN and 6W were occupied on decoupling series during Pre-Gondola II.)

SEISMIC INSTRUMENTATION

Ground motions were measured with modified HS-10-1 velocity geophones. The HS-10-1 is a moving coil instrument with a 1-sec natural period; with 70% damping it has a flat response curve above 1 Hz (cycles per second). The sensitivity is determined by the coil impedance (Fig. 3). To improve performance and reliability and to reduce instrument drift, adjustments were made in the field and all instruments were monitored after emplacement. Emplacement was accomplished about 1 wk prior to the event date, and the final monitor check was made on the evening prior to the event date. The critical

parameters are sensitivity, natural period, and damping ratios.

Each station consisted of one vertical and two horizontal instruments, the latter oriented radially and transversely to the shot point. This comprises the standard rectangular system, giving motion in the three mutually orthogonal directions necessary to define translational motion. As a matter of definition, for the rest of this report the following designations will be used: x refers to radial motion, y refers to transverse motion, z refers to vertical motion, and Res is the vector sum ($\sqrt{x^2 + y^2 + z^2}$) for velocity and an arithmetic sum ($x + y + z$) for energy.

Isolation from wind noise and good mechanical coupling with the earth are

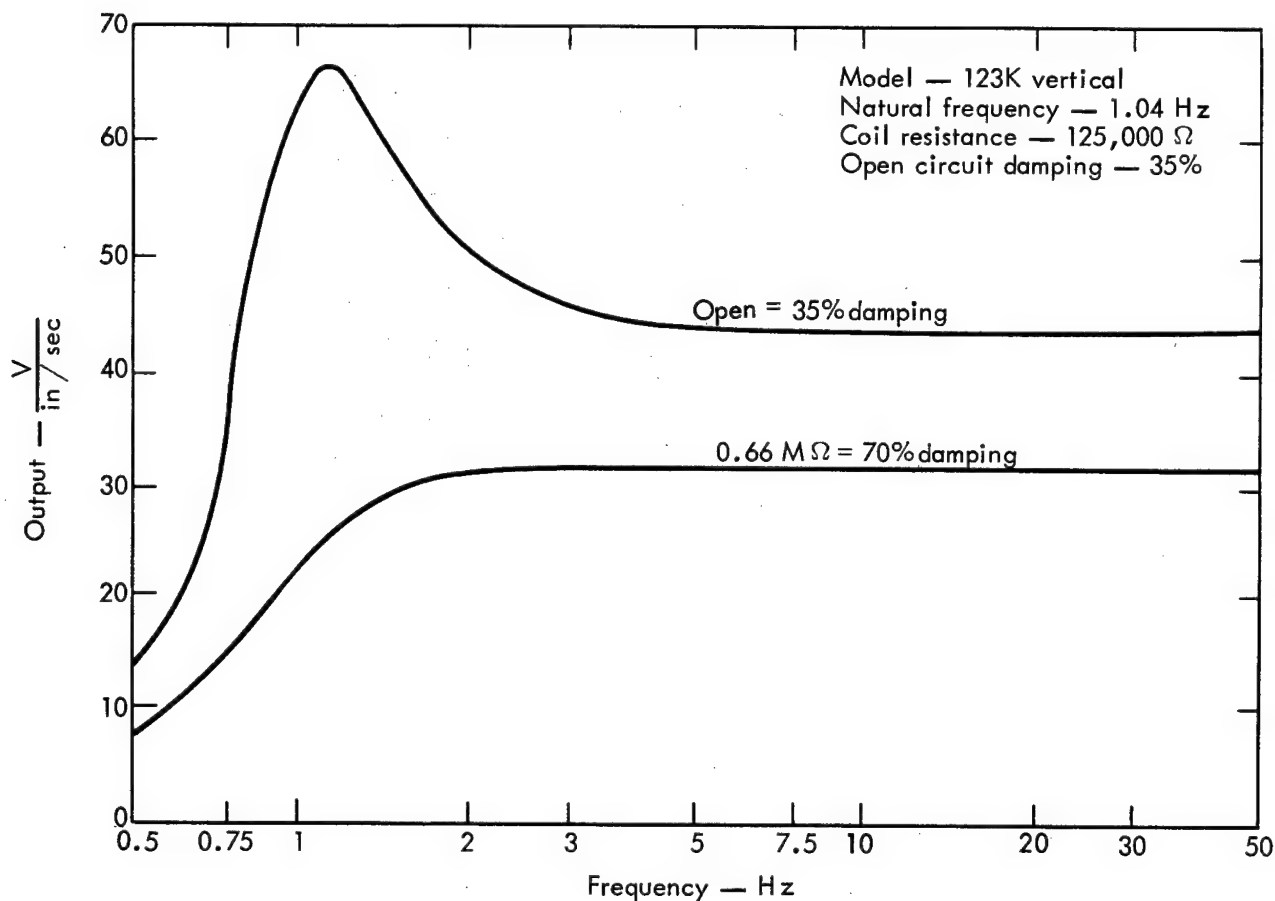


Fig. 3. Response of HS-10-1 velocity geophone at 35 and 70% damping.

accomplished by burying the instruments. To meet the requirements of instrument protection, ease of operation and emplacement, quality of orientation, etc., an instrument canister was developed to maintain the instruments in the mutually orthogonal relationship. The water-tight canister is then easily buried in a 12-in. diameter, 40-in. hole and oriented as a unit. Tamped sand was used as a backfill. Figure 4 illustrates the details of the instrument package.

RECORDING AND TIMING

Magnetic tape recorders utilizing an FM electronics system, a four-track head,

and a 1/4-in. loop-tape cartridge with a 5-1/2-min capacity were used on all measurements. One of these recorders is shown in Fig. 5 and partly dismantled in Fig. 6. The recorder shown was used on the Pre-Gondola I Events Alfa, Bravo, Charlie, and Delta. For the Pre-Gondola II Events certain modifications were made on the power supplies and VCO's to improve their temperature and time stability. These modifications did not significantly alter the appearance of the recorders.

Each geophone (component) was recorded on one track of the magnetic tape and an oscillator-controlled timing signal was recorded on the fourth track. An

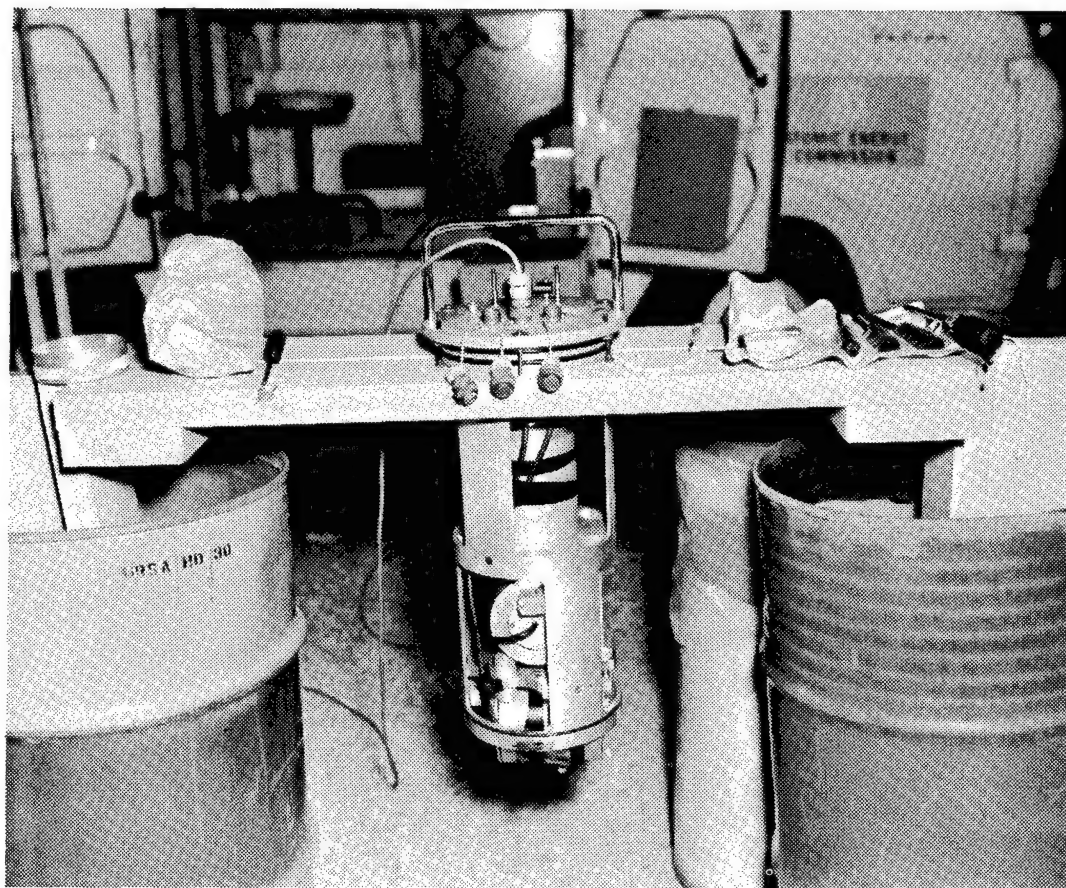


Fig. 4. Three-component instrument package during set-up and prior to insertion into outer canister (canister is partly visible behind metal drum on right).

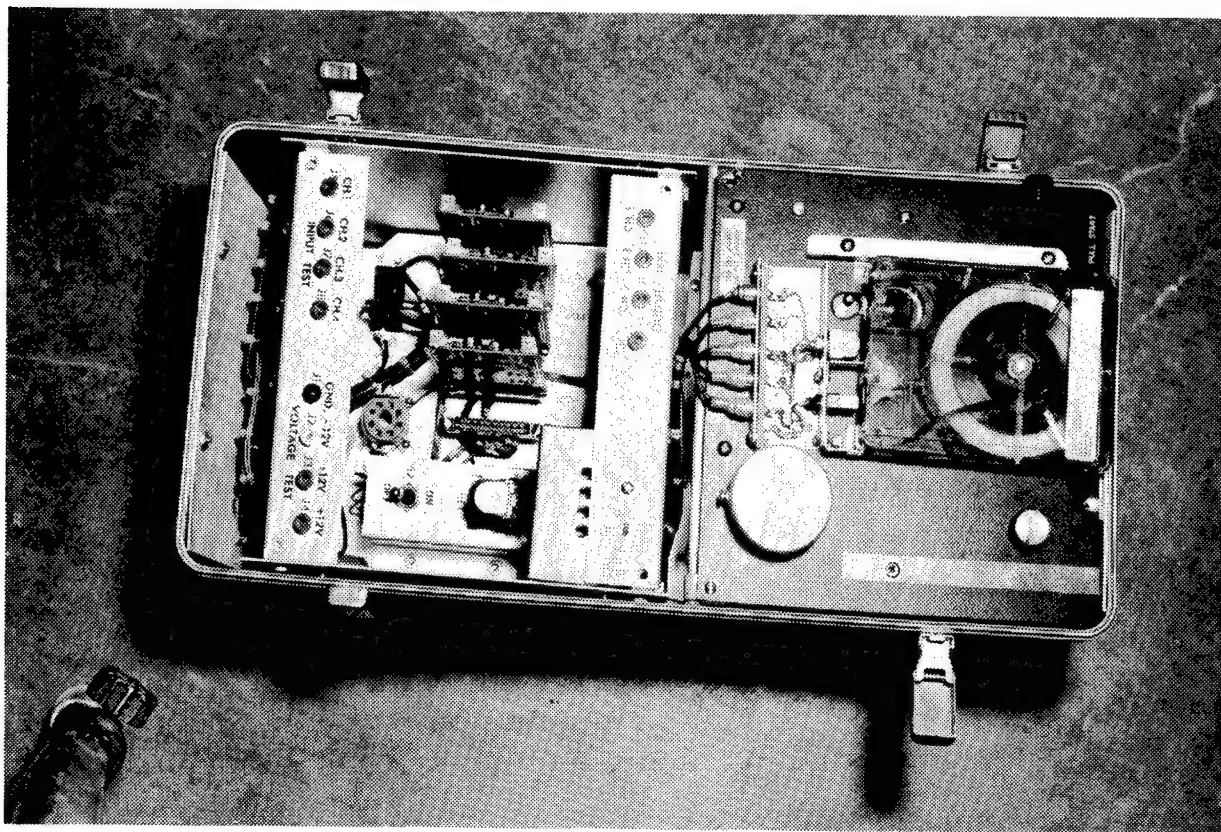


Fig. 5. Top view of tape recorder used for recording geophone signals (tape cartridge is shown in place at right).

approximate zero time signal (square pulse) was manually superimposed on the timing channel by the station operator who was in radio contact with the firing control center.

The cross timing accuracy between stations is determined by the variation in station operator reaction time. This variation could cause an uncertainty of as much as 1 sec in actual zero time. This uncertainty is considered too large to allow meaningful analysis of the transit times of various wave phases, etc.

INFORMATION RETRIEVAL AND REDUCTION

Instrument responses to step functions were recorded prior to events. Recorder

calibration signals (sine waves and ramps) were recorded on the "event tapes" before and after the event. All recording equipment was turned on and running at minus 30 sec. A positive dc voltage of about 1-sec duration was manually superimposed at zero time on the timing channel.

Subsequent to the event, magnetic tape records from all stations were redubbed to a 1-in. tape to make them compatible with the digital analysis system. Records were digitized with an Astro-Data analog-to-digital translator. Analysis of digitized records was completed on IBM 7094 and CDC 3600 computers. The digitized record contained 400 data points per sec for each component.

DATA ANALYSIS

The most used method of analyzing seismic motion data of the type with which we are concerned has, in the past, been to measure the peak amplitude attained regardless of where in the record it occurred. Such an analysis is crude to be sure, but little else could be done due to the high cost of hand analysis on the many records that had to be studied. Digital computers have become common enough to reduce the total cost and more

sophisticated analysis techniques are now possible.

It is of interest at this time to compare this method to newer ones and to obtain some measure of the validity of the old method. Accordingly peak motions were measured from the records. Also measured were the time of arrival of that motion after the first motion and the approximate frequency of the motion. The latter is calculated by assuming the half wave to be of harmonic nature; i. e.,

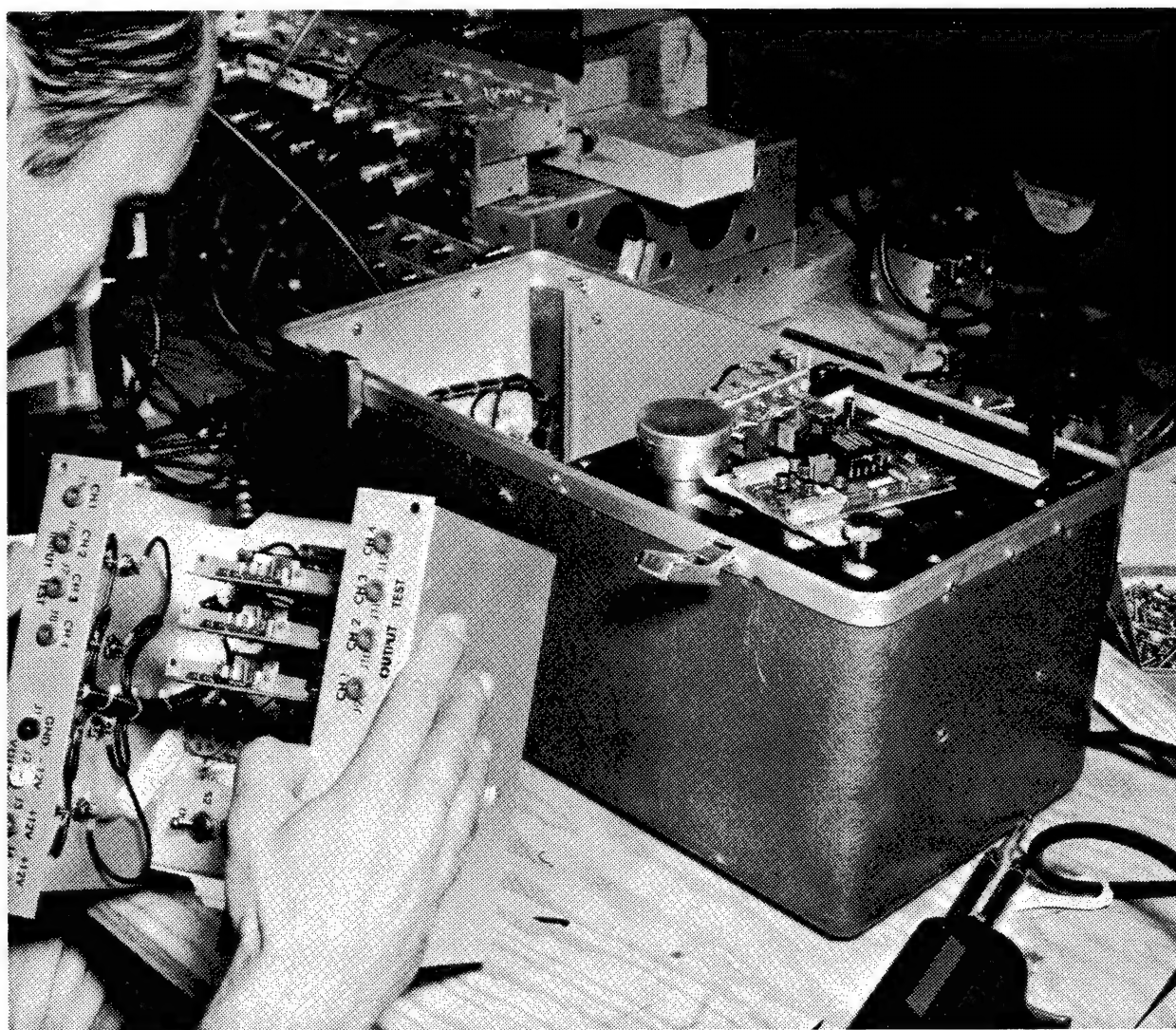


Fig. 6. Partly dismantled recorder, showing its size, portability, etc.

$f = (1/2) (1/\Delta t)$ where Δt is the time between zero crossings just prior to and following the peak motion.

One of the newer techniques for analyzing a time varying signal is to filter it into its spectral components to measure the peak amplitudes in each component generating a velocity spectra. This method is called comb filter peak velocity (CFPV) and is described in Appendix B.

The actual equipment used in this analysis was band pass filters. The signal ratios at 1 octave from the center frequency were about 15 dB for power (voltage_{in}/voltage_{out} \approx 6). Center frequencies were set in a semi-systematic pattern to cover the range of interest. They were 0.75, 1.0, 1.5, 2.0, 3.0, 4.0, 5.0, 6.0, 8.0, 10.0, 12.0, and 15.0 Hz, respectively.

Comb filtering was planned for the records obtained in the 140-ton row charge, as well as the SD-1 and SD-2 Events. The peak amplitudes for each frequency from a given geophone were plotted against frequency to illustrate the spectral content of the signal. Comparison of the plots of the three space coordinates, the different stations, and the several events provides an understanding of how the spectral content varies with distance, space direction, source configuration (for the SD-1 Event compared to the SD-2) and for yield (the SD-1 Event compared to the 140-ton row charge). Attenuation for various frequencies can be determined from a fit to the data. The equation is

$$A_f = \text{Amplitude } (f) = K_f R^{-\alpha(f)}$$

where α is the attenuation slope.

A comparison of these results to those obtained by the power spectral density method of analysis (PSD) provides a basis for choosing the most consistent and appropriate method of the two for analyzing ground motions from underground explosions.

The three rectangular components are sufficient to describe the translational motion of a point. However to gain a knowledge of the absolute amplitude of motion requires a transformation to spherical coordinates. The theory and computer code for the transformation is described in Appendix B.

The code calculates x , y , z , $(\text{Res})^2$, $|\text{Res}|$, θ , and ϕ as functions of time. It is called (surprisingly) VECTOR.

Another method of analyzing a signal to obtain a measure of its spectral content and total energy is to determine the PSD and the integral of $(\text{PSD})df$ or E . This method is described in Appendix C and Ref. 5. The quantities produced by the PSD code for a given time history of velocity are $\text{PSD}(f)$, or density of power as a function of frequency for three components, a resultant E , or total energy in a component, and $\sum E$ or total station energy.

The PSD's for all signals in this report were to be calculated and comparisons made to determine the variance with yield, depth of burst, source configuration, and radius and to make selected comparisons with the CFPV's for some events and stations.

Results

DATA RECOVERY AND REDUCTION

Table II lists the events included in this report along with the various seismic stations, their locations with respect to SGZ, the quality of the data recorded, and the analysis techniques used on each station recording.

The failure of the primary recorder is the reason for the poor quality on Station 3N for Bravo. A backup recorder set at low gain recorded the event but the signal-to-electronic noise ratio is small. On the 140-ton row charge the motions at Stations 6W and 1N exceeded the mechanical limits of the geophones, making the data totally unreliable. No results for these two stations on this event will be included. The small motions from Events SD-1 and SD-2 resulted in a small signal-to-background seismic noise, reducing the quality of these signals somewhat.

The method of data reduction requires redubbing which introduces additional noise, usually random or white, but sometimes peculiar to a given machine as a result of mechanical flutter in the tape drive, etc. This is apparently the cause of spikes in the power spectral density curves at $9\frac{1}{2}$ and 15 Hz in all of the SD-1, SD-2, and 140-ton row-charge Events from Pre-Gondola II. The large spike in the PSD for all components of Station 3N on Bravo is not present for the 140-ton Event at 3N nor is it present on any other station. It is assumed that this is due to the tape drive of the event recorder especially since this was the low gain recorder. There is, however, some

doubt about the validity of this assumption and both possibilities are reported in the peak amplitude values. It has little effect upon the total energy E (see Appendix C) in the signal.

PEAK VELOCITY AND VECTOR ADDITION

Table III lists the peak velocity of the components and the peak vector resultant, the time of arrival of that peak after first motion, and the apparent frequency of that motion for all stations and all events. Peak velocities for the stations recording for Bravo and the 140-ton row charge are plotted in Figs. 7 and 8 as a function of distance from SGZ.

COMB FILTER PEAK VELOCITY

Only the records from SD-1, SD-2, and the 140-ton row charge were analyzed in this manner. Table IV contains these data. A better concept of these data is gained when they are put in graphical form. Figures 9 and 10 show the results for Station 2BN on SD-1 and SD-2, respectively, and Figs. 11, 12, and 13 compare the three separate space coordinates for the two events to illustrate the differences due to the small decoupling factor. Figures 14 through 18 show results for Station 6W for the same events in the same sequence.

The CFPV-frequency curves for each station for the 140-ton row-charge are shown in Figs. 19 through 22, while the individual components for all stations are compared in Figs. 23 through 25. The

Table III. Velocity data—all stations.

| Event | Station | Component | Peak velocity (mm/sec) | Time of arrival after first motion (sec) | Frequency of motion (Hz) |
|------------|---------|-----------|---------------------------|--|--------------------------------|
| SD-1 | 2BN | x | 0.0385 | 11.2 | 1.75 |
| SD-1 | 2BN | y | ~0.027 | 11.6 | 1.75 |
| SD-1 | 2BN | z | 0.0338 | 0.8 | 6.8 |
| SD-1 | 2BN | Res | 0.042 | 11.6 | - |
| SD-2 | 6W | x | 0.108 | 7.6 | 2.4 |
| SD-2 | 6W | y | 0.096 | 9.4 | 3.7 |
| SD-2 | 6W | z | 0.096 | 9.97 | 8.0 |
| SD-2 | 6W | Res | 0.113 | 7.6 | - |
| SD-2 | 2BN | x | 0.0545 | 11.9 | 1.75 |
| SD-2 | 2BN | y | ~0.045 | 12.5 | 1.75 |
| SD-2 | 2BN | z | 0.0432 | 1.4 | 7.6 |
| SD-2 | 2BN | Res | 0.0687 | 12.6 | - |
| SD-1 | 6W | x | 0.055 | 7.5 | 2.5 |
| SD-1 | 6W | y | 0.072 | 7.5 | 3.4 |
| SD-1 | 6W | z | 0.099 | 1.0 | 8.8 |
| SD-1 | 6W | Res | 0.099 | 1.0 | - |
| Bravo | 2BN | x | 0.76 | 12.4 | 1.75 |
| Bravo | 2BN | y | 0.34 | 12.4 | 1.2 |
| Bravo | 2BN | z | 1.20 | 2.4 | 4.5 |
| Bravo | 2BN | Res | 1.29 | 2.4 | - |
| Bravo | 3N | x | 0.16 | ? | 1.5 |
| Bravo | 3N | y | 0.10 | ? | 1.5 |
| Bravo | 3N | z | 0.125 | ? | 2.5 |
| Bravo | 3N | Res | 0.220 | ? | - |
| Bravo | 4N | x | 0.0207 | 12.65 | 3.0 |
| Bravo | 4N | y | 0.0142 | 14.7 | 3.0 |
| Bravo | 4N | z | 0.0257 | 13.5 | 2.5 |
| Bravo | 4N | Res | 0.0306 | 13.5 | - |
| Bravo | 5N | x | 0.024 ± 10% | 5.48 | 7.0 |
| Bravo | 5N | y | 0.014 ± 10% | 5.53 | 8.0 |
| Bravo | 5N | z | 0.08 ± 10% | 4.2 | 8.0 |
| Bravo | 5N | Res | 0.08 ± 10% | 4.2 | - |
| Alfa | 2BN | x | 1.10 | 2.32 | 6.0 |
| Alfa | 2BN | y | 0.45 | 11.9 | 2.0 |
| Alfa | 2BN | z | 1.94 | 2.25 | 5.0 |
| Alfa | 2BN | Res | 2.09 | 2.25 | - |
| Charlie | 2BN | x | 0.75 | 3.2, 11.2 | 5.0, 1.5 |
| Charlie | 2BN | y | 0.28 | 12.8 | 1.5 |
| Charlie | 2BN | z | 1.38 | 3.1 | 5.0 |
| Charlie | 2BN | Res | 1.46 | 3.1 | - |
| Delta | 2BN | x | 1.72 | 11.8 | 1.75 |
| Delta | 2BN | y | 0.72 | 13.5 | 1.75 |
| Delta | 2BN | z | 2.20 | 2.26 | 6.00 |
| Delta | 2BN | Res | 2.45 | 2.34 | - |
| Row charge | 2BN | x | 4.4 | 10.7 | 2.0 |
| Row charge | 2BN | y | 2.8 | 11.7 | 0.8 |
| Row charge | 2BN | z | 5.8 | 2.21 | 4.8 |
| Row charge | 2BN | Res | 6.3 | 2.21 | - |
| Row charge | 3N | x | 0.251 | 10.5 | 2.0 |
| Row charge | 3N | y | 0.209 | 20.8 | 1.75 |
| Row charge | 3N | z | 0.655 | 6.8 | 3.0 |
| Row charge | 3N | Res | 0.663 | 6.8 | - |
| Row charge | 4N | x | 0.193 | 12.6 | 3.1 |
| Row charge | 4N | y | 0.14 | 14.2 | 3.0 |
| Row charge | 4N | z | 0.32 | 12.0 | 2.7 |
| Row charge | 4N | Res | 0.344 | 12.2 | - |
| Row charge | 5N | x | 0.097 | 5.4 | 4.0 |
| Row charge | 5N | y | 0.046 | 12.9 | 3.3 |
| Row charge | 5N | z | 0.197 | 4.0 | 7.0 |
| Row charge | 5N | Res | 0.197 | 4.0 | - |

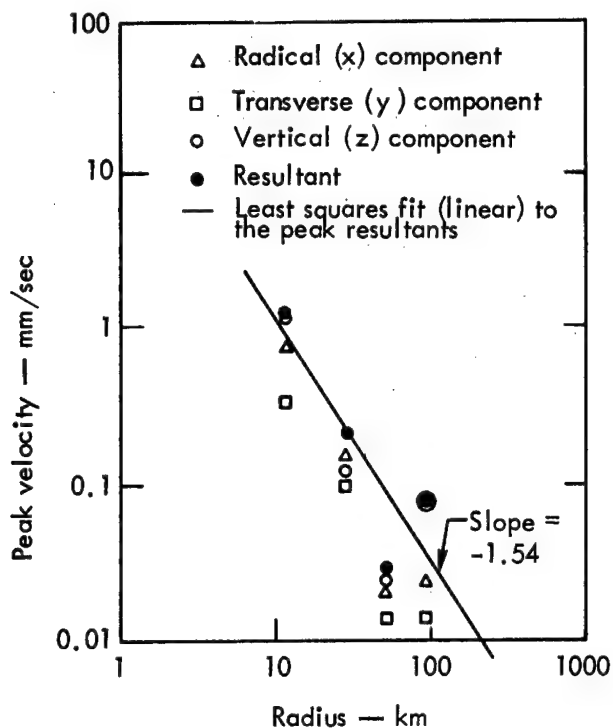


Fig. 7. Peak velocities for Pre-Gondola I Bravo Event, as a function of distance (large value at 96 km is due to single pulse of very high amplitude in velocity-time signature; rest of signature is of relatively low amplitude).

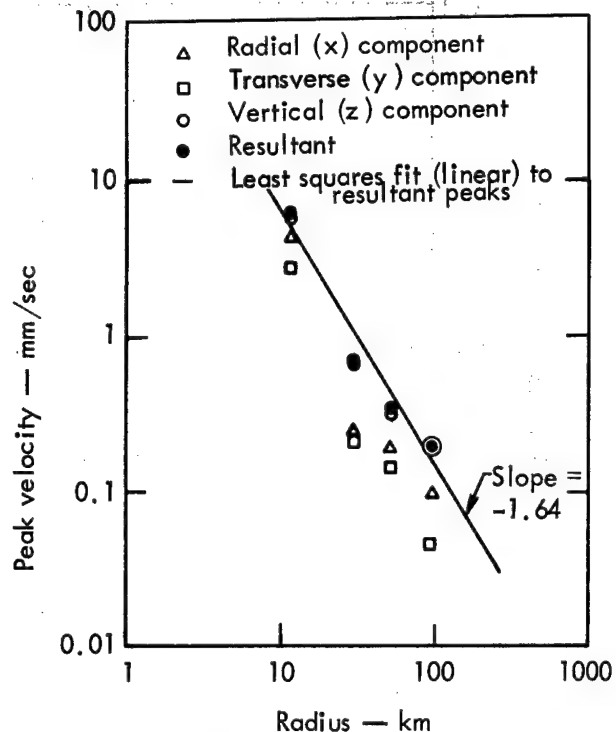


Fig. 8. Peak velocities for Pre-Gondola II 140-ton row charge as a function of distance.

Table IV. Comb filter peak velocity data for Pre-Gondola II.

| Event | Station | Component | 0.75 Hz | 1.0 Hz | 1.5 Hz | 2.0 Hz | 3.0 Hz | 4.0 Hz | 5.0 Hz | 6.0 Hz | 8.0 Hz | 10.0 Hz | 12.0 Hz | 15.0 Hz |
|--------------------|---------|-----------|---------|--------|--------|--------|--------|--------|--------|--------|--------|---------|---------|---------|
| 140-ton row charge | 2BN | x | 1.72 | 2.87 | 2.87 | 2.10 | 0.86 | 1.62 | 2.10 | 1.91 | 1.53 | 0.96 | 0.48 | 0.19 |
| | | y | 0.67 | 0.78 | 1.34 | 1.23 | 0.56 | 0.33 | 0.67 | 0.56 | 0.47 | 0.33 | 0.23 | 0.12 |
| | | z | 0.97 | 1.84 | 2.16 | 1.30 | 4.00 | 5.40 | 5.40 | 4.64 | 2.38 | 1.73 | 0.97 | 0.54 |
| | 3N | x | 0.23 | 0.25 | 0.18 | 0.27 | 0.21 | 0.20 | 0.14 | 0.083 | 0.062 | 0.041 | 0.021 | - |
| | | y | 0.094 | 0.19 | 0.17 | 0.15 | 0.11 | 0.12 | 0.11 | 0.11 | 0.047 | 0.024 | 0.012 | - |
| | | z | 0.19 | 0.31 | 0.20 | 0.36 | 0.63 | 0.45 | 0.22 | 0.18 | 0.13 | 0.078 | 0.045 | 0.033 |
| | 4N | x | 0.052 | 0.042 | 0.057 | 0.12 | 0.18 | 0.15 | 0.083 | 0.052 | 0.037 | 0.026 | 0.021 | 0.010 |
| | | y | 0.029 | 0.046 | 0.032 | 0.072 | 0.13 | 0.075 | 0.046 | 0.032 | 0.023 | 0.013 | 0.009 | - |
| | | z | 0.065 | 0.054 | 0.081 | 0.20 | 0.35 | 0.23 | 0.11 | 0.065 | 0.051 | 0.070 | 0.076 | 0.085 |
| | 5N | x | 0.022 | 0.011 | 0.022 | 0.022 | 0.039 | 0.044 | 0.039 | 0.033 | 0.033 | 0.028 | 0.022 | - |
| | | y | 0.013 | 0.007 | - | 0.013 | 0.027 | 0.013 | 0.040 | 0.034 | 0.013 | - | - | - |
| | | z | - | - | 0.011 | 0.045 | 0.068 | 0.057 | 0.085 | 0.11 | 0.14 | 0.13 | 0.13 | 0.068 |
| SD-1 | 2BN | x | 0.008 | 0.010 | 0.031 | 0.036 | 0.019 | 0.013 | 0.008 | 0.010 | 0.013 | 0.008 | - | - |
| | | y | 0.005 | 0.005 | 0.014 | 0.014 | 0.011 | 0.007 | 0.005 | 0.011 | 0.009 | 0.005 | - | - |
| | | z | 0.005 | 0.005 | 0.012 | 0.012 | 0.010 | 0.014 | 0.017 | 0.022 | 0.026 | 0.019 | 0.014 | 0.009 |
| | 6W | x | 0.012 | 0.018 | 0.039 | 0.058 | 0.066 | 0.066 | 0.048 | 0.051 | 0.042 | 0.030 | 0.027 | 0.012 |
| | | y | 0.007 | - | 0.014 | 0.018 | 0.053 | 0.064 | 0.043 | 0.021 | 0.028 | 0.018 | 0.014 | - |
| | | z | 0.008 | 0.011 | 0.039 | 0.044 | 0.044 | 0.048 | 0.033 | 0.048 | 0.069 | 0.066 | 0.066 | 0.061 |
| SD-2 | 2BN | x | 0.008 | 0.019 | 0.050 | 0.053 | 0.029 | 0.015 | 0.015 | 0.015 | 0.017 | 0.009 | - | - |
| | | y | 0.005 | 0.009 | 0.023 | 0.027 | 0.014 | 0.014 | 0.011 | 0.007 | 0.018 | 0.005 | - | - |
| | | z | 0.005 | 0.012 | 0.026 | 0.026 | 0.014 | 0.017 | 0.024 | 0.034 | 0.036 | 0.034 | 0.014 | - |
| | 6W | x | 0.012 | 0.030 | 0.060 | 0.072 | 0.072 | 0.072 | 0.042 | 0.036 | 0.042 | 0.033 | 0.030 | 0.015 |
| | | y | 0.007 | 0.018 | 0.036 | 0.064 | 0.078 | 0.050 | 0.028 | 0.025 | 0.025 | 0.021 | 0.014 | - |
| | | z | 0.008 | 0.025 | 0.050 | 0.056 | 0.061 | 0.044 | 0.033 | 0.050 | 0.066 | 0.077 | 0.069 | 0.061 |

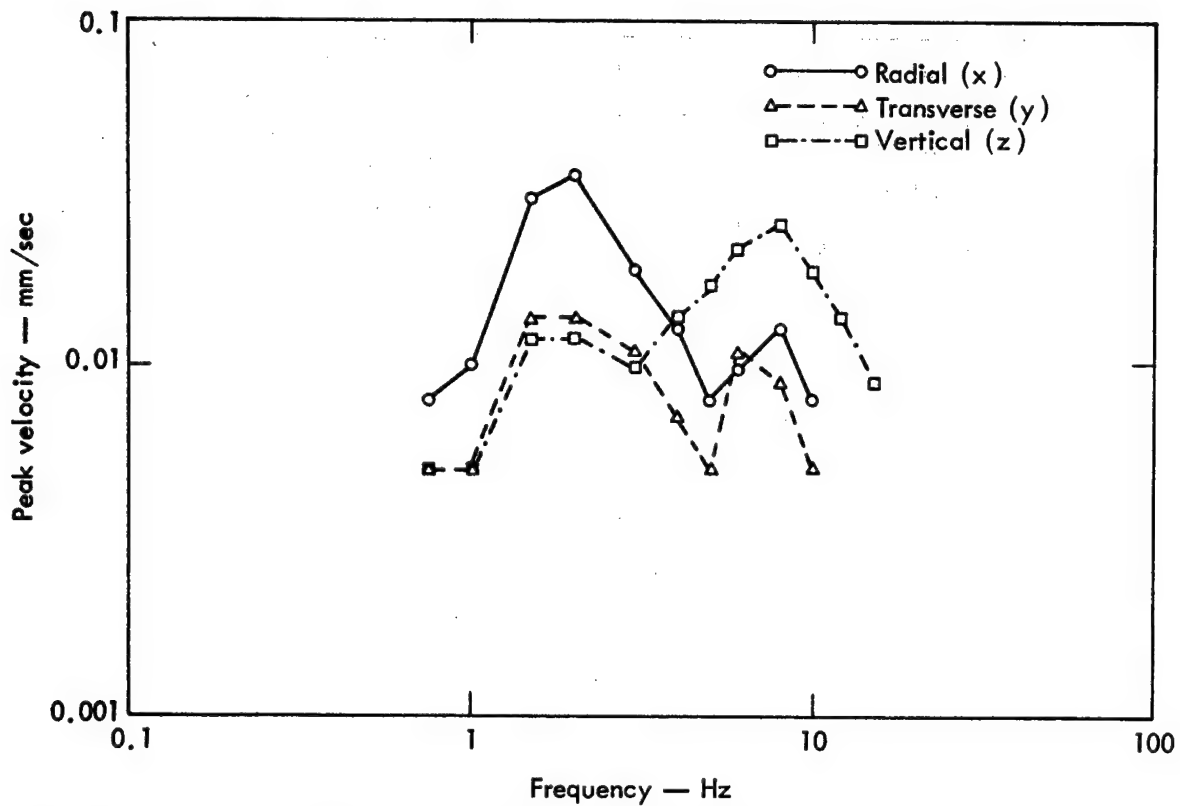


Fig. 9. Comb filter peak velocity as a function of frequency for Station 2BN, Pre-Gondola II SD-1 Event.

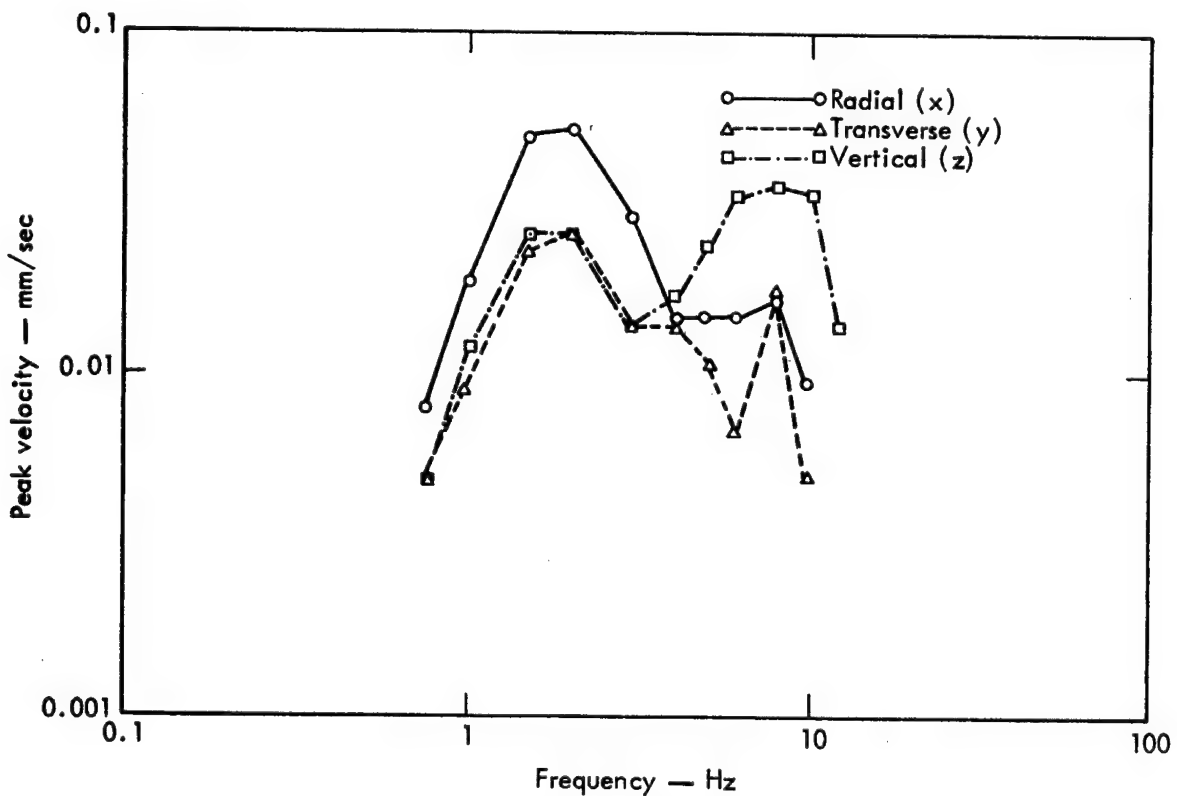


Fig. 10. Comb filter peak velocity as a function of frequency for Station 2BN, Pre-Gondola II SD-2 Event.

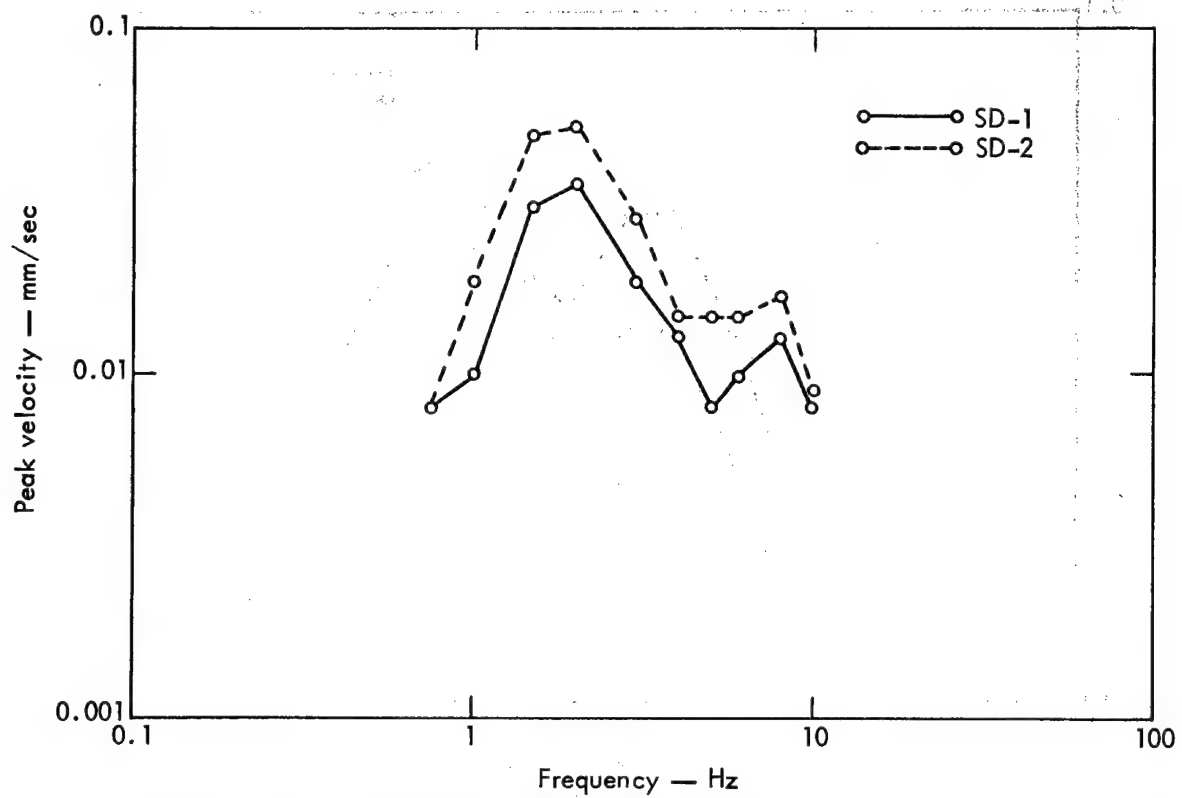


Fig. 11. Comparison of comb filter peak velocities of radial motion at Station 2BN for SD-1 and SD-2 Events.

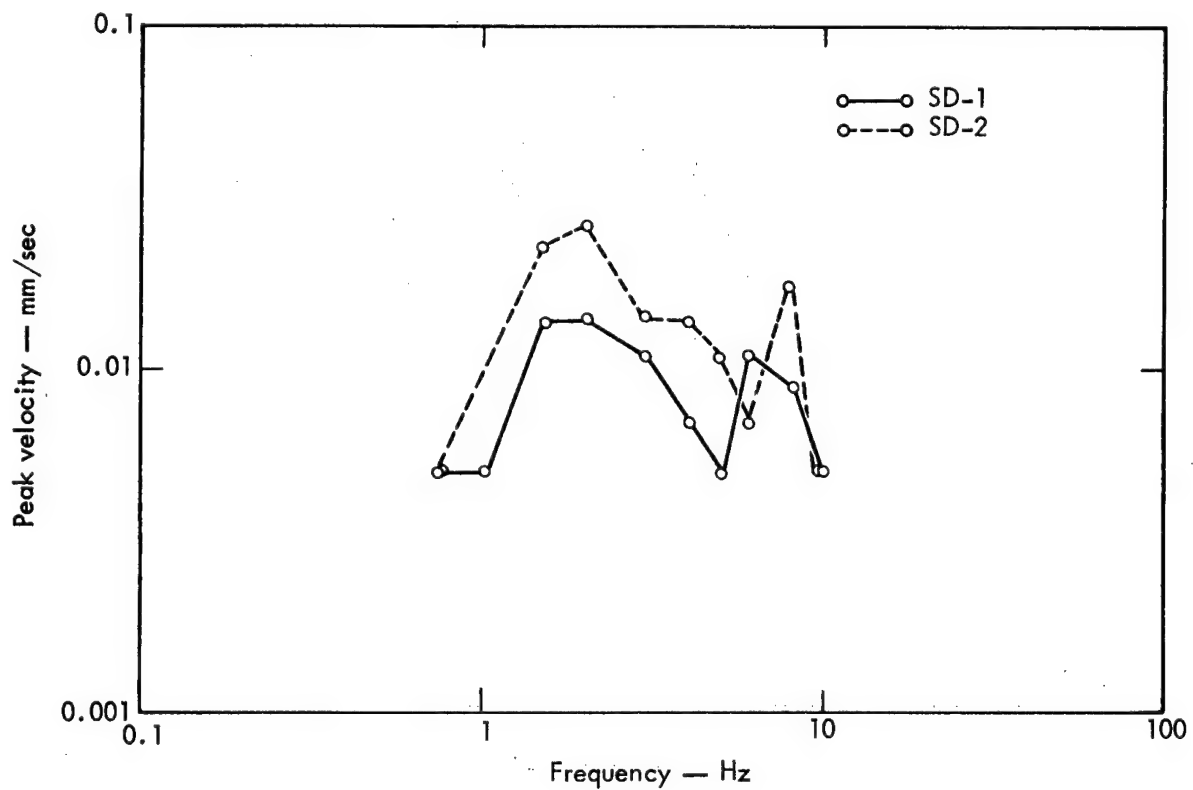


Fig. 12. Comparison of comb filter peak velocities of transverse motion at Station 2BN for SD-1 and SD-2 Events.

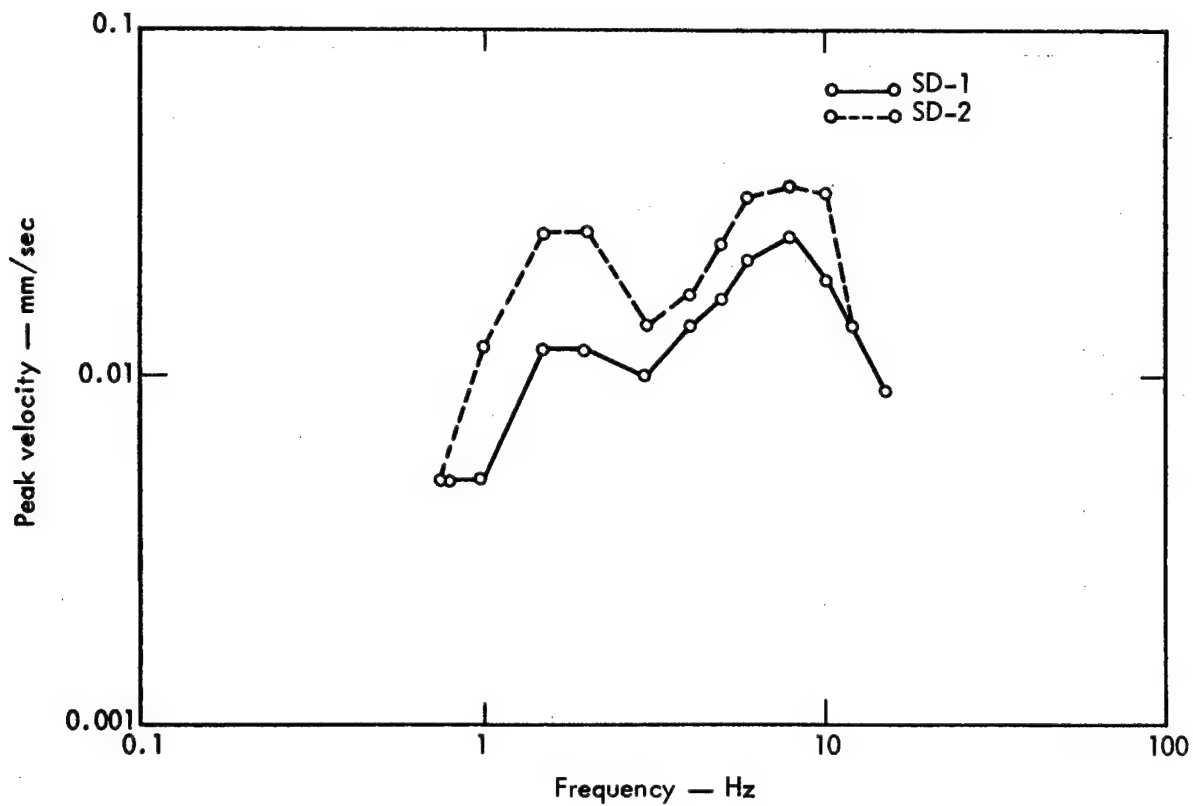


Fig. 13. Comparison of comb filter peak velocities of vertical motion at Station 2BN for SD-1 and SD-2 Events.

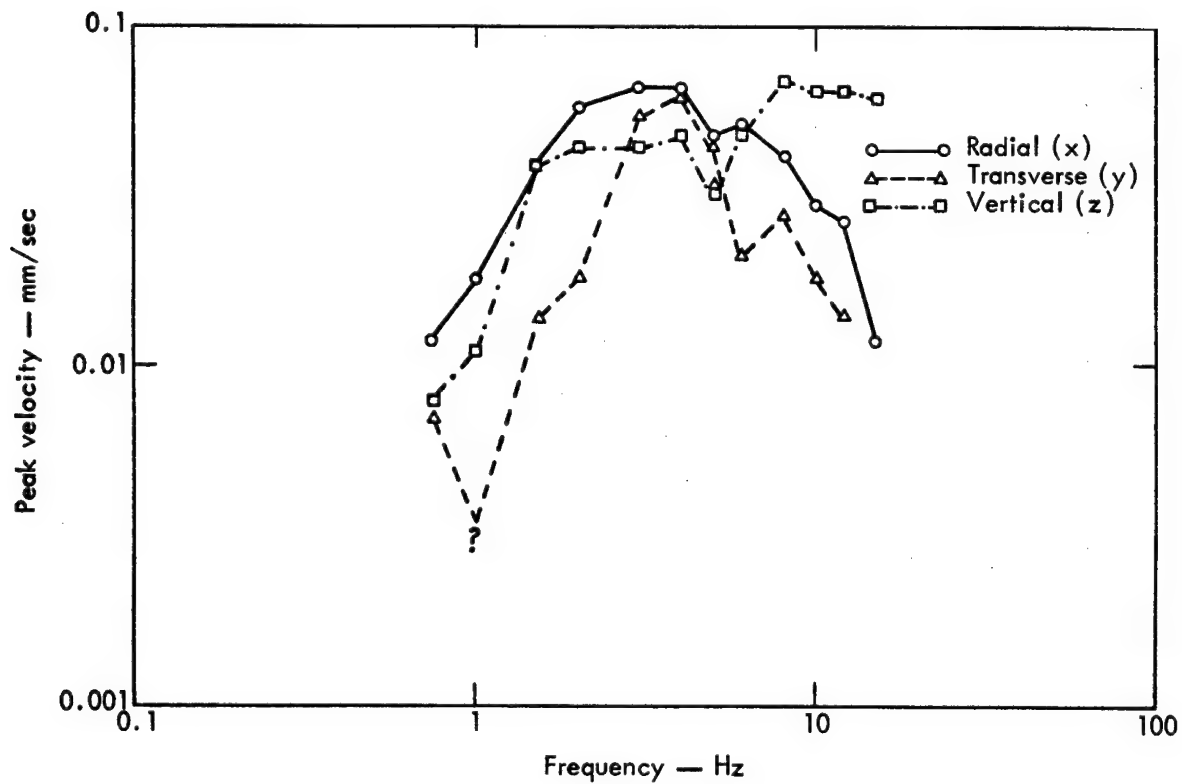


Fig. 14. Comb filter peak velocity as a function of frequency for Station 6W, Pre-Gondola II SD-1 Event.

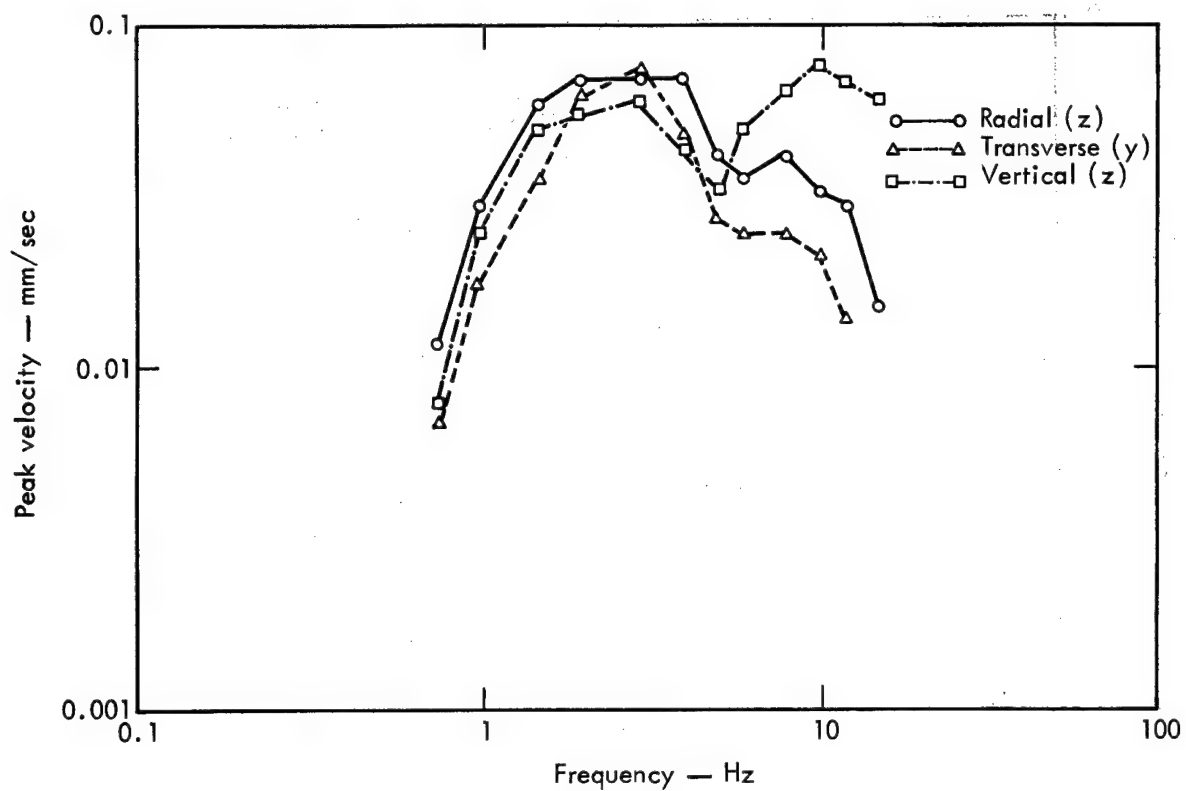


Fig. 15. Comb filter peak velocity as a function of frequency for Station 6W, Pre-Gondola II SD-2 Event.

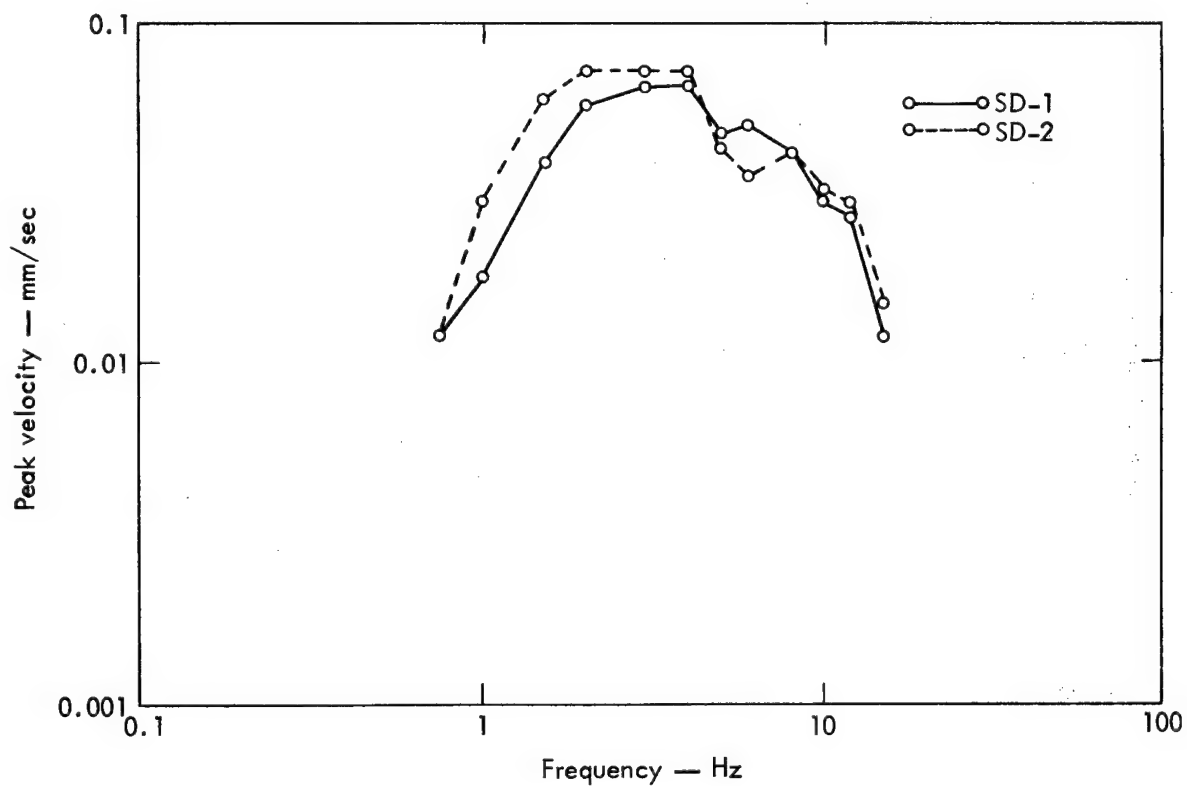


Fig. 16. Comparison of comb filter peak velocities of radial motion at Station 6W, for SD-1 and SD-2 Events.

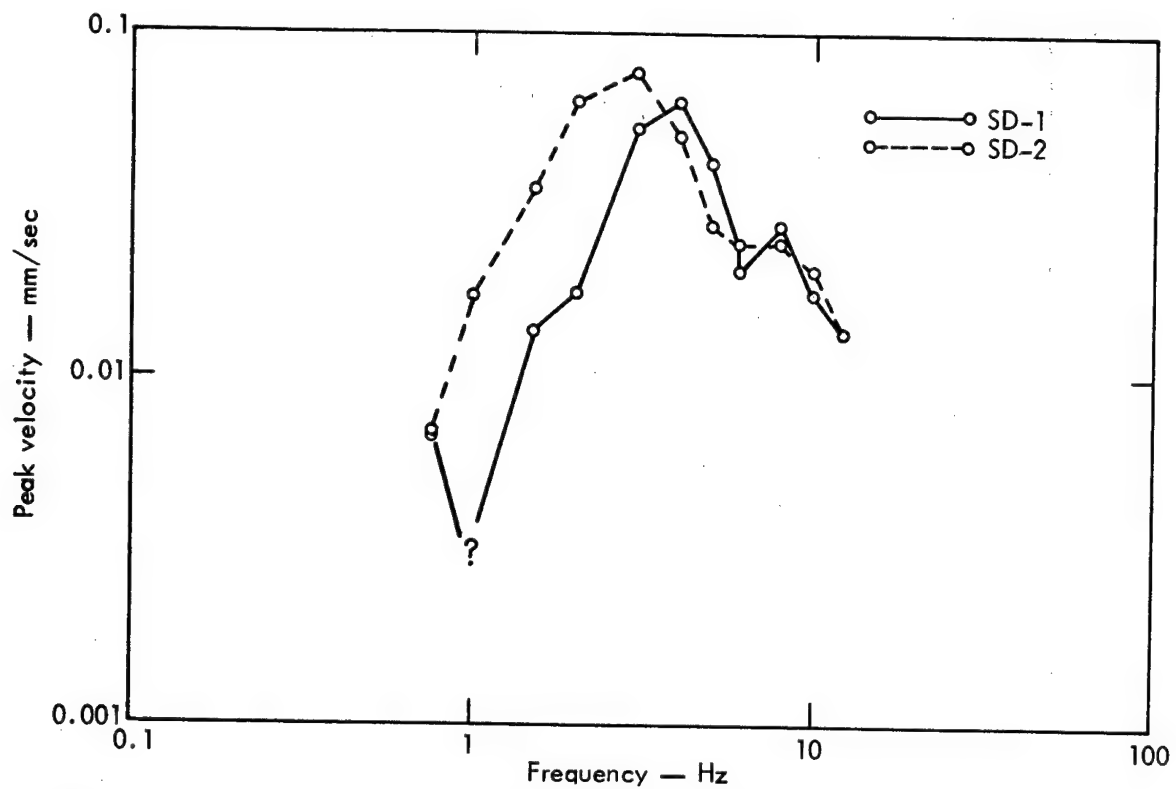


Fig. 17. Comparison of comb filter peak velocities of transverse motion at Station 6W for SD-1 and SD-2 Events.

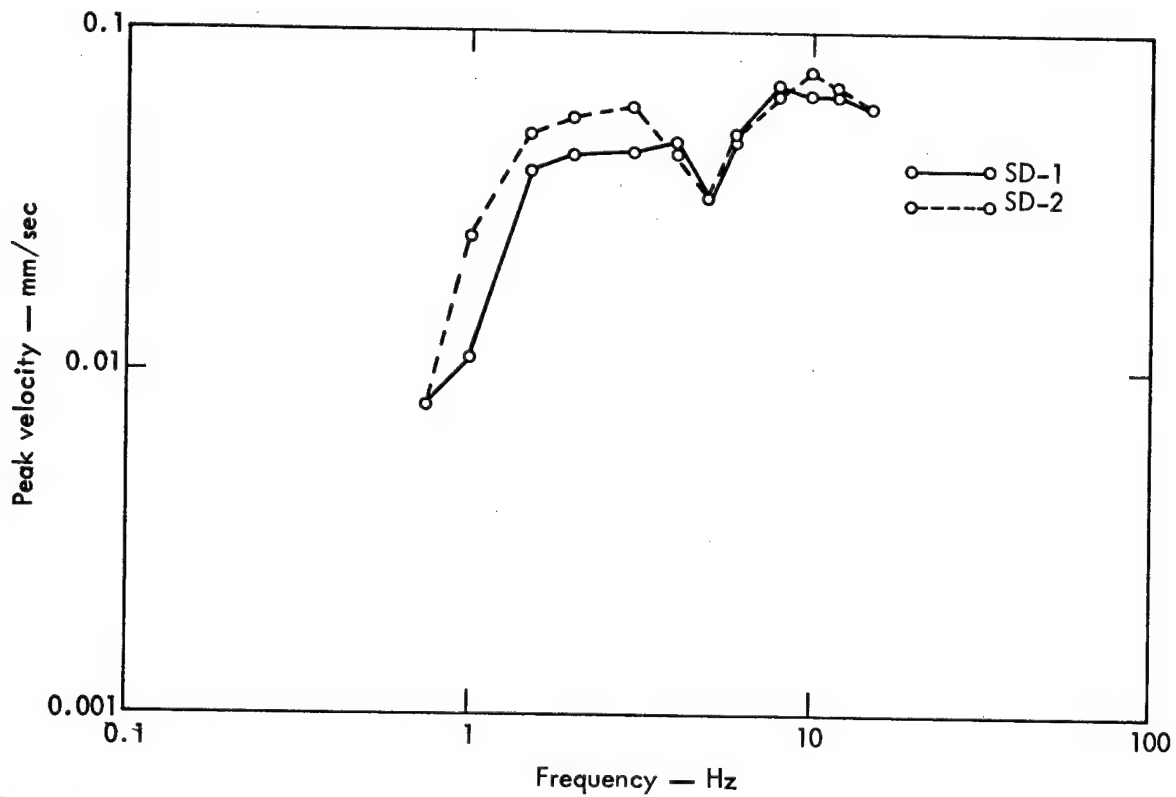


Fig. 18. Comparison of comb filter peak velocities of vertical motion at Station 6W for SD-1 and SD-2 Events.

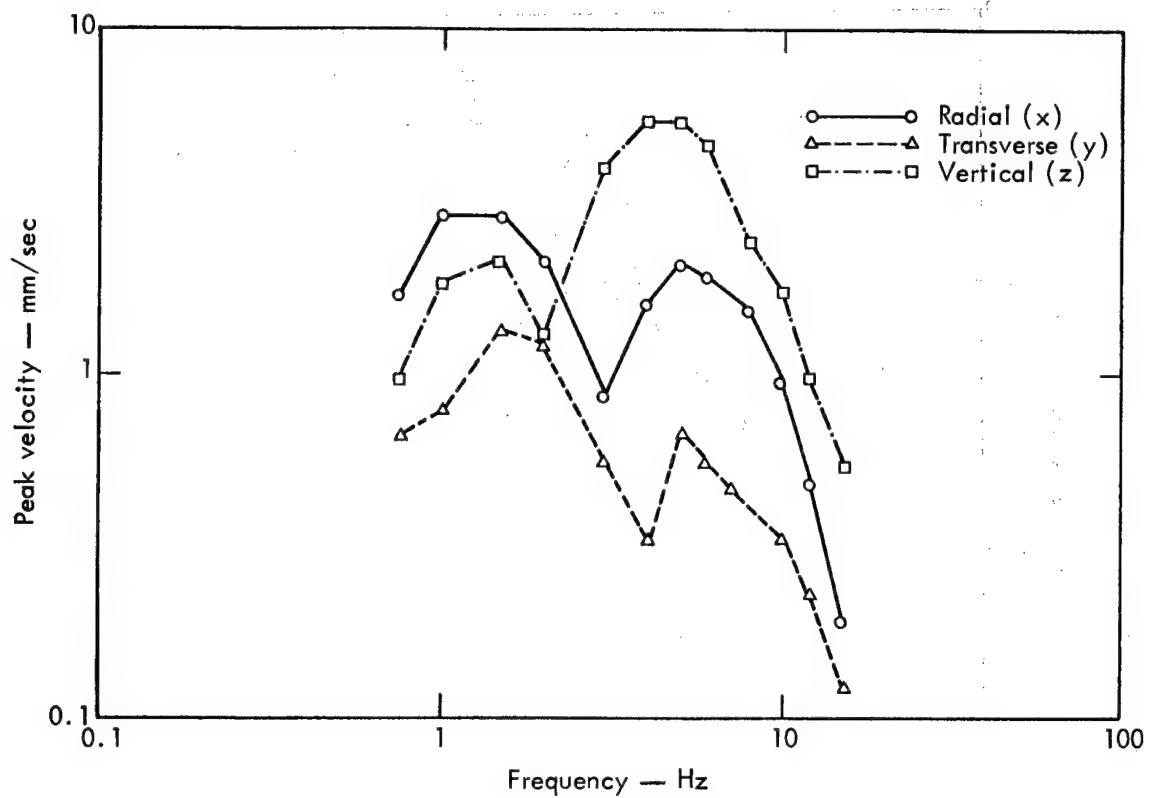


Fig. 19. Comb filter peak velocity as a function of frequency for Station 2BN, Pre-Gondola II 140-ton row charge.

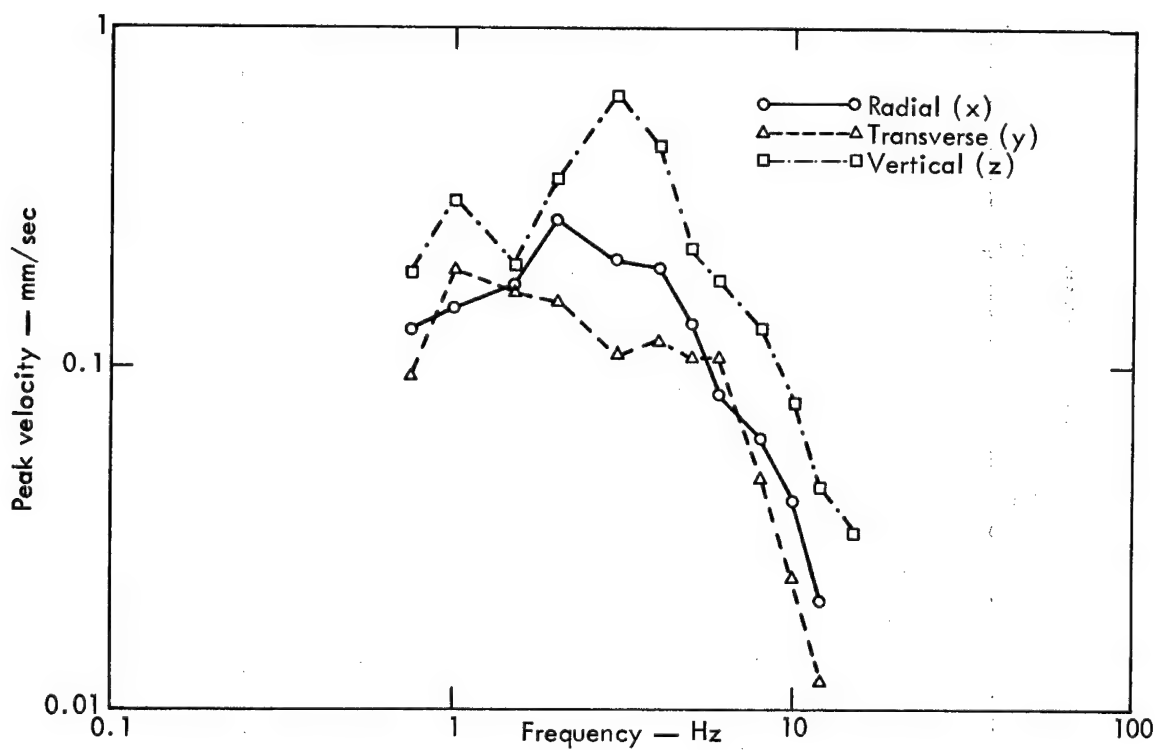


Fig. 20. Comb filter peak velocity as a function of frequency for Station 3N, Pre-Gondola II 140-ton row charge.

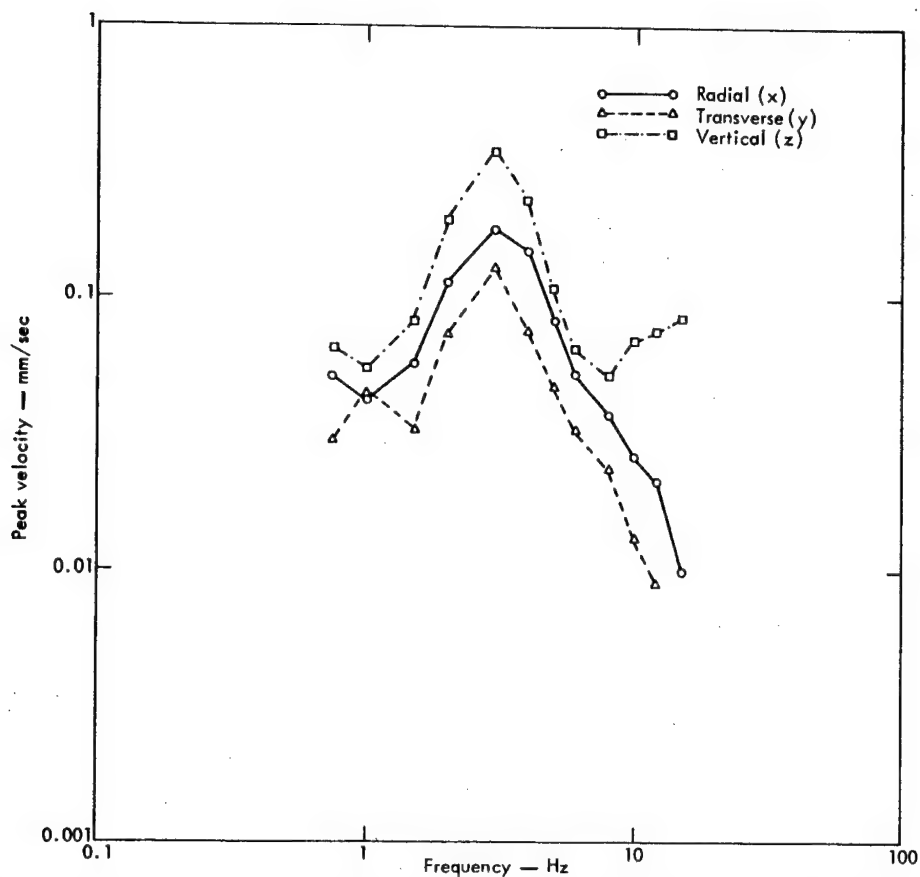


Fig. 21. Comb filter peak velocity as a function of frequency for Station 4N, Pre-Gondola II 140-ton row charge.

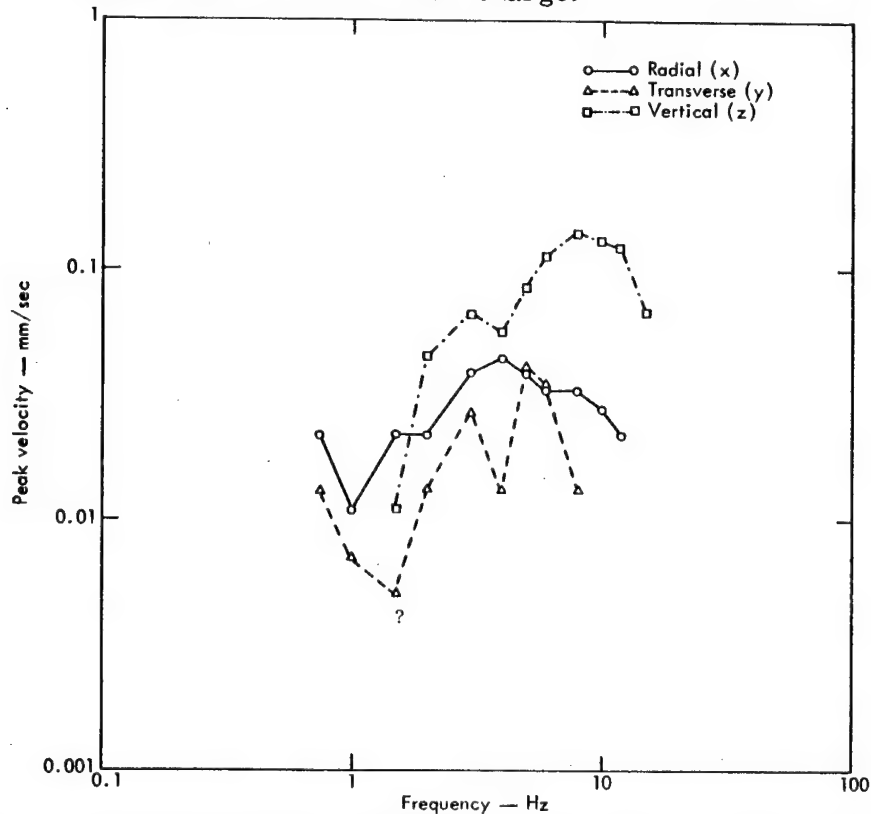


Fig. 22. Comb filter peak velocity as a function of frequency for Station 5N, Pre-Gondola II 140-ton row charge.

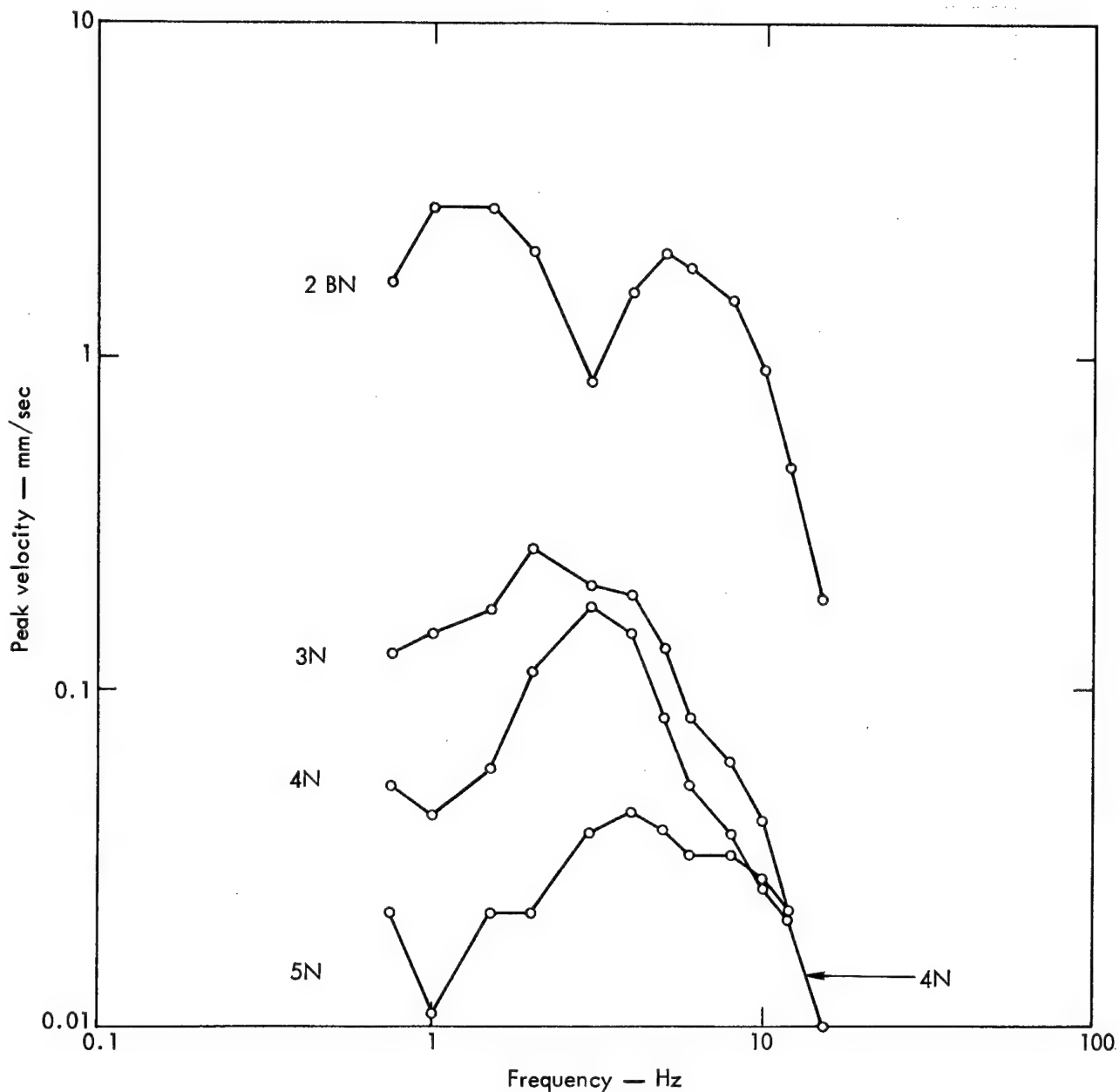


Fig. 23. Comb filter peak velocity of radial components for all stations, Pre-Gondola II 140-ton row charge.

attenuation α , (see Appendix B) with distance for the peak amplitudes from the CFPV's is shown in Fig. 26.

POWER SPECTRAL DENSITY

Table V lists the peak density (PSD_{max}), the frequency at which it occurs, and the

total energies (E and $\sum E$) for each component on all stations and events.

Comparisons of the PSD's for each component (including the resultant) at Station 2BN for three yields are shown in Figs. 27 through 30. Comparisons of the PSD's for each component and resultant

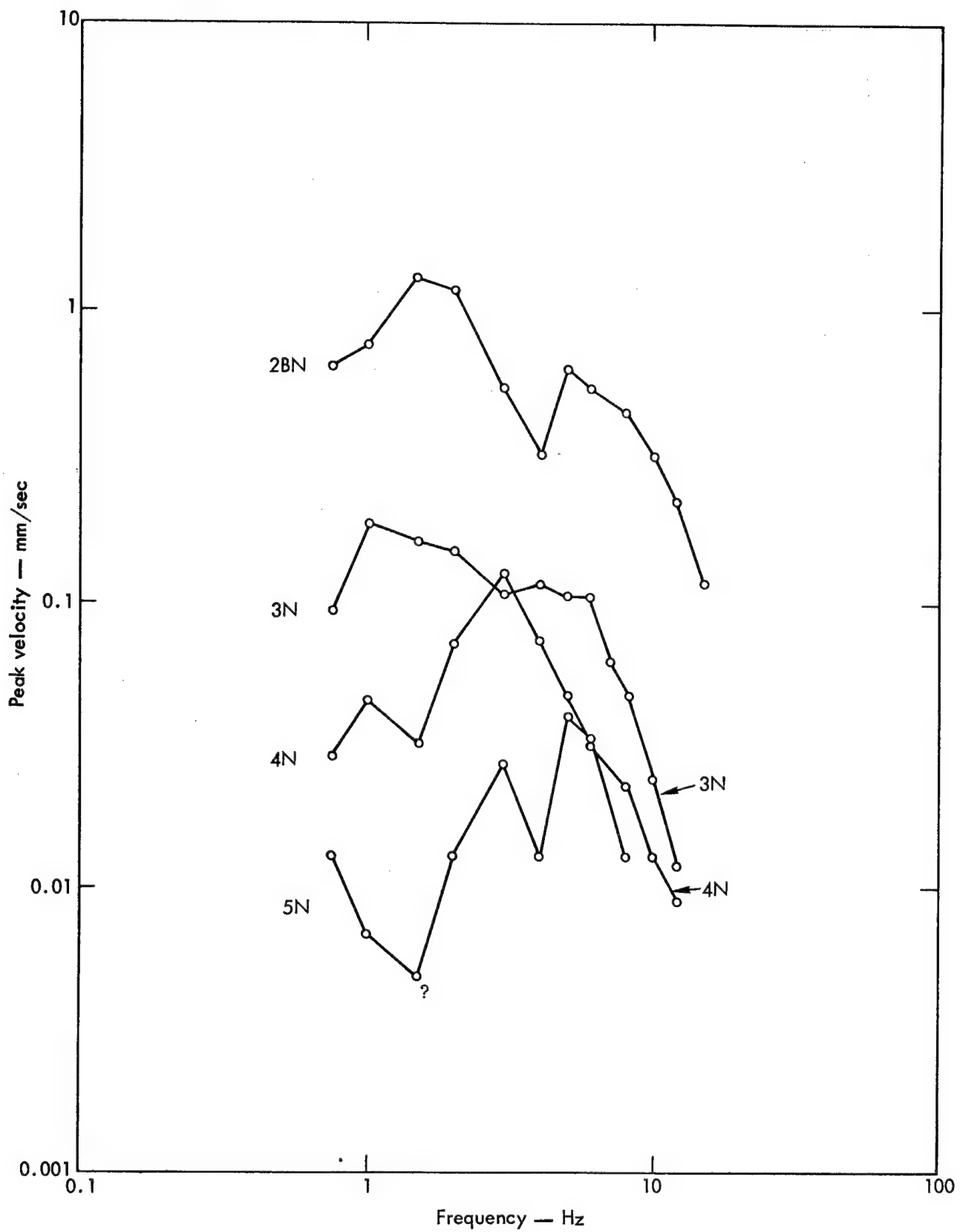


Fig. 24. Comb filter peak velocities for all stations of transverse components, Pre-Gondola II 140-ton row charge.

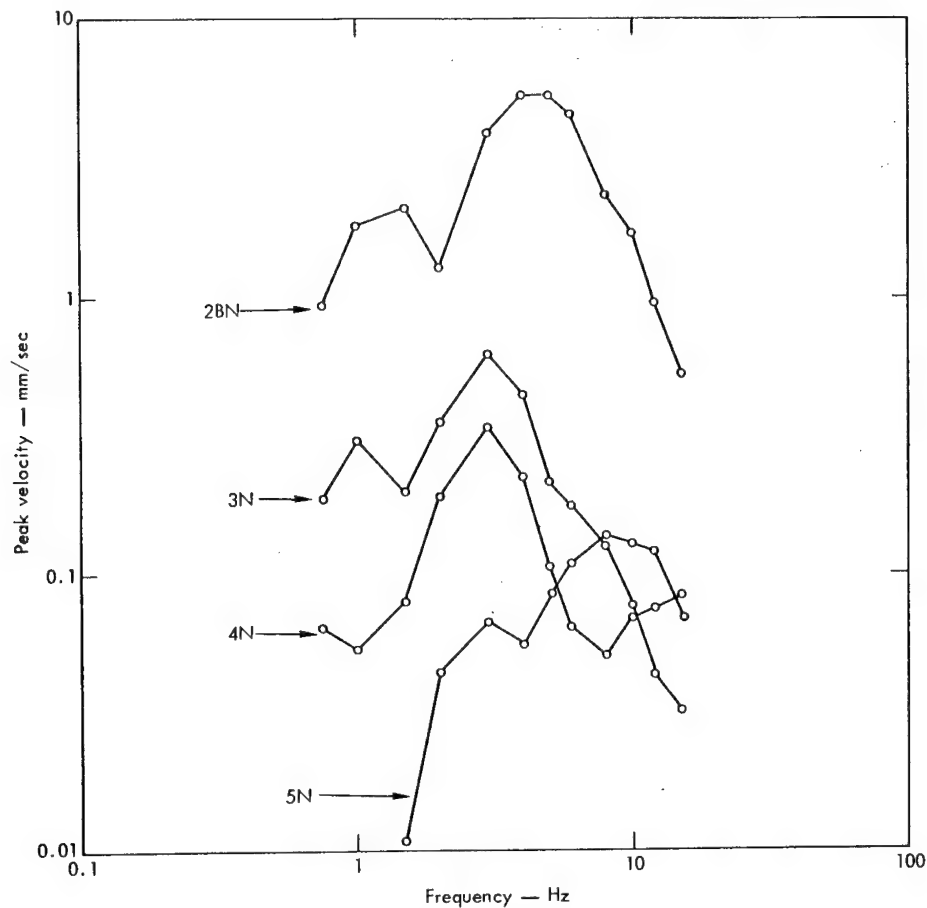


Fig. 25. Comb filter peak velocity of vertical components for all stations, Pre-Gondola II 140-ton row charge, as a function of frequency. (Note that at low frequencies attenuation is about as expected; at high frequencies the short duration-high amplitude pulses in signals on Station 5N considerably alter relationship of V_p vs distance.)

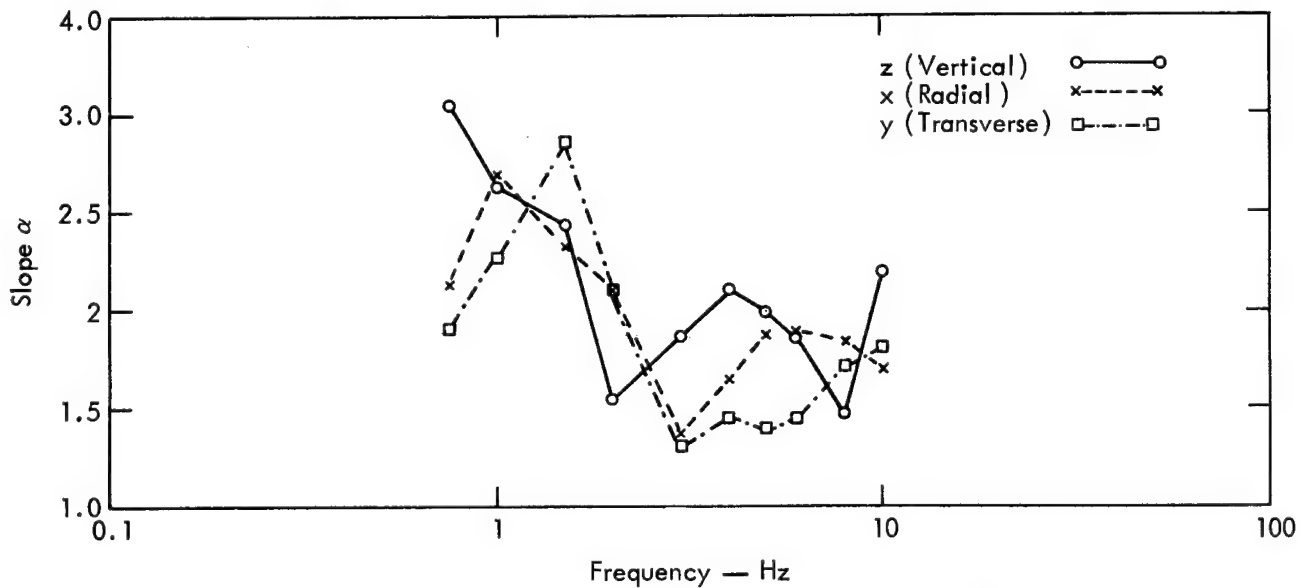


Fig. 26. Plot of α (frequency) from equation: $CFPV(R, f) = K_f R^{-\alpha(f)}$; this represents attenuation slope for comb filter peak velocity as a function of frequency (Pre-Gondola II).

Table V. Power spectral density: peak density values and total energy.

| Event | Station | Component | Peak density | | Total energy (E and $\sum E$) (mm/sec) ² |
|---|---------|-----------|------------------------------------|--------------------------------|--|
| | | | Value (mm/sec) ² sec | Frequency ^a (Hz) | |
| Pre-Gondola II 140-ton row charge | 2BN | x | 0.805 | 1.17 | 0.633 E |
| | | y | 0.164 | 1.50 | 0.250 E |
| | | z | 0.255 | 1.33 | 0.570 E |
| | | Res | 1.20 | 1.17 | 1.453 $\sum E$ |
| | 3N | x | 2.26×10^{-3} | 1.87 | 5.65×10^{-3} |
| | | y | 2.72×10^{-3} | 1.67 | 2.89×10^{-3} |
| | | z | 7.74×10^{-3} | 2.67 | 8.06×10^{-3} |
| | | Res | 10.5×10^{-3} | 2.67 | 16.60×10^{-3} |
| | 4N | x | 1.24×10^{-3} | 2.67 | 1.67×10^{-3} |
| | | y | 3.43×10^{-4} | 2.83 | 0.473×10^{-3} |
| | | z | 2.10×10^{-3} | 2.83 | 2.76×10^{-3} |
| | | Res | 3.55×10^{-3} | 2.83 | 4.903×10^{-3} |
| | 5N | x | 1.54×10^{-4} | 2.83 | 2.83×10^{-4} |
| | | y | 0.274×10^{-4} | 4.67 | 1.36×10^{-4} |
| | | z | 2.57×10^{-4} | 2.67 | 3.51×10^{-4} |
| | | Res | 4.30×10^{-4} | 2.67 | 7.70×10^{-4} |
| SD-1 | 2BN | x | 4.68×10^{-5} | 1.83 | 4.4×10^{-5} |
| | | y | 2.51×10^{-5} | 1.63 | 4.1×10^{-5} |
| | | z | 1.62×10^{-5} | 1.50 | 4.1×10^{-5} |
| | | Res | 7.42×10^{-5} | 1.83 | 12.6×10^{-5} |
| SD-2 | 2BN | x | 11.40×10^{-5} | 1.83 | 8.8×10^{-5} |
| | | y | 5.12×10^{-5} | 1.67 | 7.1×10^{-5} |
| | | z | 4.06×10^{-5} | 1.50 | 7.7×10^{-5} |
| | | Res | 17.4×10^{-5} | 1.83 | 23.6×10^{-5} |
| | 6W | x | 2.492×10^{-4} | 1.67 | 5.12×10^{-4} |
| | | y | 3.28×10^{-4} | 2.17 | 4.24×10^{-4} |
| | | z | 2.35×10^{-4} | 3.00 | 3.84×10^{-4} |
| | | Res | 6.35×10^{-4} | 2.17 | 13.2×10^{-4} |
| SD-1 | 6W | x | 0.64×10^{-4} | 2.17 | 1.31×10^{-4} |
| | | y | 1.12×10^{-4} | 3.67 | 1.95×10^{-4} |
| | | z | 1.29×10^{-4} | 3.00 | 2.67×10^{-4} |
| | | Res | 2.45×10^{-4} | 3.16 | 5.93×10^{-4} |
| Pre-Gondola I Bravo | 2BN | x | 2.17×10^{-2} | 1.17 | 2.40×10^{-2} |
| | | y | 0.66×10^{-2} | 1.17 | 0.70×10^{-2} |
| | | z | 0.97×10^{-2} | 1.33 | 2.05×10^{-2} |
| | | Res | 3.61×10^{-2} | 1.33 | 5.15×10^{-2} |
| | 3N | x | 9.09×10^{-4} | 7.50 | 29.03×10^{-4b} |
| | | | 8.06×10^{-4} | 1.50 | |
| | | y | 4.37×10^{-4} | 7.50 | 12.91×10^{-4b} |
| | | | 2.17×10^{-4} | 1.83 | |
| | | z | 3.94×10^{-4} | 7.50 | 14.69×10^{-4b} |
| | | | 3.43×10^{-4} | 2.67 | |
| | | Res | 17.40×10^{-4} | 7.50 | 56.63×10^{-4b} |
| | | | 9.57×10^{-4} | 1.50 | |
| | 4N | x | 14.77×10^{-6} | 3.50 | 26.95×10^{-6} |
| | | y | 2.92×10^{-6} | 2.83 | 6.89×10^{-6} |
| | | z | 13.58×10^{-6} | 2.83 | 23.34×10^{-6} |
| | | Res | 28.07×10^{-6} | 2.83 | 57.18×10^{-6} |
| | 5N | x | 7.00×10^{-6} | 1.67 | 16.14×10^{-6} |
| | | y | 2.75×10^{-6} | 5.00 | 8.96×10^{-6} |
| | | z | 8.81×10^{-6} | 6.50 | 39.88×10^{-6} |
| | | Res | 13.96×10^{-6} | 2.67 | 64.98×10^{-6} |
| Alfa | 2BN | x | 7.36×10^{-2} | 1.33 | 8.58×10^{-2} |
| | | y | 0.736×10^{-2} | 1.87 | 1.47×10^{-2} |
| | | z | 2.46×10^{-2} | 1.50 | 6.91×10^{-2} |
| | | Res | 10.26×10^{-2} | 1.33 | 16.96×10^{-2} |
| Charlie | 2BN | x | 2.45×10^{-2} | 1.33 | 2.67×10^{-2} |
| | | y | 0.535×10^{-2} | 1.67 | 0.65×10^{-2} |
| | | z | 1.16×10^{-2} | 1.33 | 3.02×10^{-2} |
| | | Res | 3.96×10^{-2} | 1.33 | 6.34×10^{-2} |
| Delta | 2BN | x | 9.53×10^{-2} | 1.33 | 10.46×10^{-2} |
| | | y | 2.29×10^{-2} | 1.67 | 2.16×10^{-2} |
| | | z | 3.36×10^{-2} | 1.33 | 7.68×10^{-2} |
| | | Res | 13.60×10^{-2} | 1.33 | 20.30×10^{-2} |

^aFrequency at which peak density occurs.

^bSpike at 7-1/2 Hz is on all three channels and unexplained at this time.

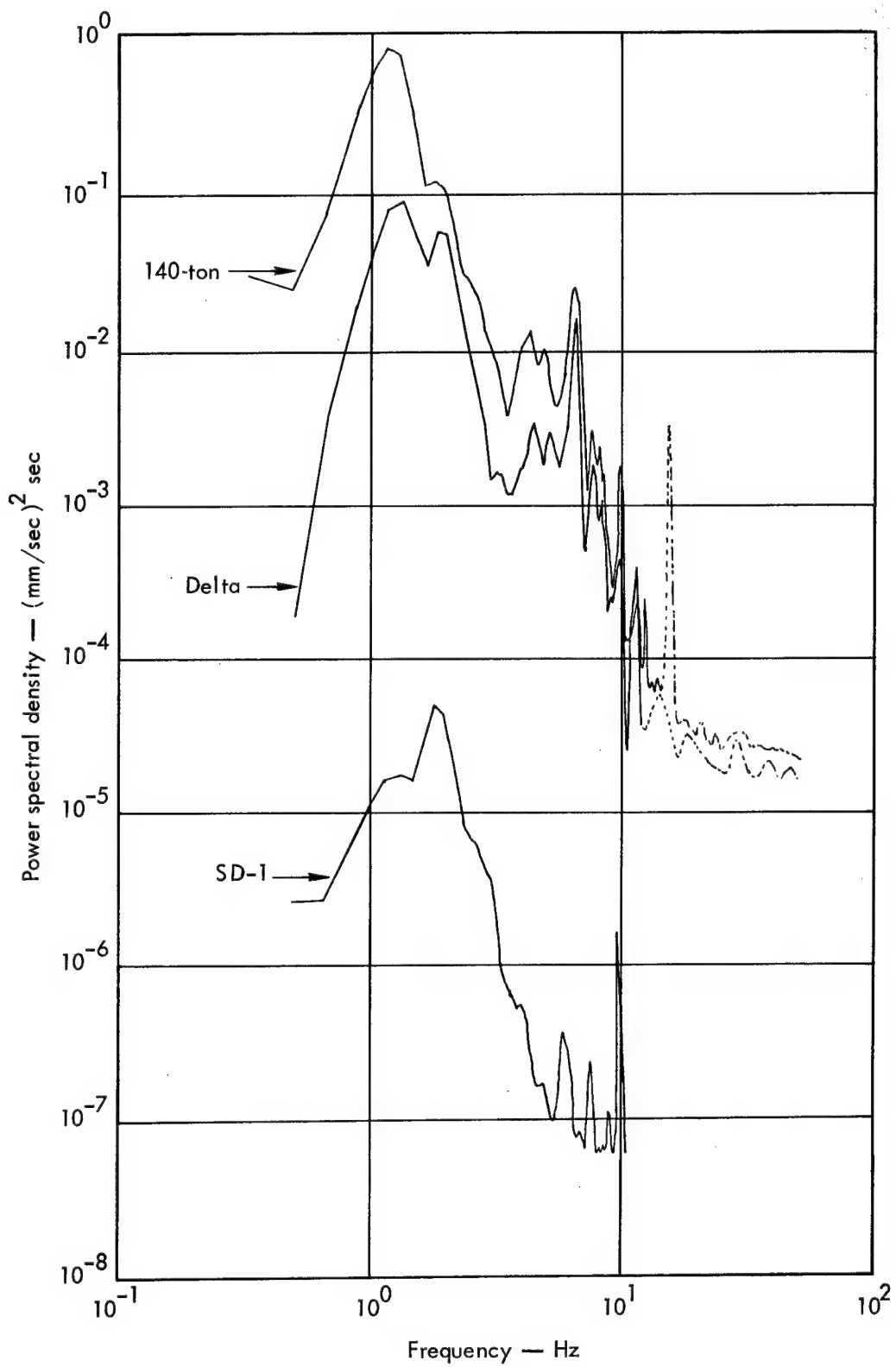


Fig. 27. Radial components at Station 2BN for three yields.

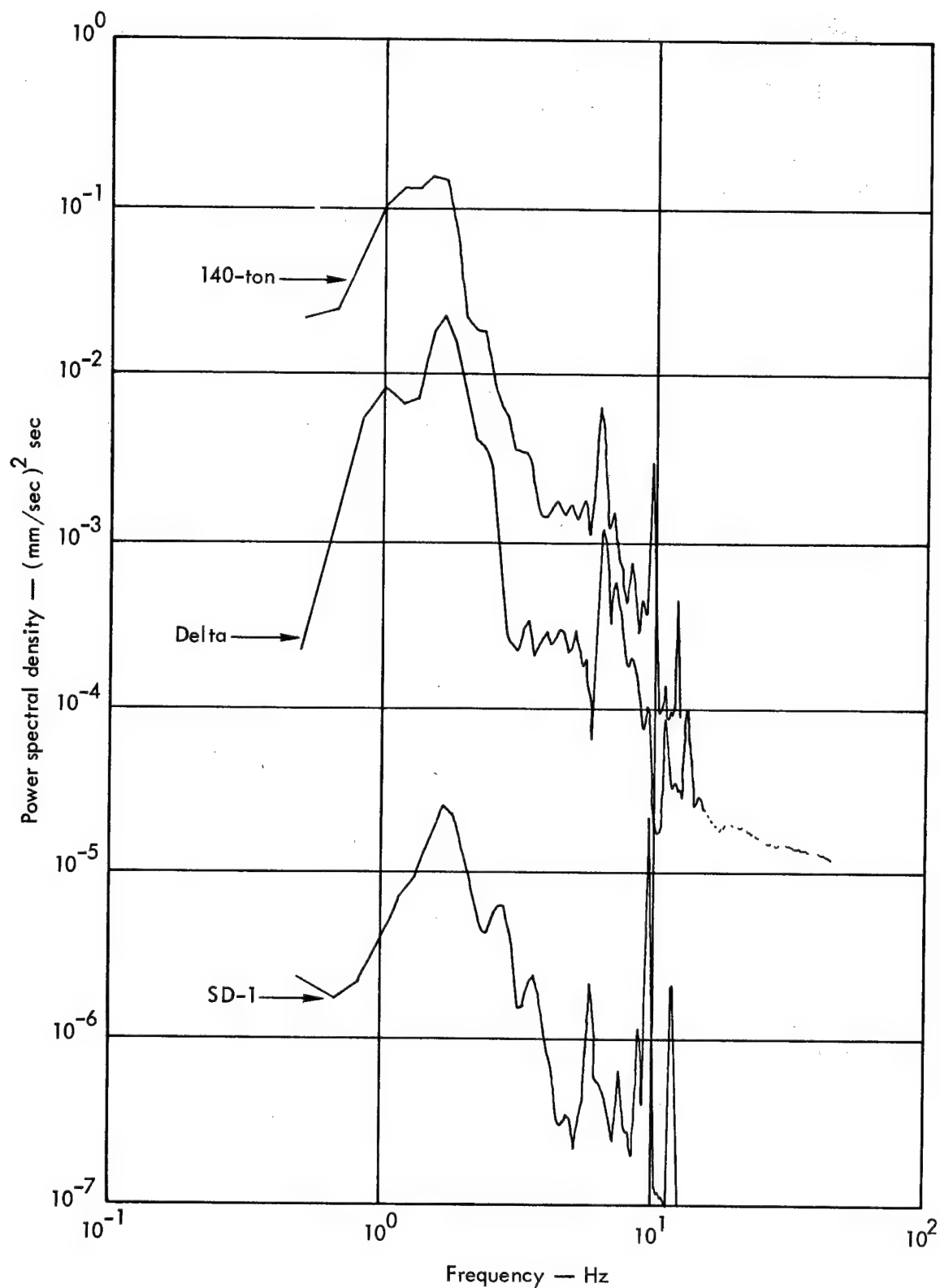


Fig. 28. Transverse components at Station 2BN for three yields.

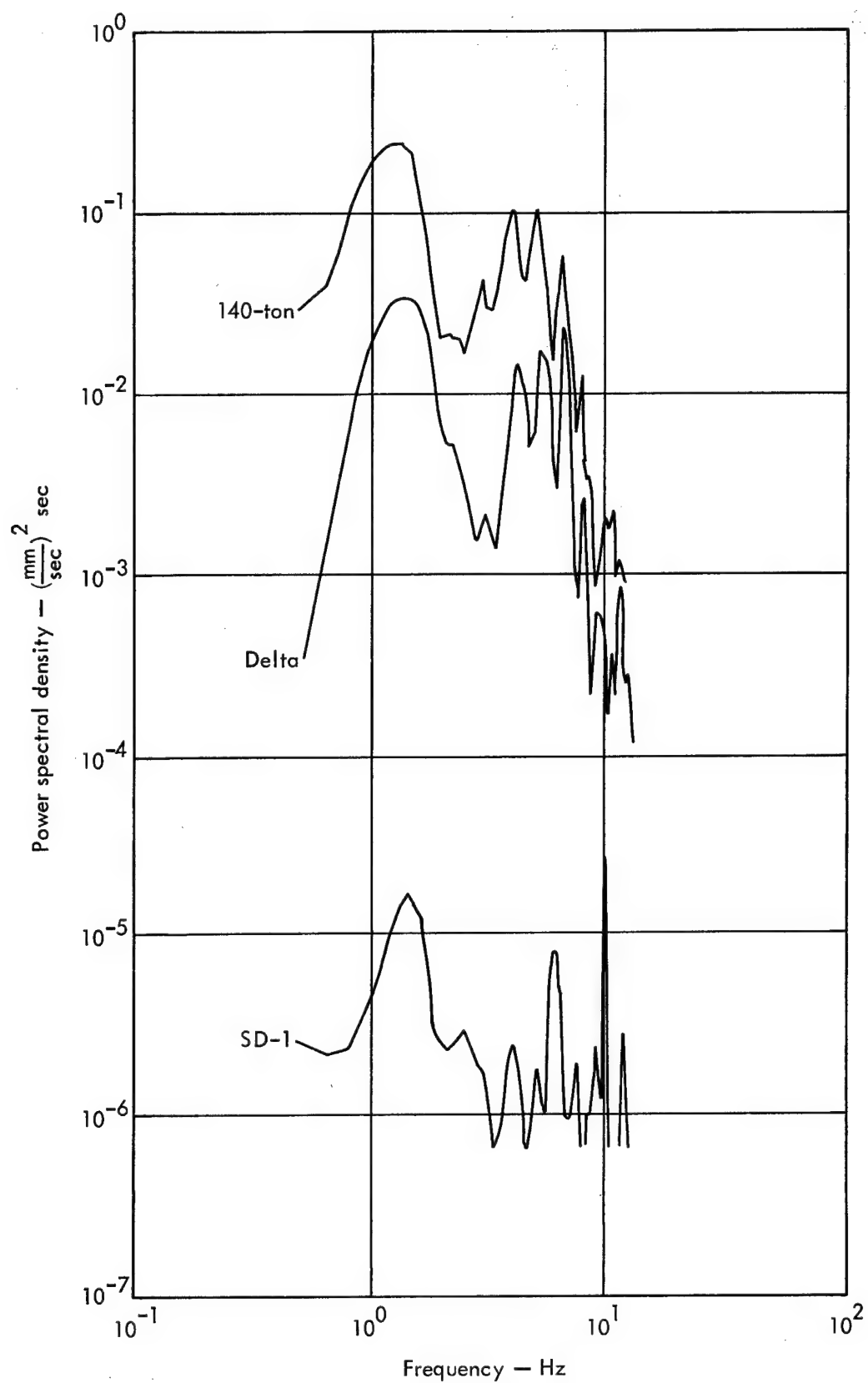


Fig. 29. Vertical components at Station 2BN for three yields.

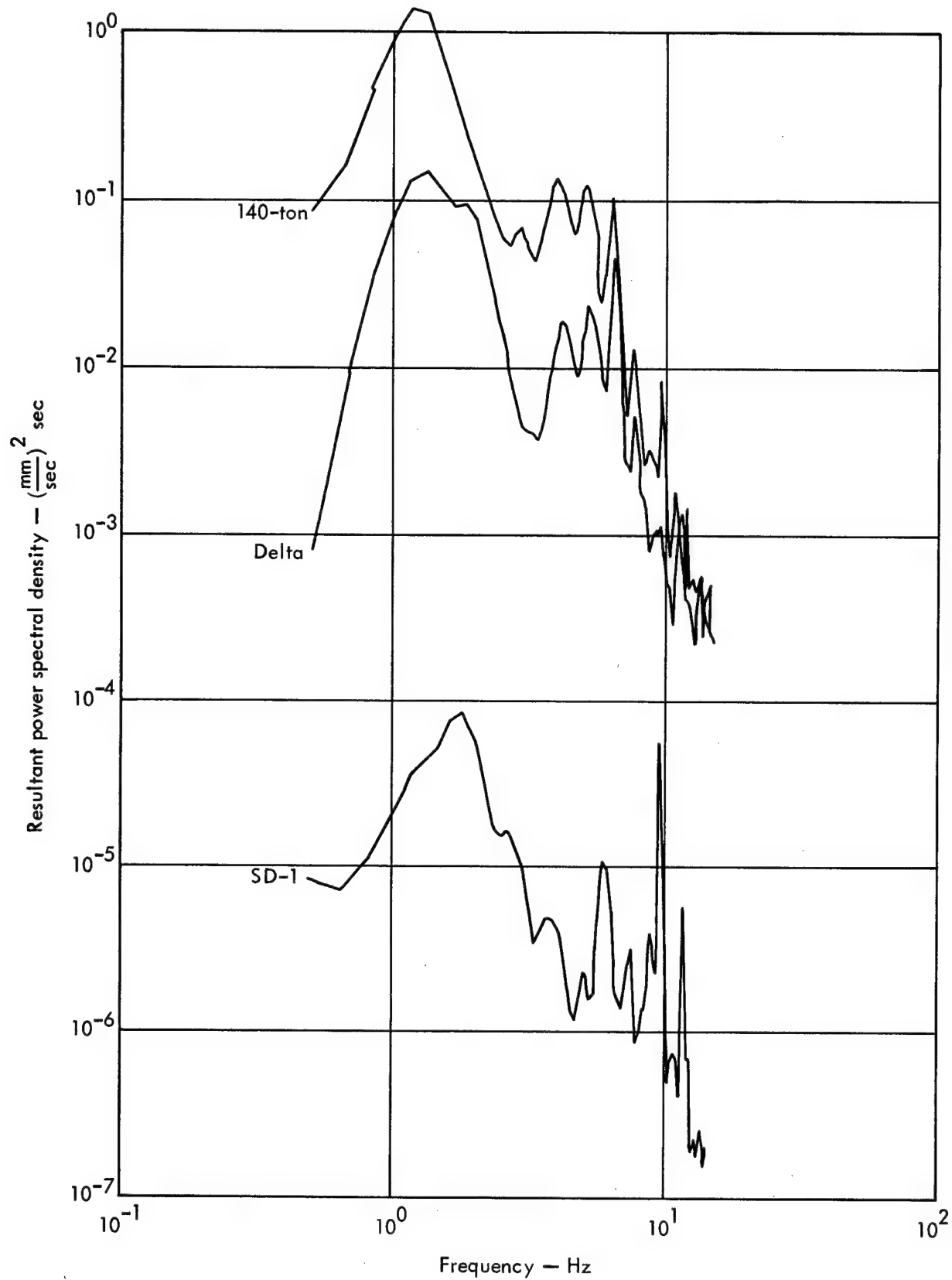


Fig. 30. Resultant power spectral densities at Station 2BN for three yields.

at Stations 6W and 2BN for SD-1 and SD-2 Events are shown in Figs. 31 through 38.

Comparison of PSD's for each component at various distances are shown in Figs. 39 through 42 for the Bravo Event, and in Figs. 43 through 46 for the 140-ton row charge. Figures 47 through 50 show comparisons of the PSD's of the separate

components at Station 2BN for the 20-ton Pre-Gondola Events Alfa, Bravo, Charlie, and Delta to show the effect of depth of burst.

The peak PSD's for Bravo and the 140-ton row charge are plotted against distance in Figs. 51 and 52, respectively. The total energies, E and $\sum E$, are shown in

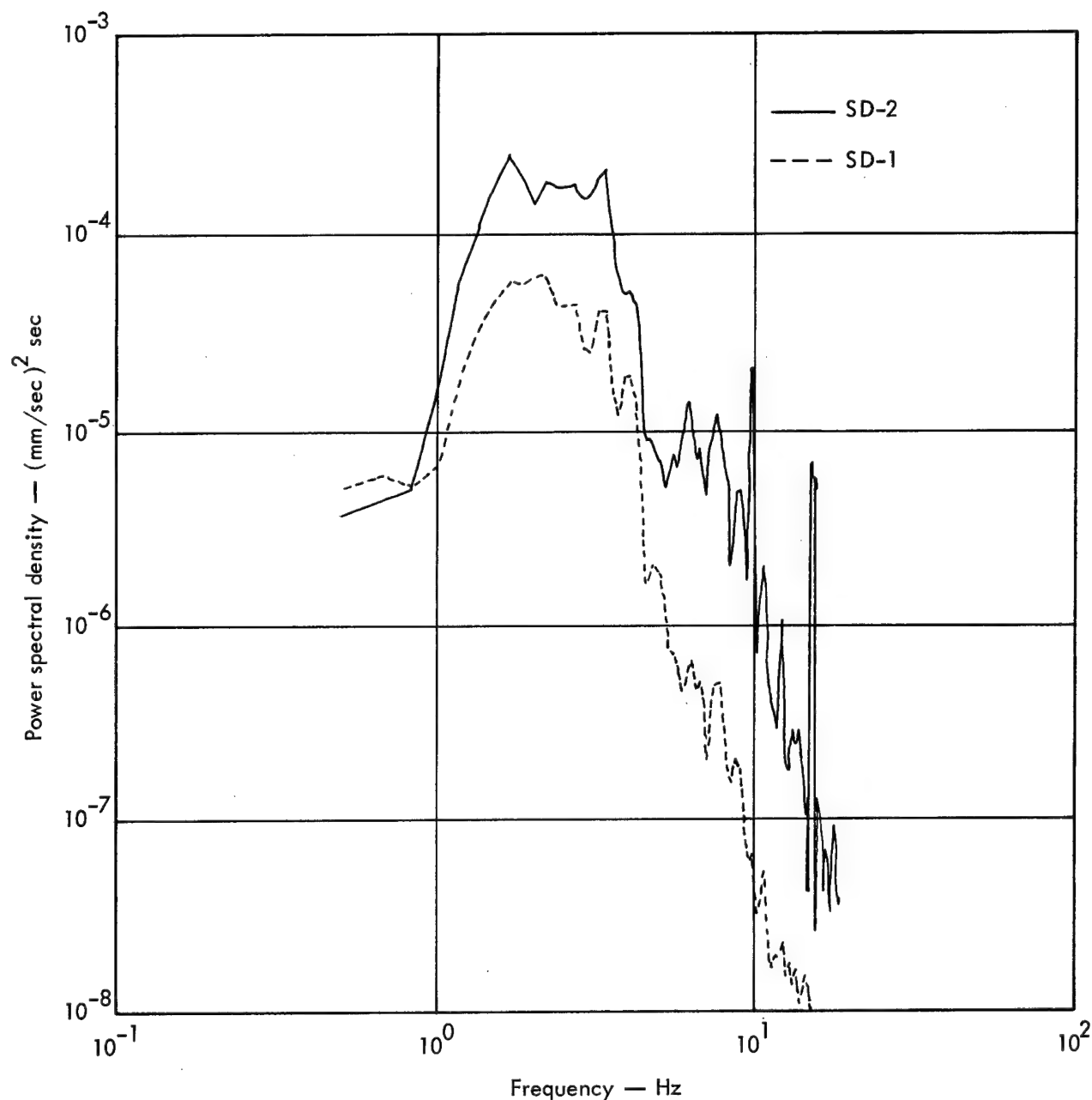


Fig. 31. Radial components at Station 6W for two source configurations.

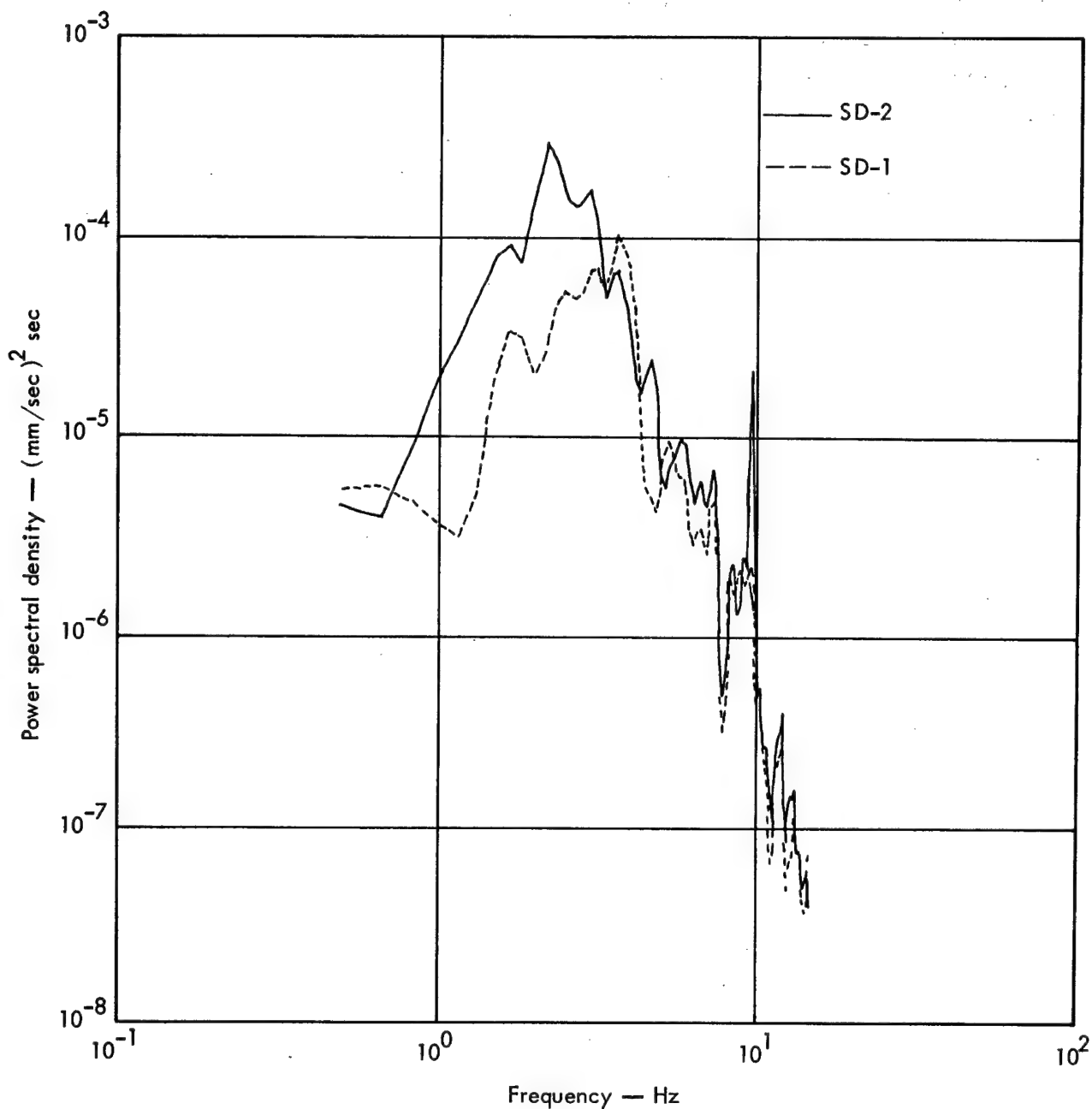


Fig. 32. Transverse components at Station 6W for two source configurations.

Figs. 53 and 54 for the same events. In a manner similar to that done for CFPV's, a plot of the distance attenuation parameter $\alpha(f)$ of the PSD components for each frequency is given in Fig. 55 for the Bravo

Event and in Fig. 56 for the 140-ton row charge. A comparison of the $\alpha(f)$ of the resultant PSD(f) for the two events is given in Fig. 57.

A plot of $\alpha(f)/2$ for the resultant PSD is compared to the CFPV's $\alpha(f)$ in Fig. 58

to compare the results of the two spectral analysis methods. Since there is no resultant component of CFPV, an approximation was made by calculating an $\alpha(f)$ from plots of peak velocity for a given frequency regardless of which component it occurred in.

Figure 59 shows the total station energy ($\sum E$) at Station 2BN for the Pre-Gondola I Events as a function of depth of burst. Figure 60 shows the total energy at Station 2BN normalized to depth of burst and plotted vs yield for three yields and six events.

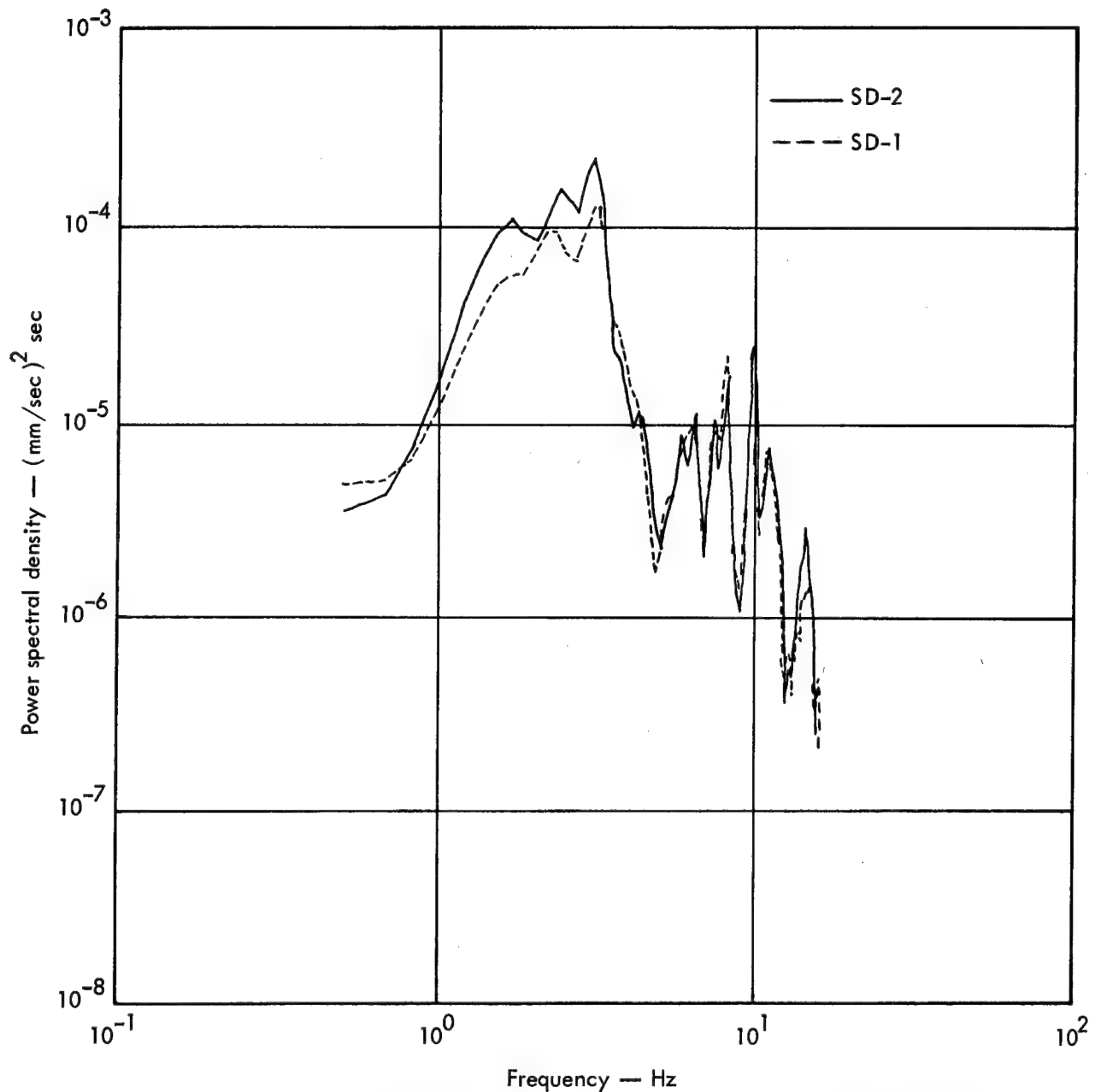


Fig. 33. Vertical components at Station 6W for two source configurations.

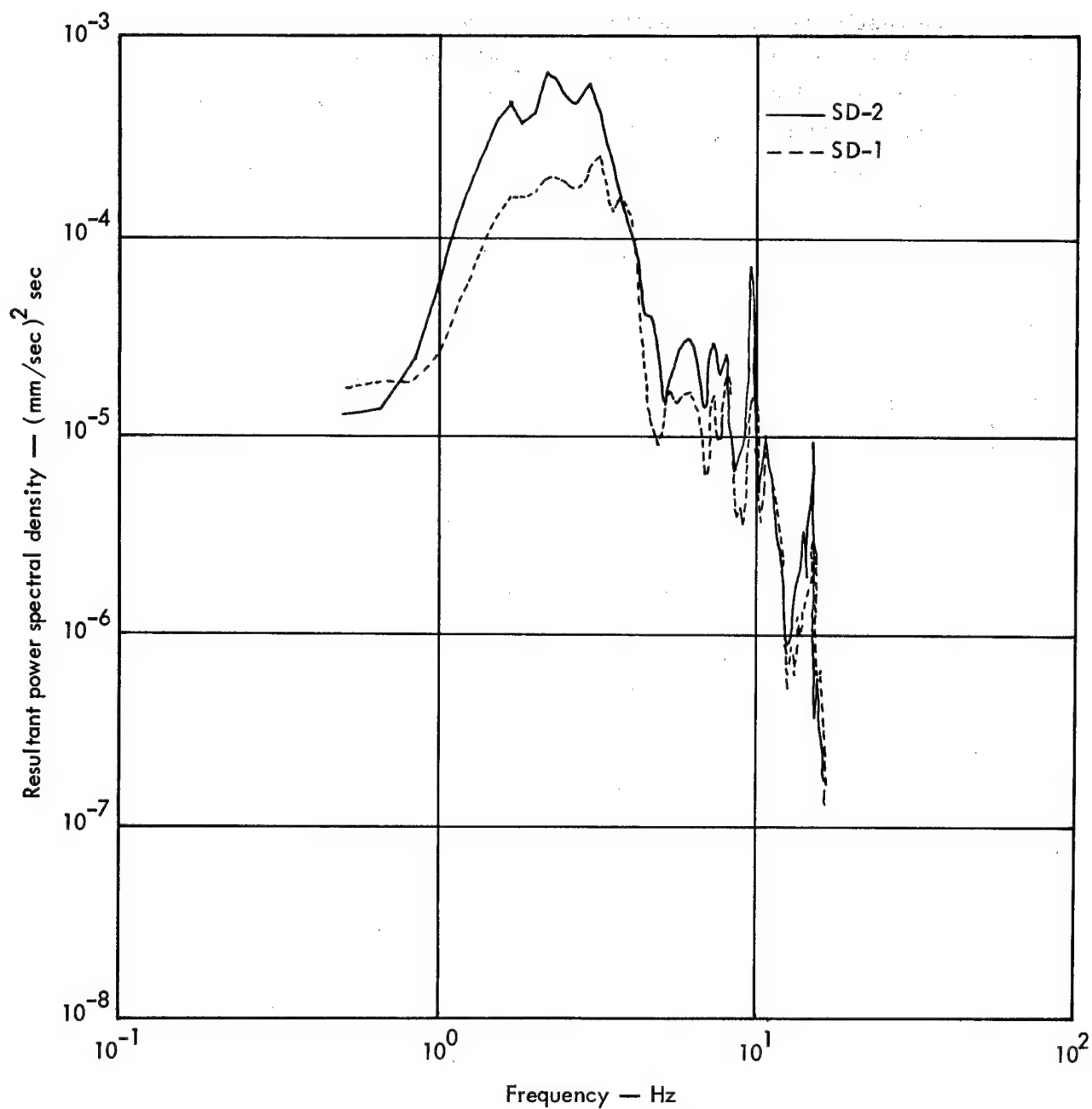


Fig. 34. Resultant power spectral densities at Station 6W for two source configurations.

In order to give the reader a feeling for the actual transducer signals, several are shown in Figs. 61 and 62. (The traces

shown have been redrawn for reproduction purposes from the originals and are not suitable for analysis.)

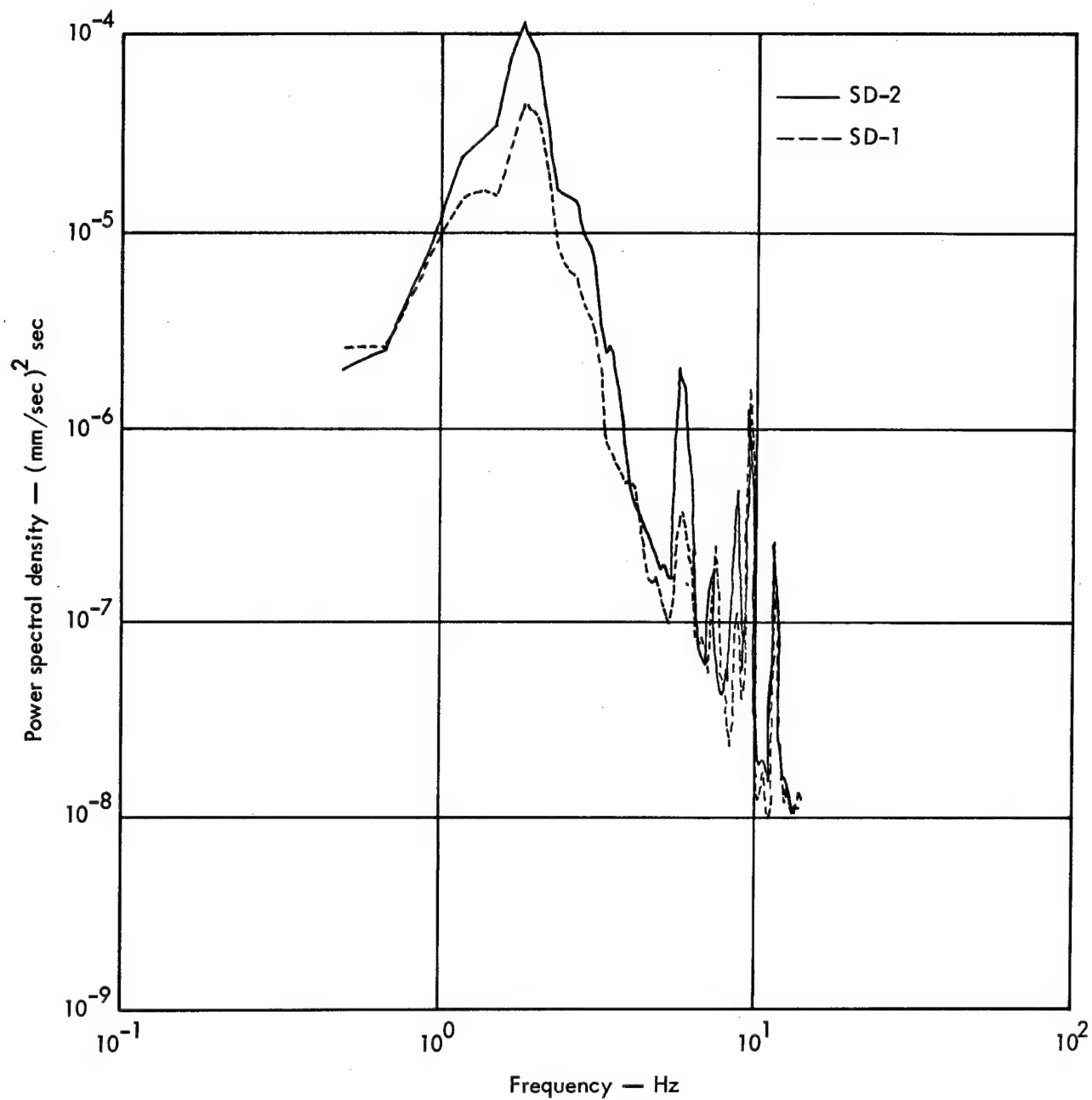


Fig. 35. Radial components at Station 2BN for two source configurations.

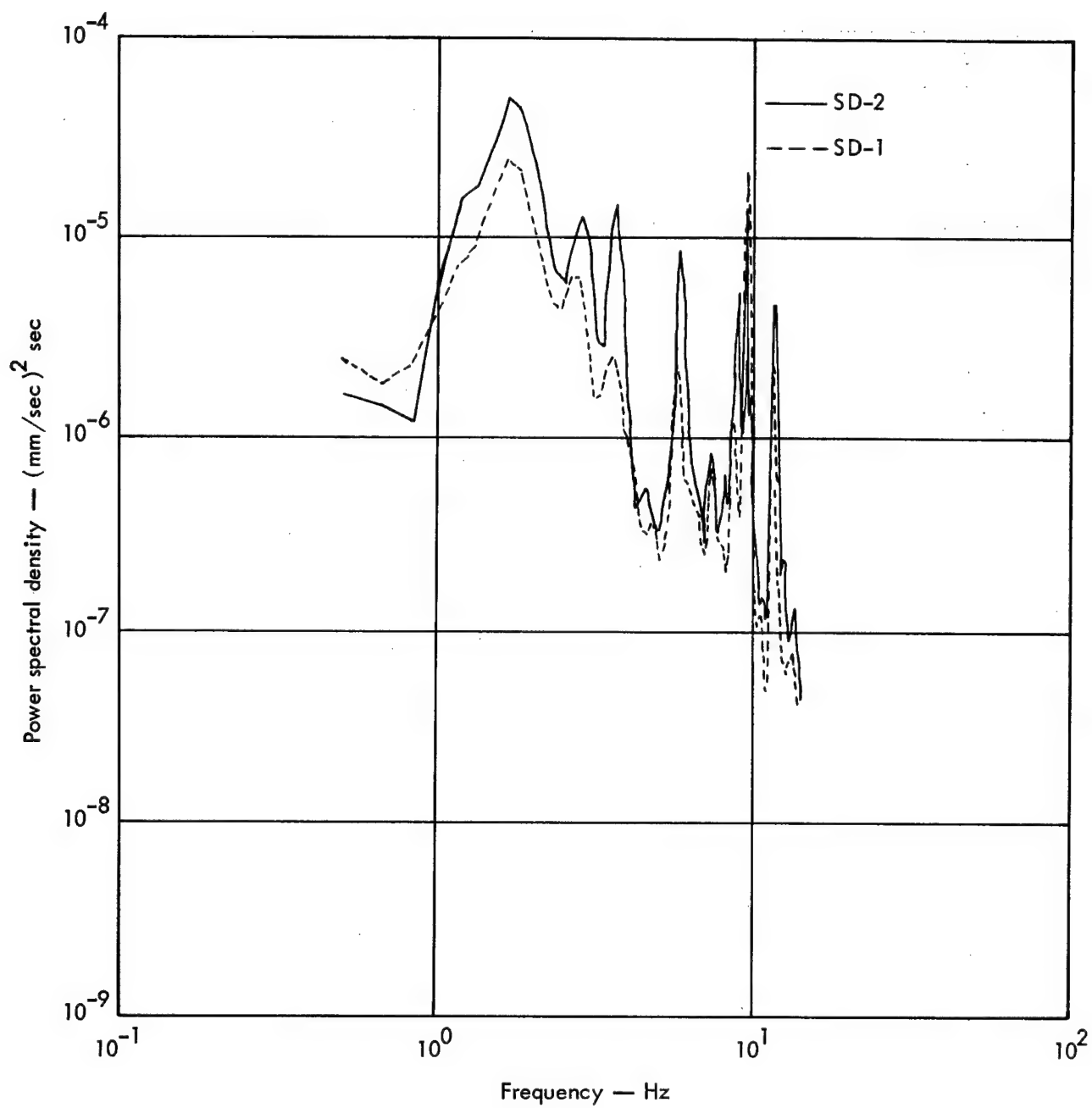


Fig. 36. Transverse components at Station 2BN for two source configurations.

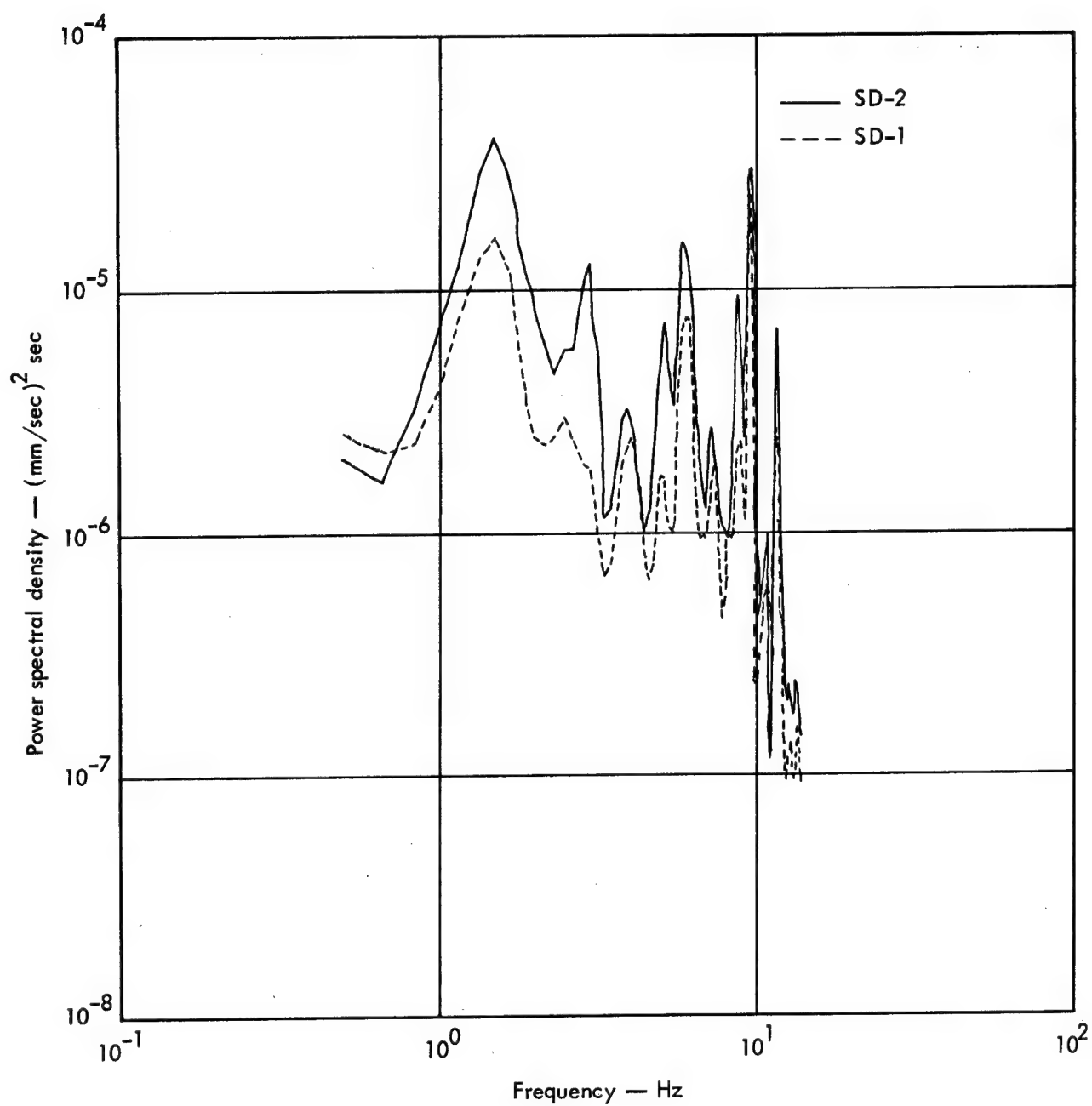


Fig. 37. Vertical components at Station 2BN for two source configurations.

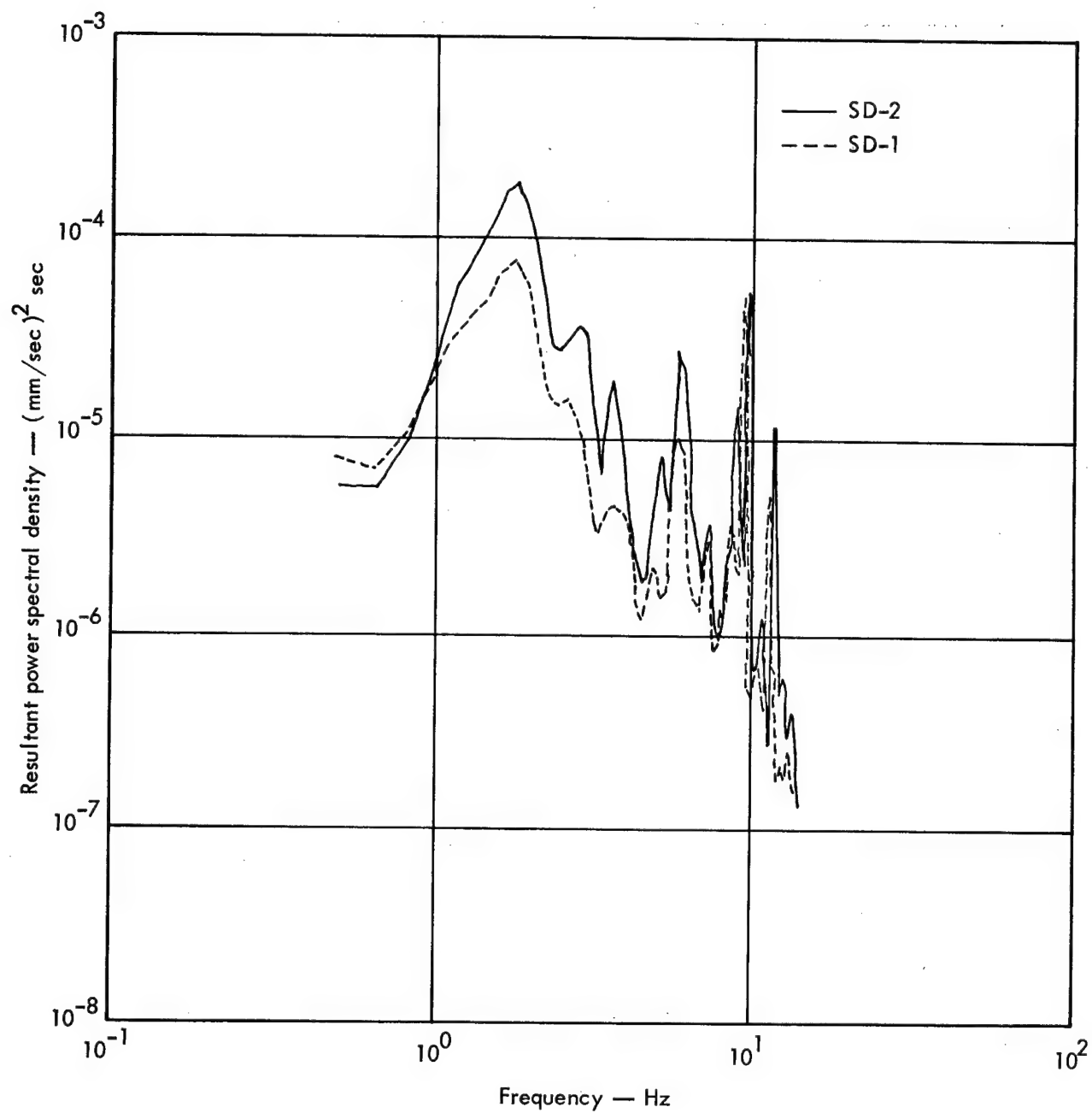


Fig. 38. Resultant power spectral densities at Station 2BN for two source configurations.

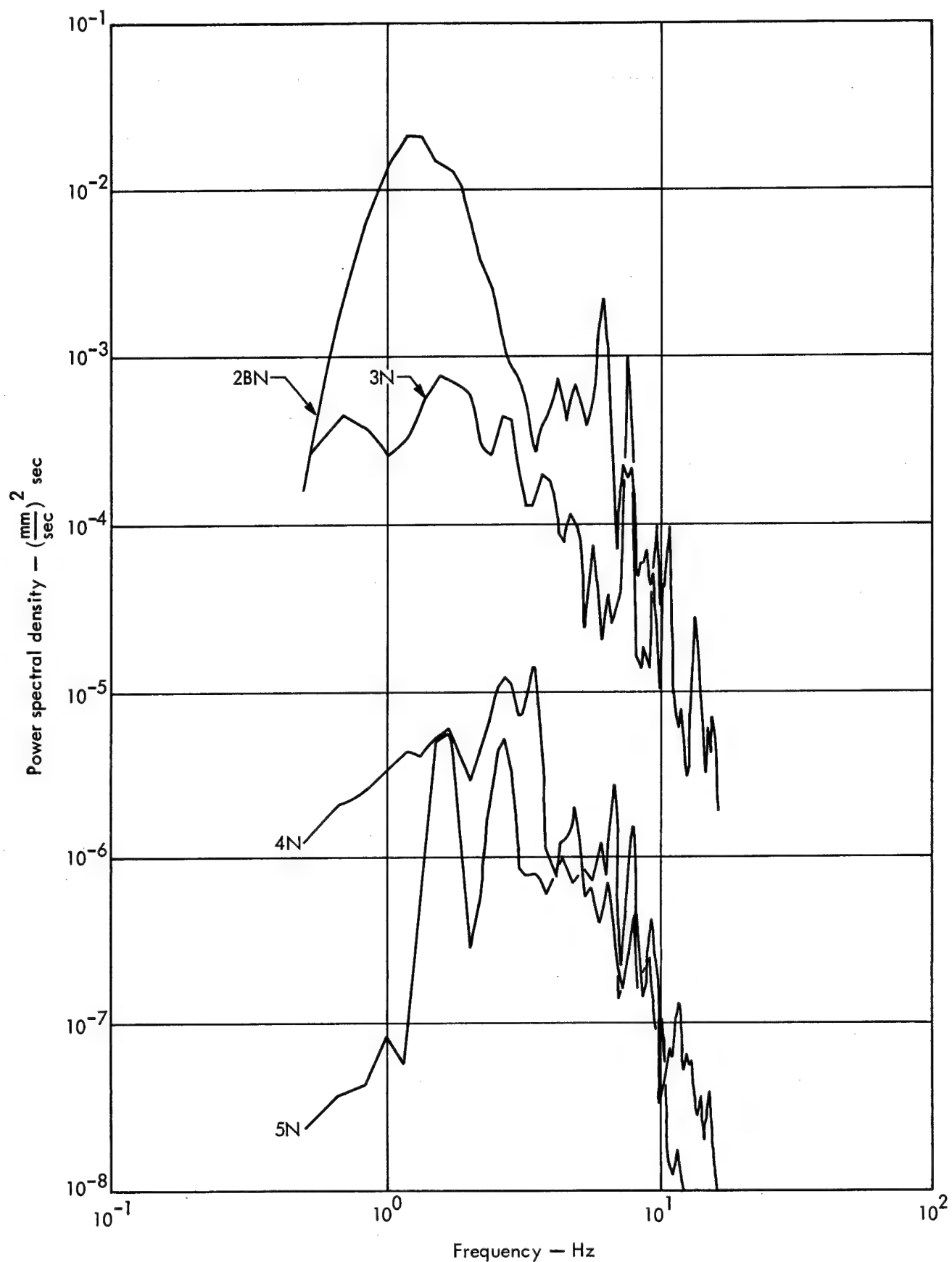


Fig. 39. Radial components for Pre-Gondola I Bravo Event at various distances.

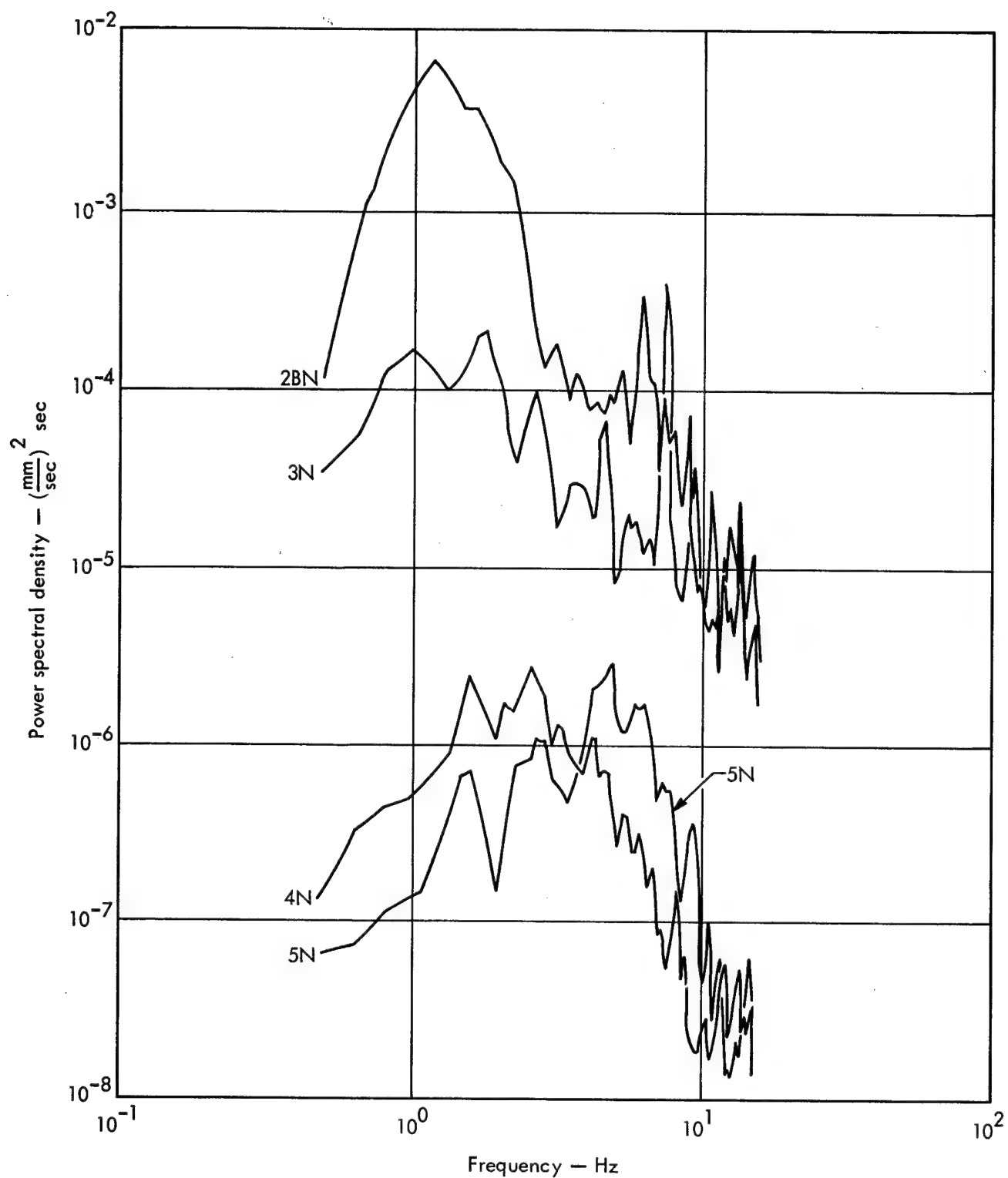


Fig. 40. Transverse components for Pre-Gondola I Bravo Event at various distances.

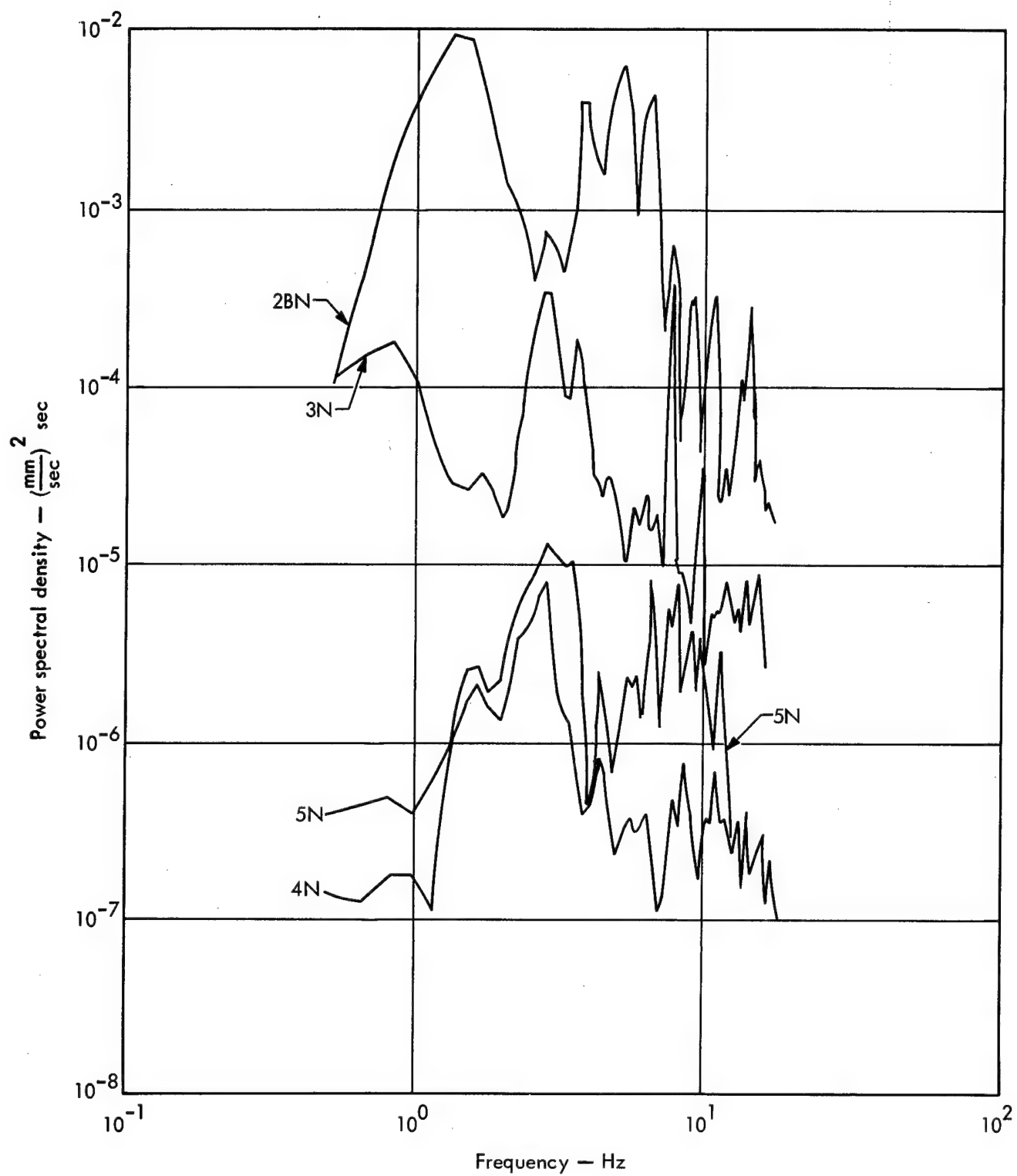


Fig. 41. Vertical components for Pre-Gondola I Bravo Event at various distances.

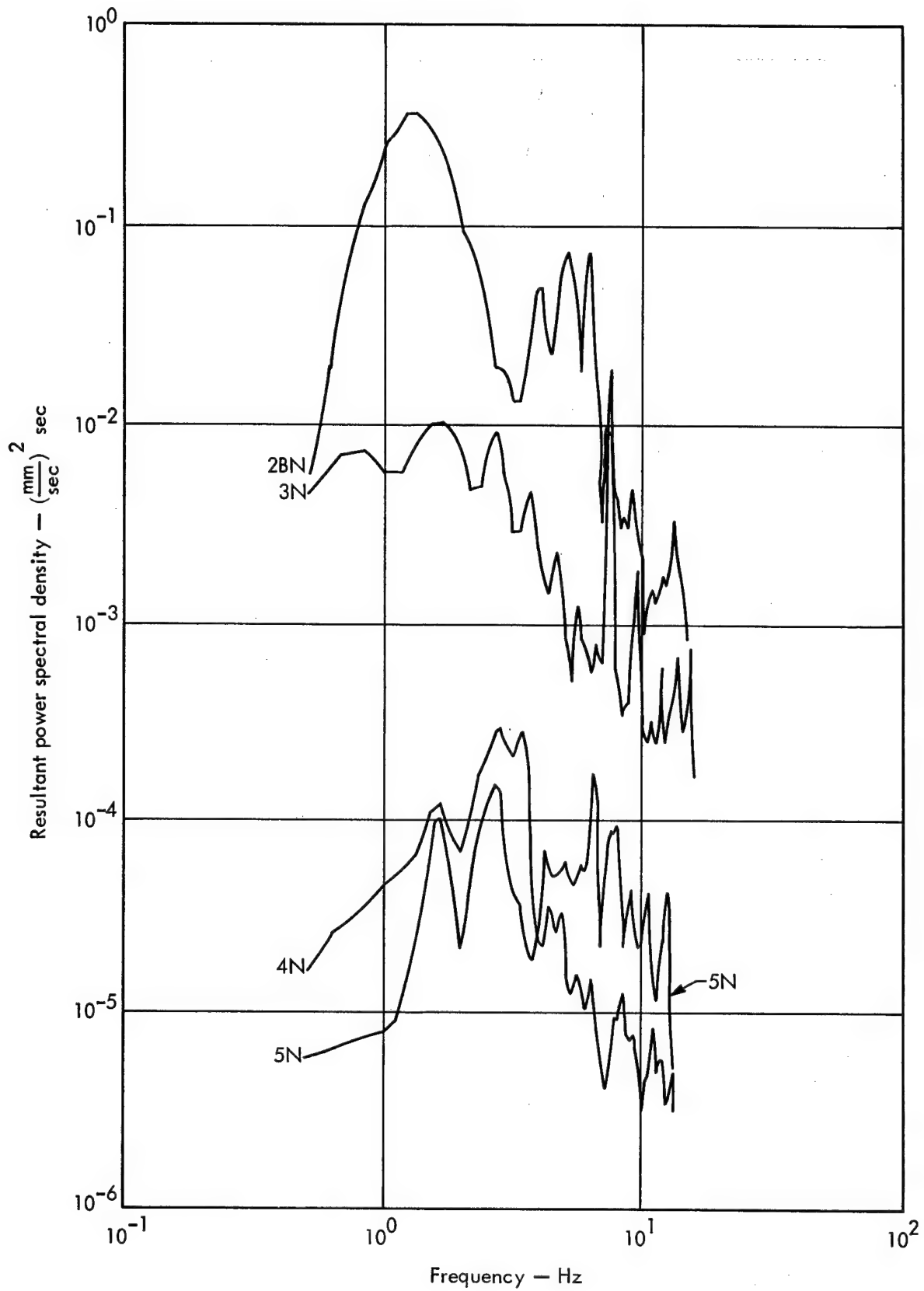


Fig. 42. Resultant power spectral densities for Pre-Gondola I Bravo Event at various distances.

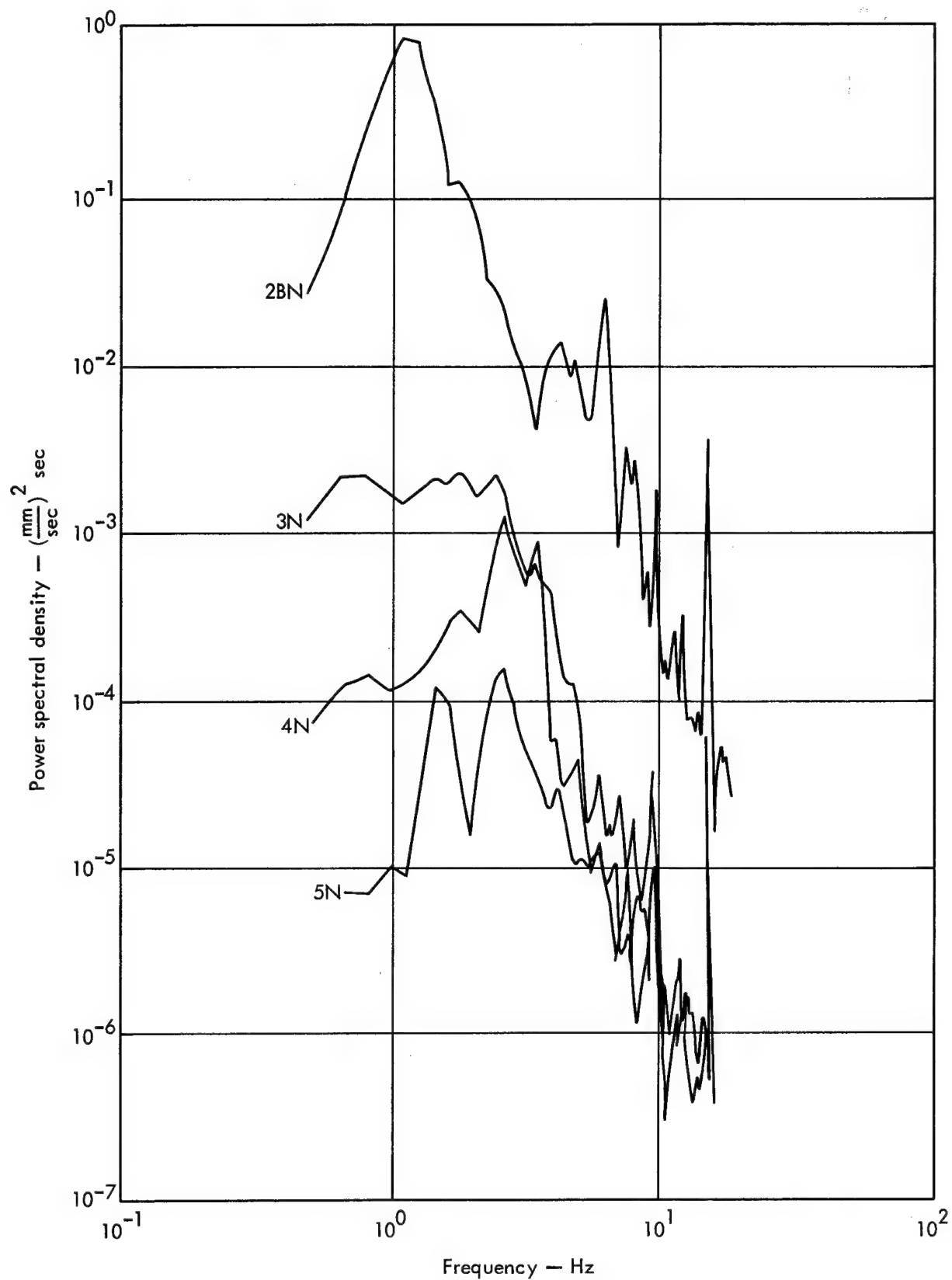


Fig. 43. Radial components for Pre-Gondola II 140-ton row charge at various distances.

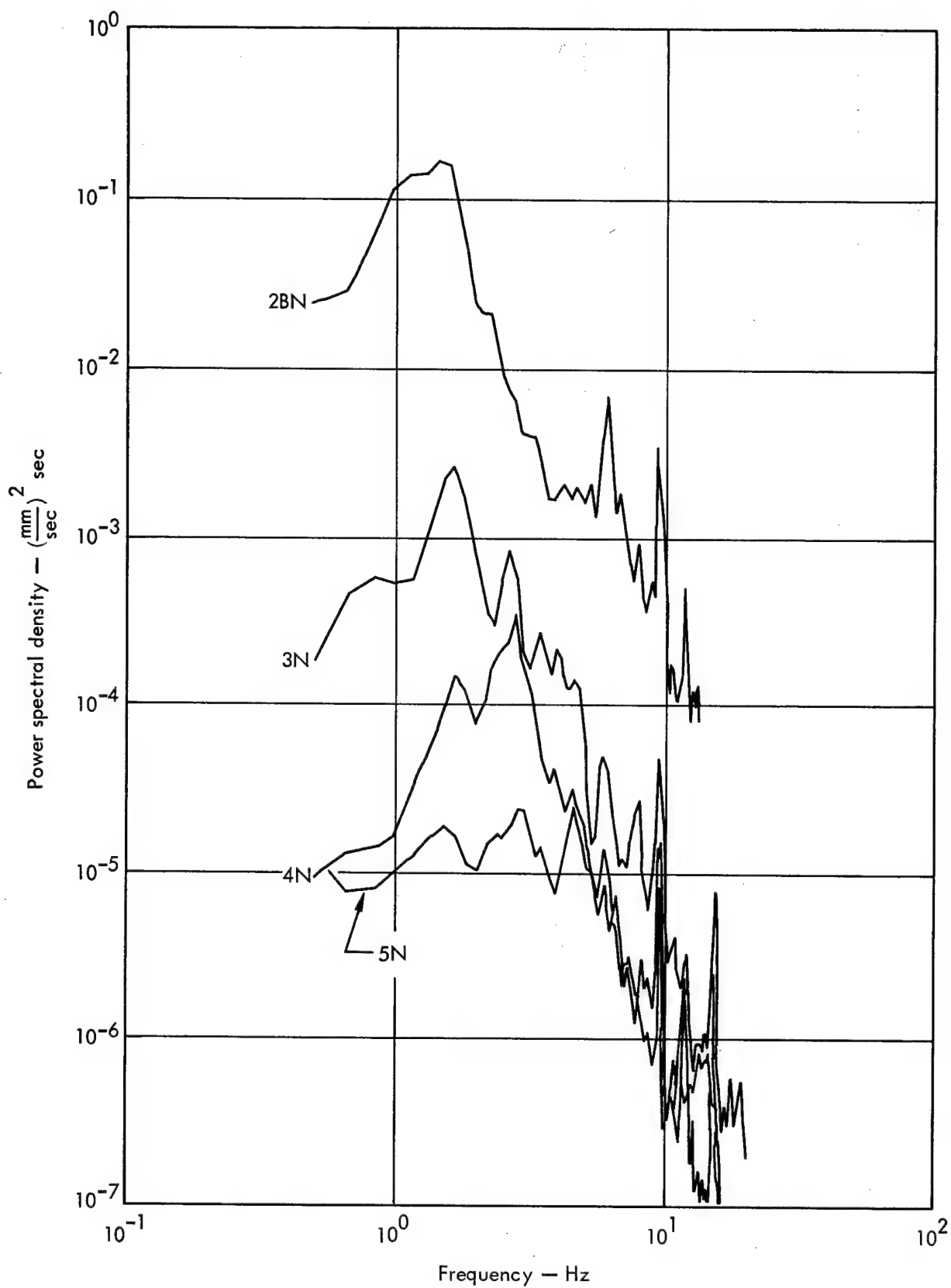


Fig. 44. Transverse components for Pre-Gondola II 140-ton row charge at various distances.

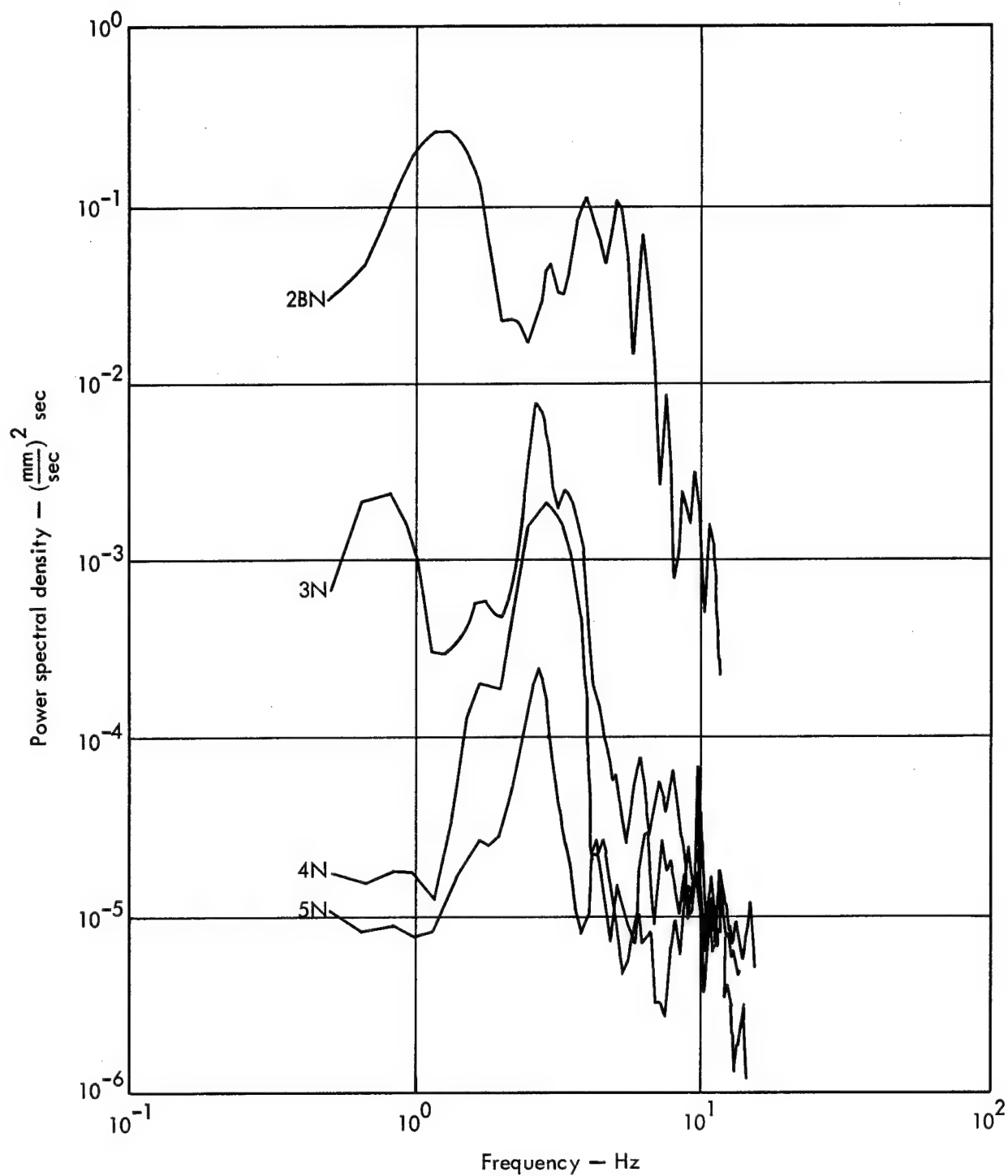


Fig. 45. Vertical components for Pre-Gondola II 140-ton row charge at various distances.

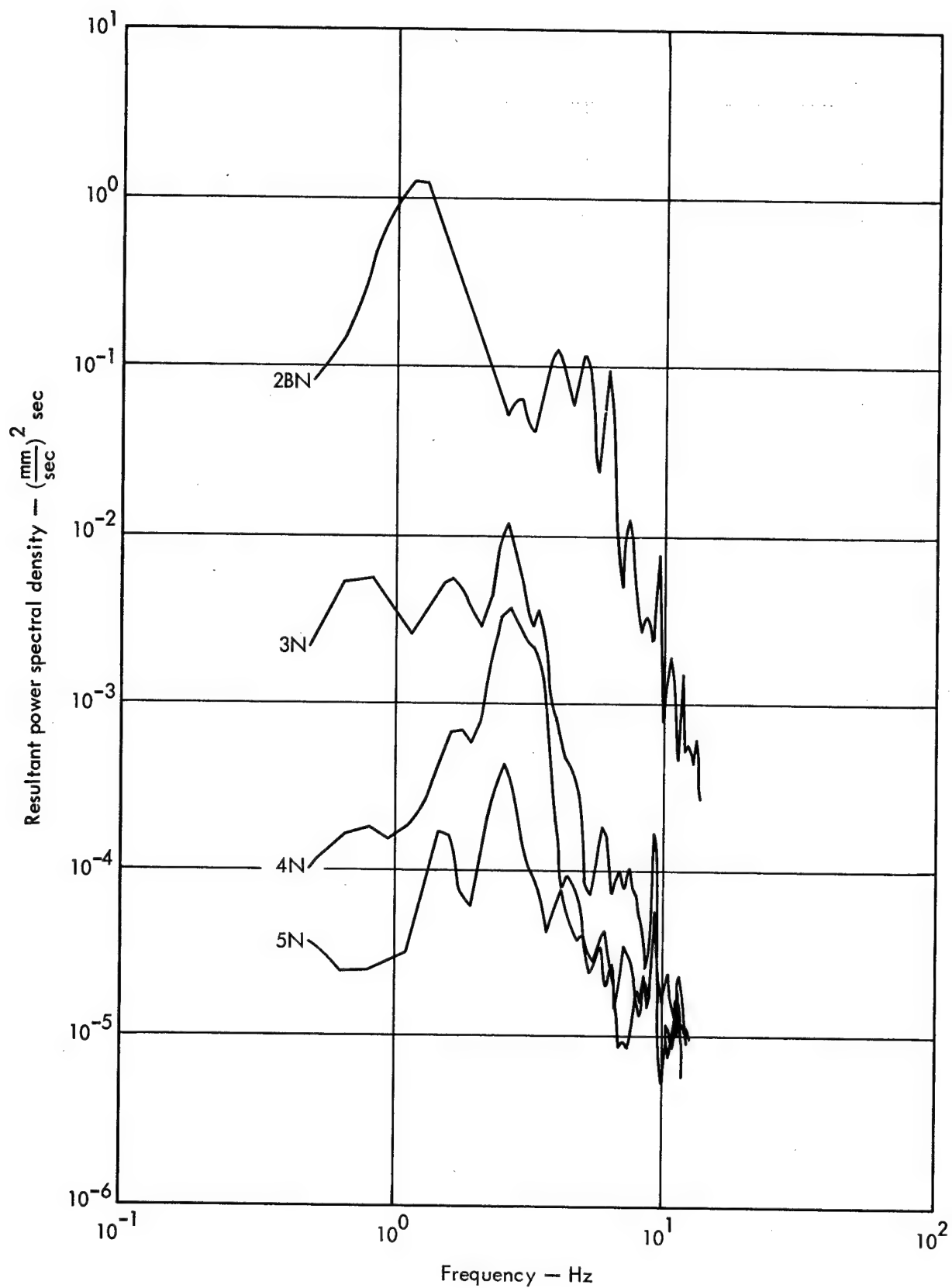


Fig. 46. Resultant power spectral densities for Pre-Gondola II 140-ton row charge at various distances.

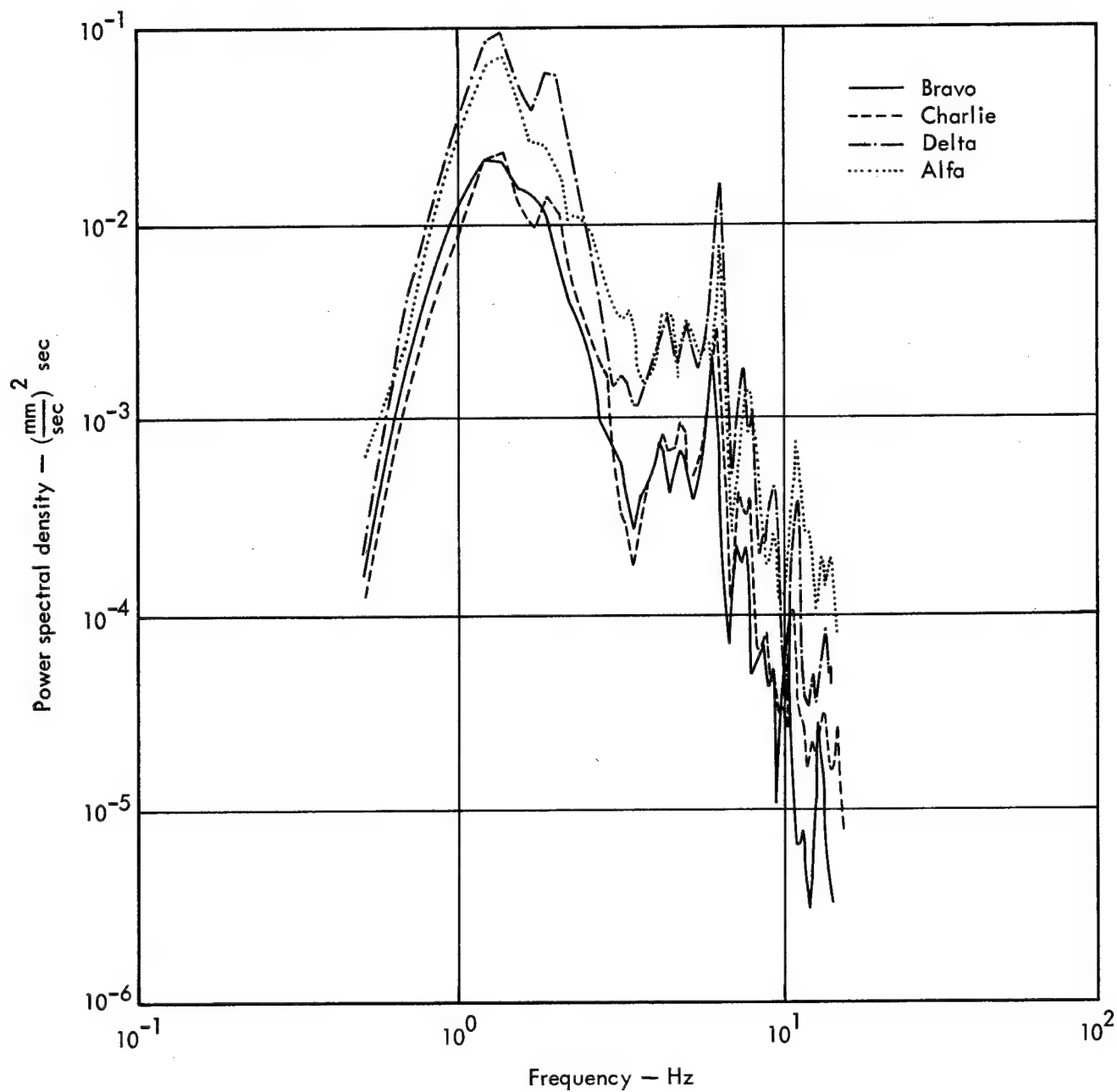


Fig. 47. Radial components at Station 2BN for four 20-ton events at different depths of burst.

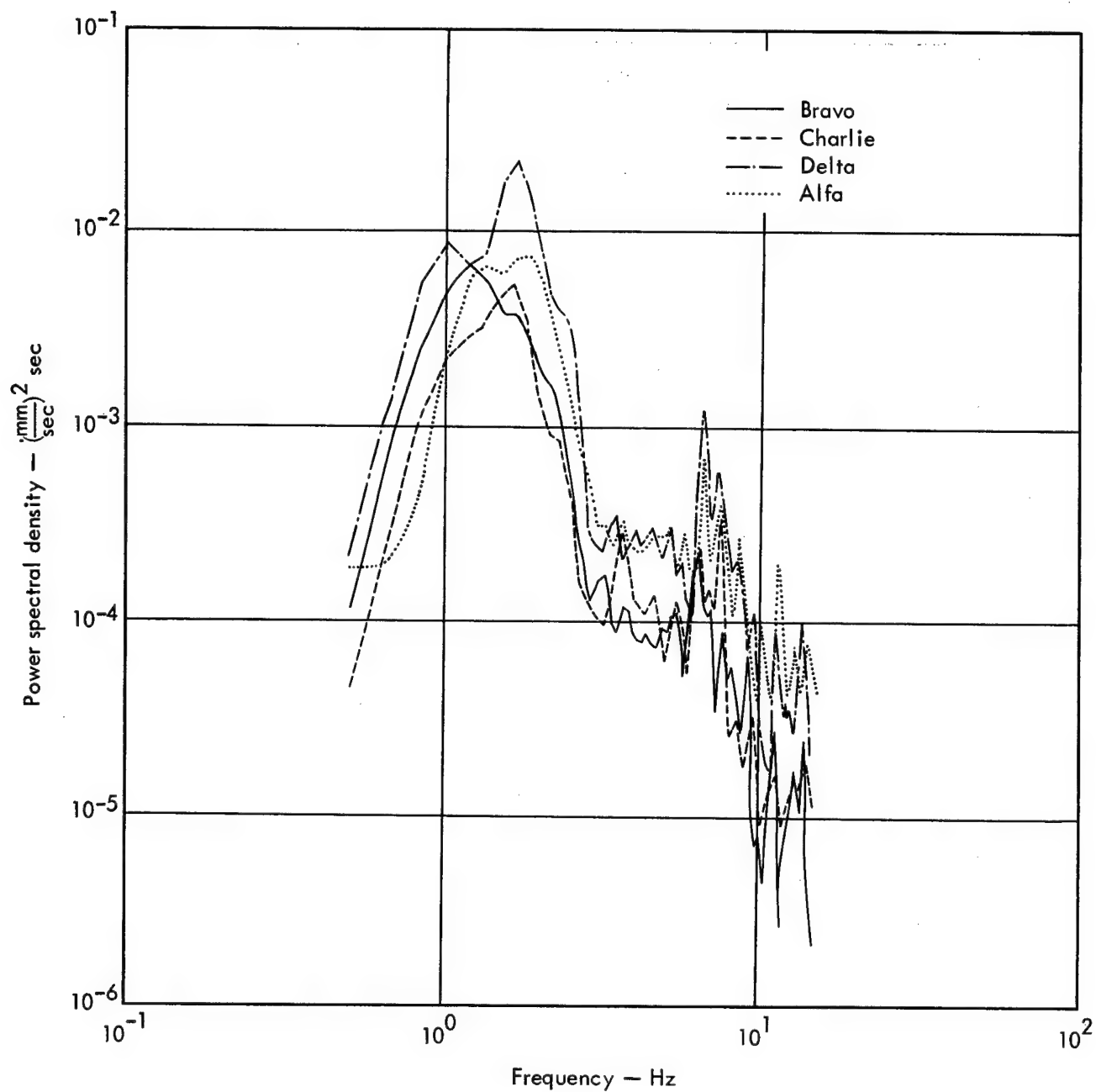


Fig. 48. Transverse components at Station 2BN for four 20-ton events at different depths of burst.

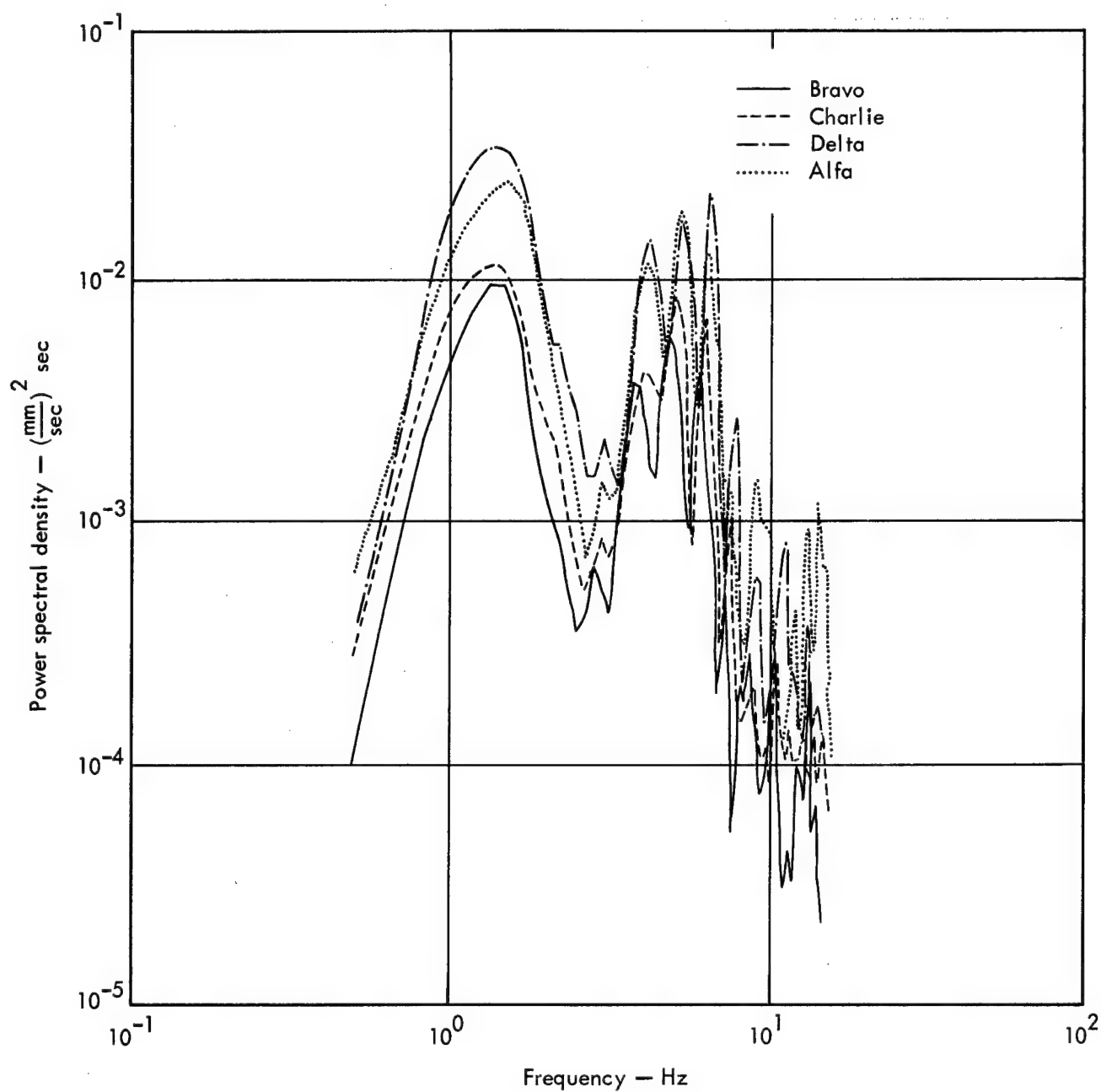


Fig. 49. Vertical components at Station 2BN for four 20-ton events at different depths of burst.

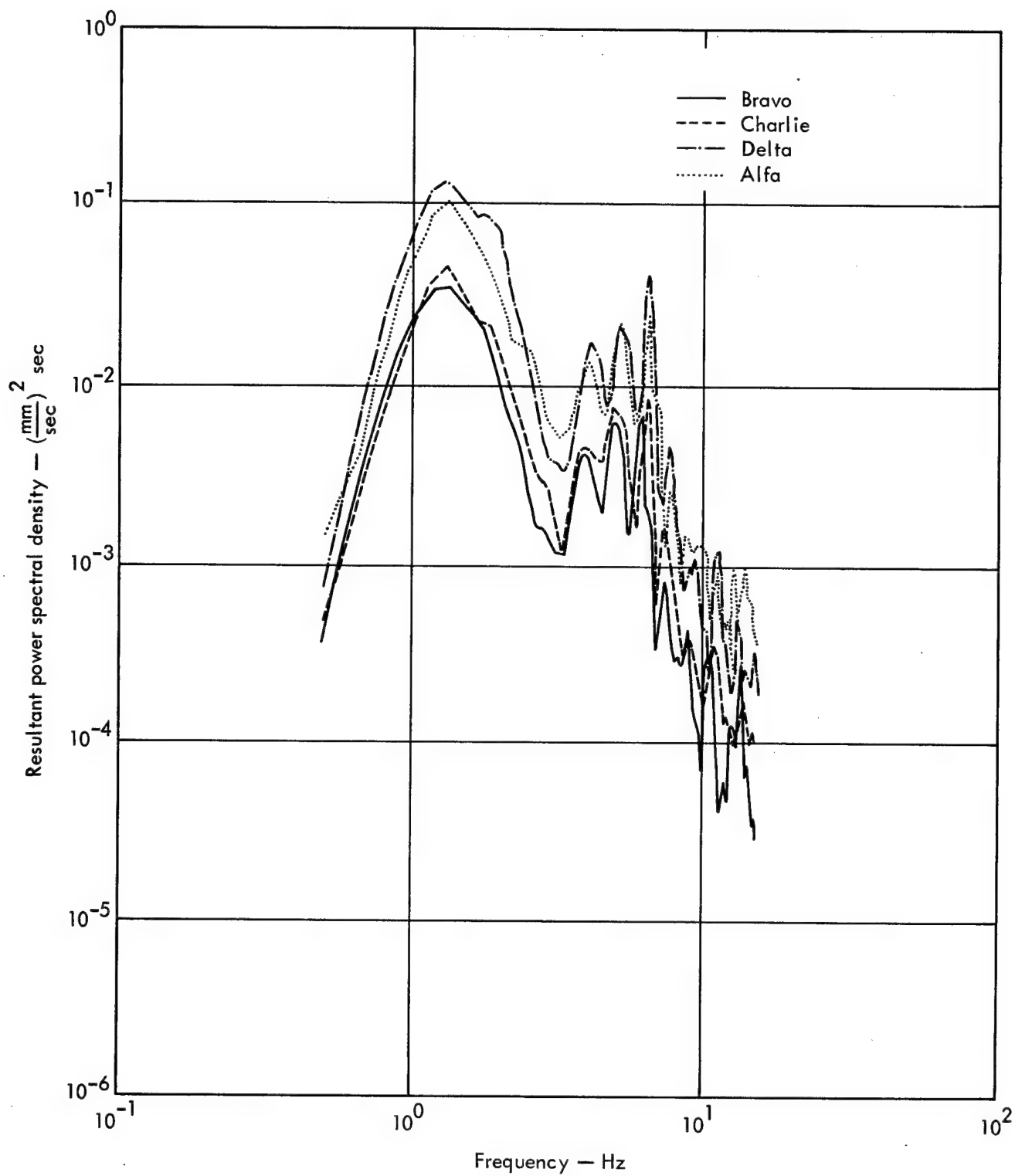


Fig. 50. Resultant power spectral densities at Station 2BN for four 20-ton events at different depths of burst.

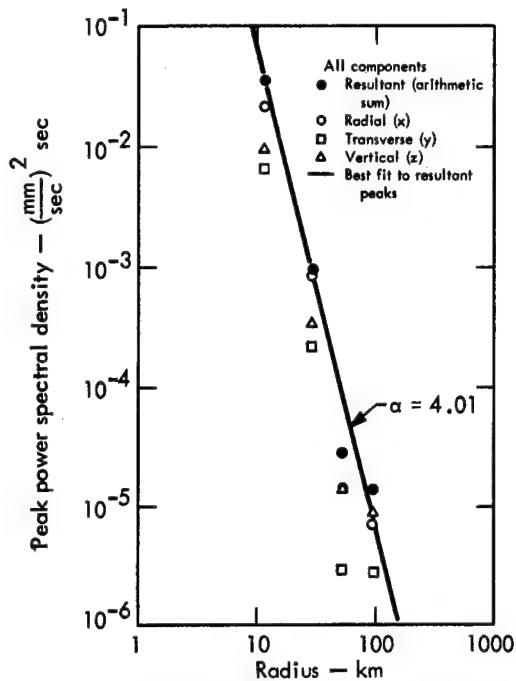


Fig. 51. Peak power spectral densities plotted against radius for Pre-Gondola I Bravo Event (α comes from the equation: $PSD_p(R) = KR^{-\alpha}$).

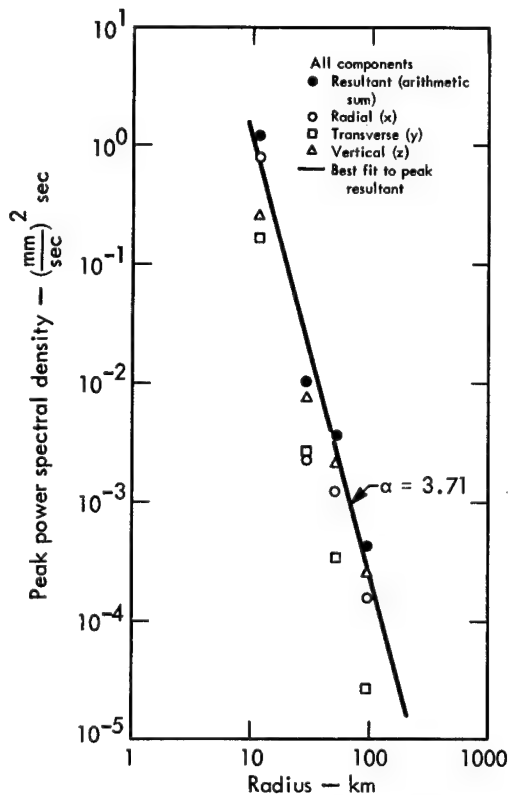


Fig. 52. Peak power spectral densities plotted against radius for Pre-Gondola II 140-ton row charge (α comes from the equation: $PSD_p(R) = KR^{-\alpha}$).

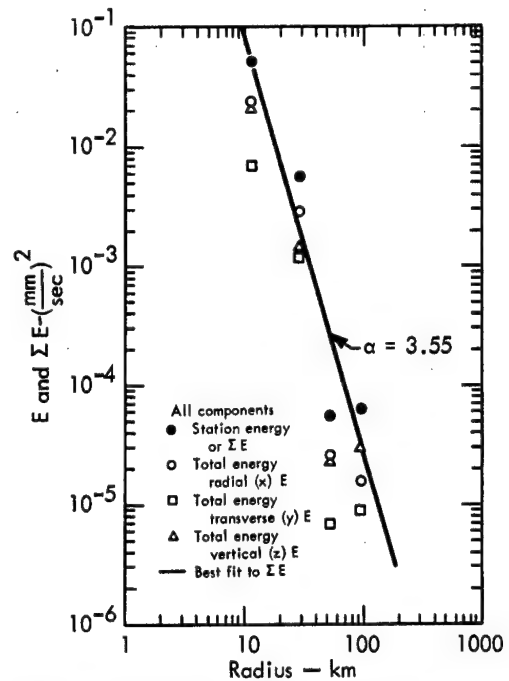


Fig. 53. Energy in seismic signal for components and total energy as a function of radius for Pre-Gondola I Bravo Event (α comes from the equation: $\sum E(R) = KR^{-\alpha}$).

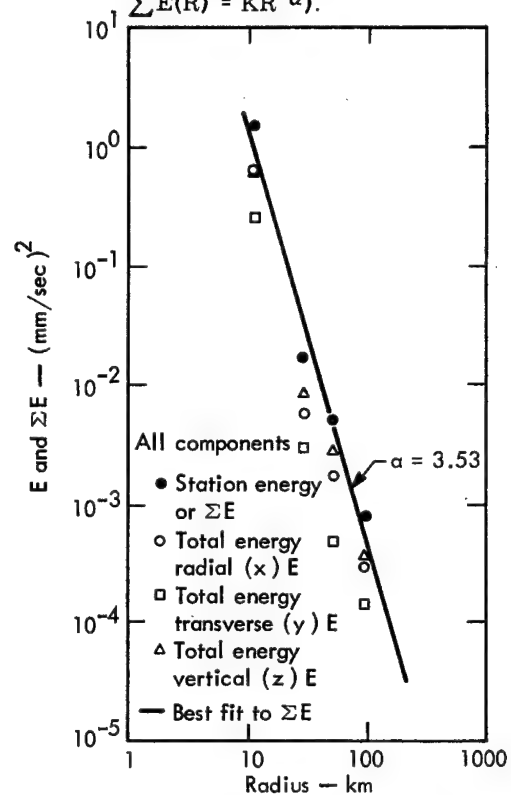


Fig. 54. Energy in seismic signal for components and total energy as a function of radius for Pre-Gondola II 140-ton row charge (α comes from the equation: $\sum E(R) = KR^{-\alpha}$).

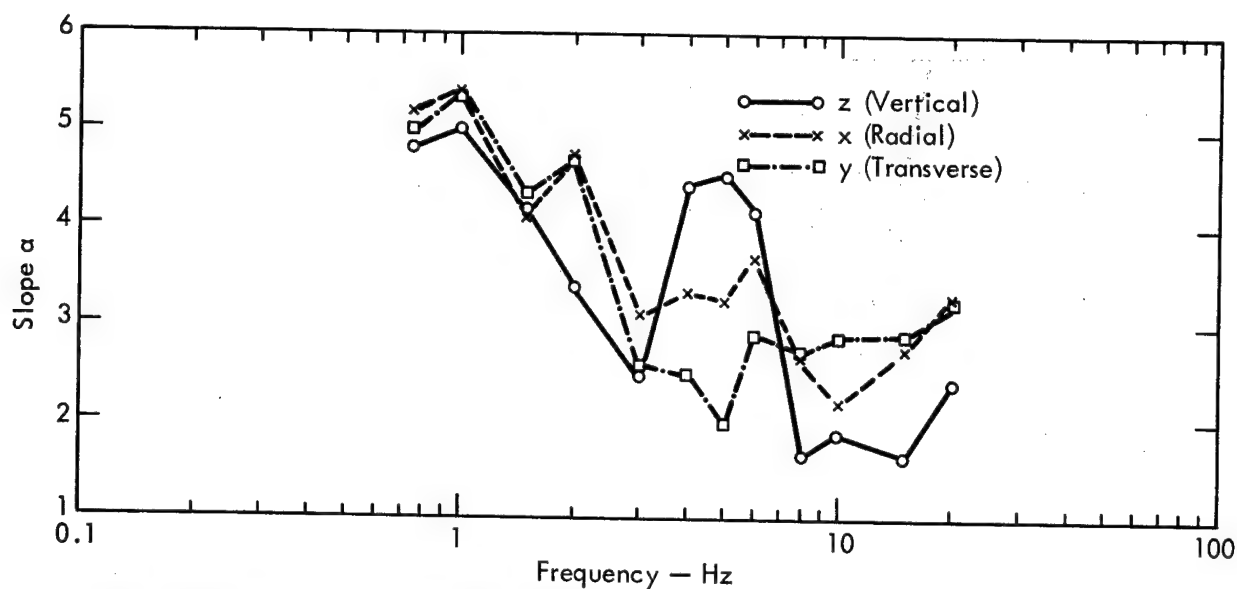


Fig. 55. Slope of power spectral density attenuation as a function of frequency for Pre-Gondola I Bravo Event (i. e., slope α comes from the equation: $\text{PSD}(R, f) = K_f R^{-\alpha(f)}$).

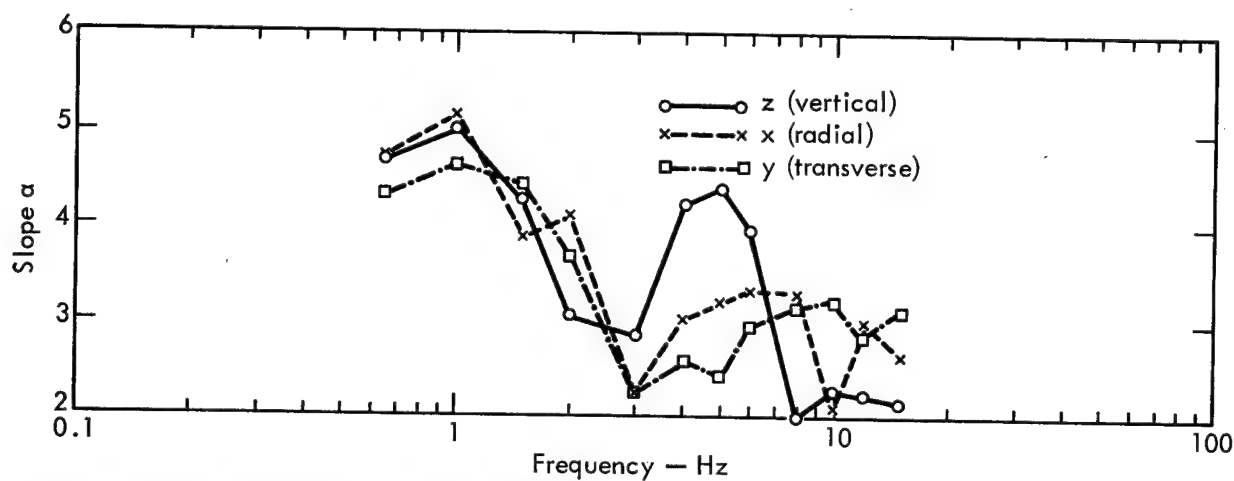


Fig. 56. Slope of power spectral density attenuation as a function of frequency for Pre-Gondola II 140-ton row charge (i. e., slope α comes from the equation: $\text{PSD}(R, f) = K_f R^{-\alpha(f)}$).

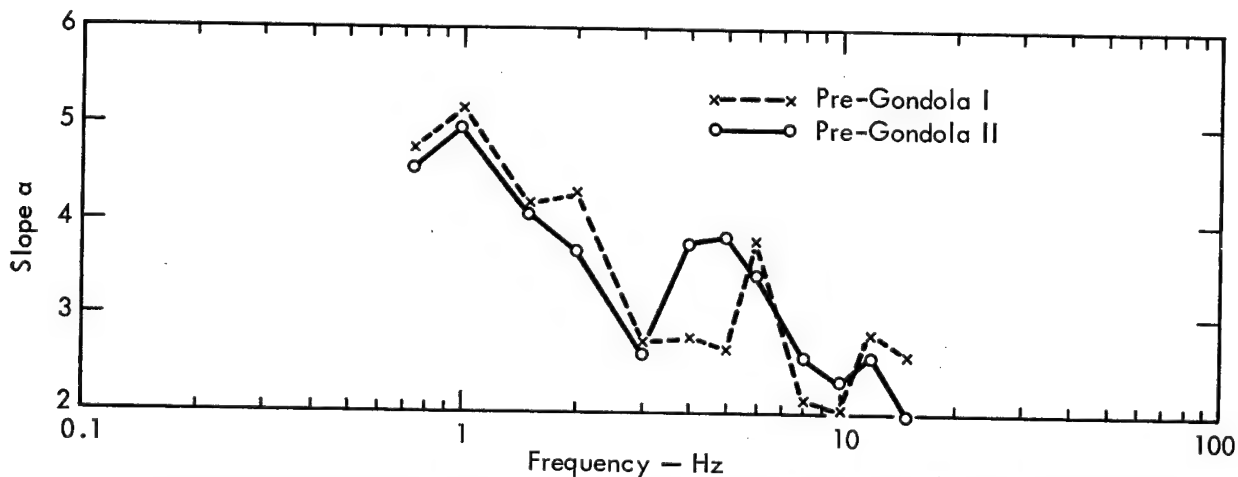


Fig. 57. Comparison of attenuation for resultant power spectral densities plotted as a function of frequency for Pre-Gondola I and II.

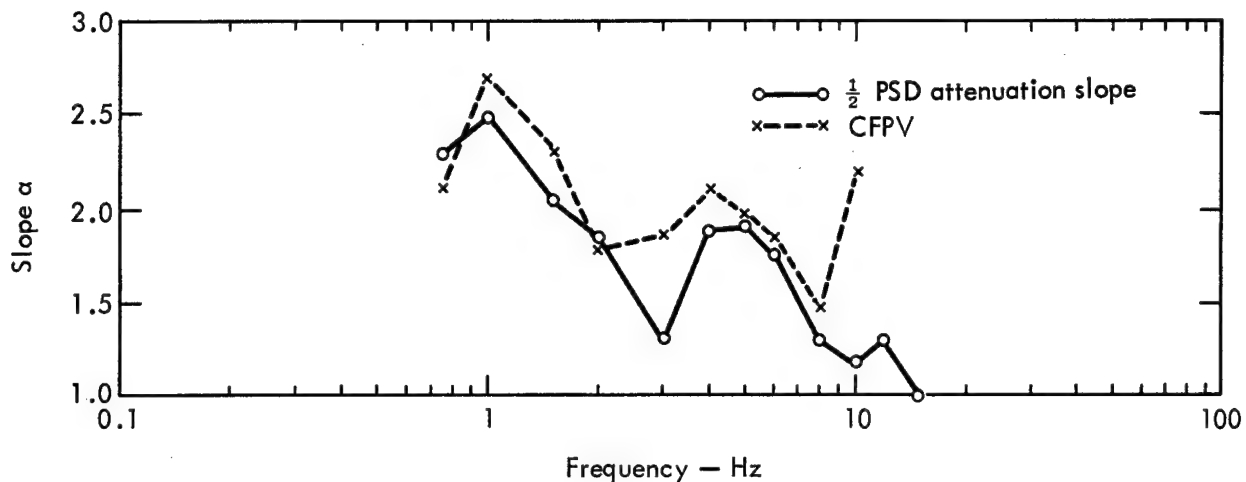


Fig. 58. Comparison of slopes of attenuation of comb filter peak velocities to one-half of slopes of attenuation of power spectral density resultant for Pre-Gondola II 140-ton row charge as a function of frequency.

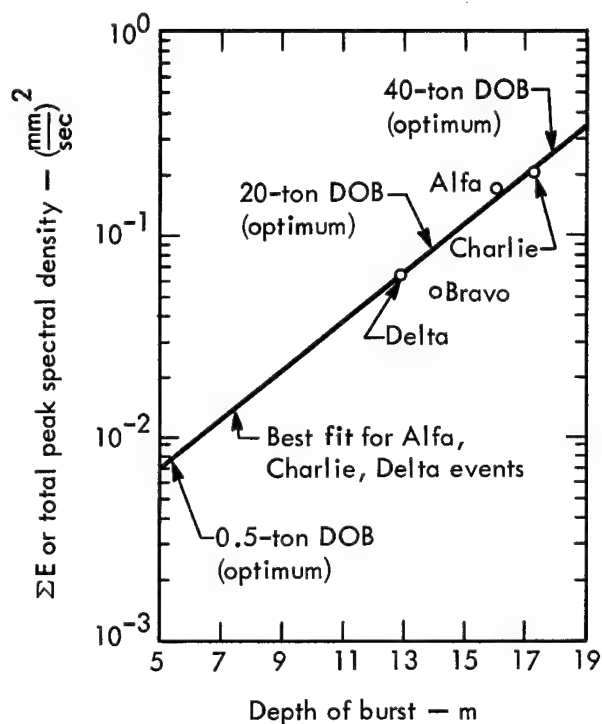


Fig. 59. Total station energy (ΣE) at Station 2BN (Pre-Gondola I) showing transmitted energy dependence upon actual depth of burst (Bravo datum is neglected—see text); curve is extrapolated to DOB's for 40-ton and 0.5-ton events to obtain comparisons for Pre-Gondola II.

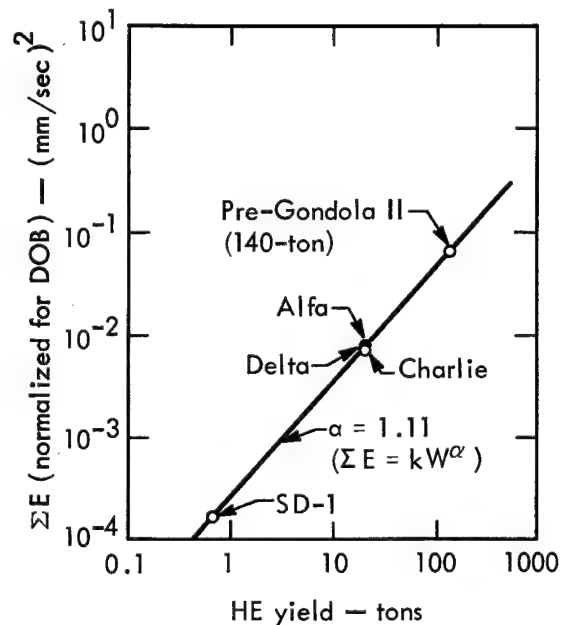


Fig. 60. Total station energy (ΣE) vs yield after depth of burst effect has been removed.

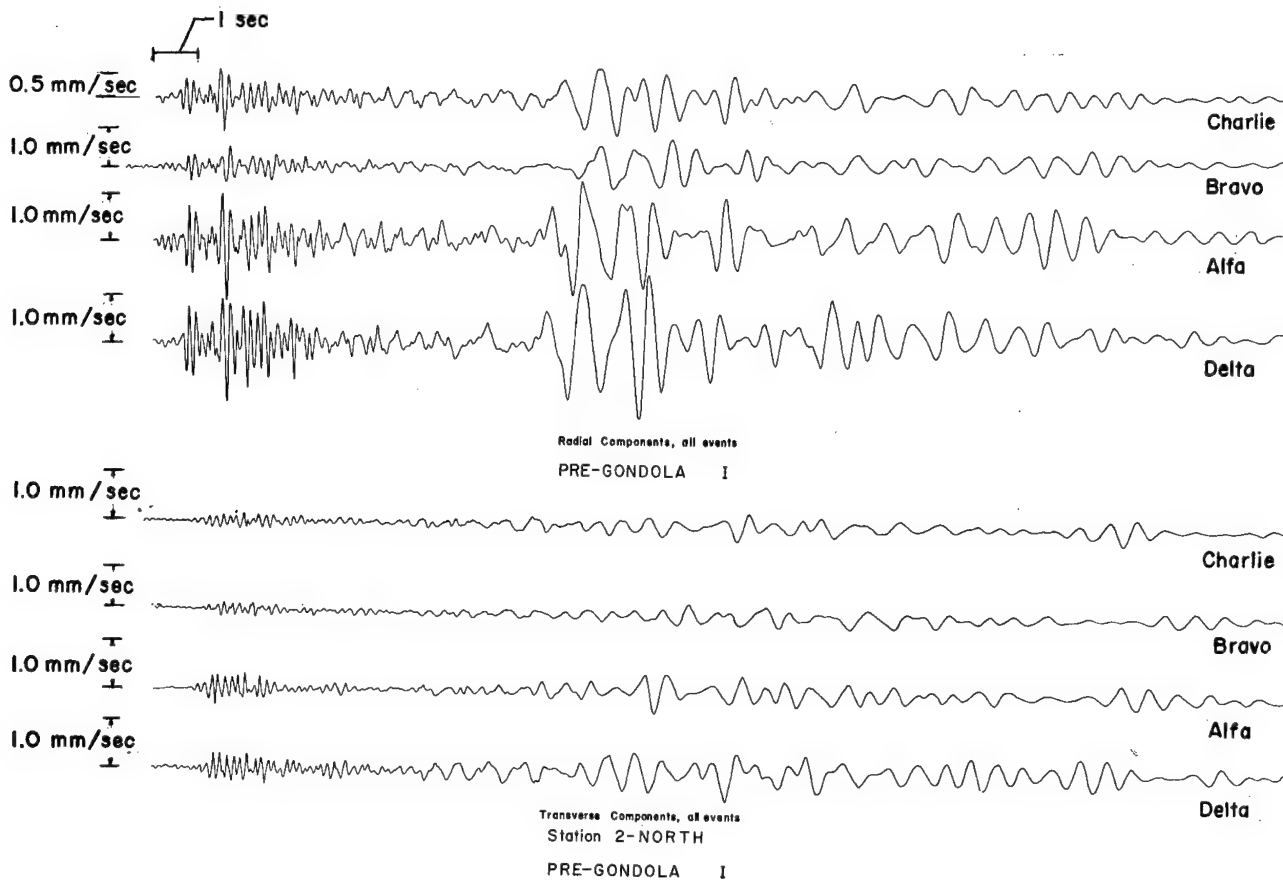


Fig. 61a. Radial and transverse components at Station 2BN for Pre-Gondola I (all events).

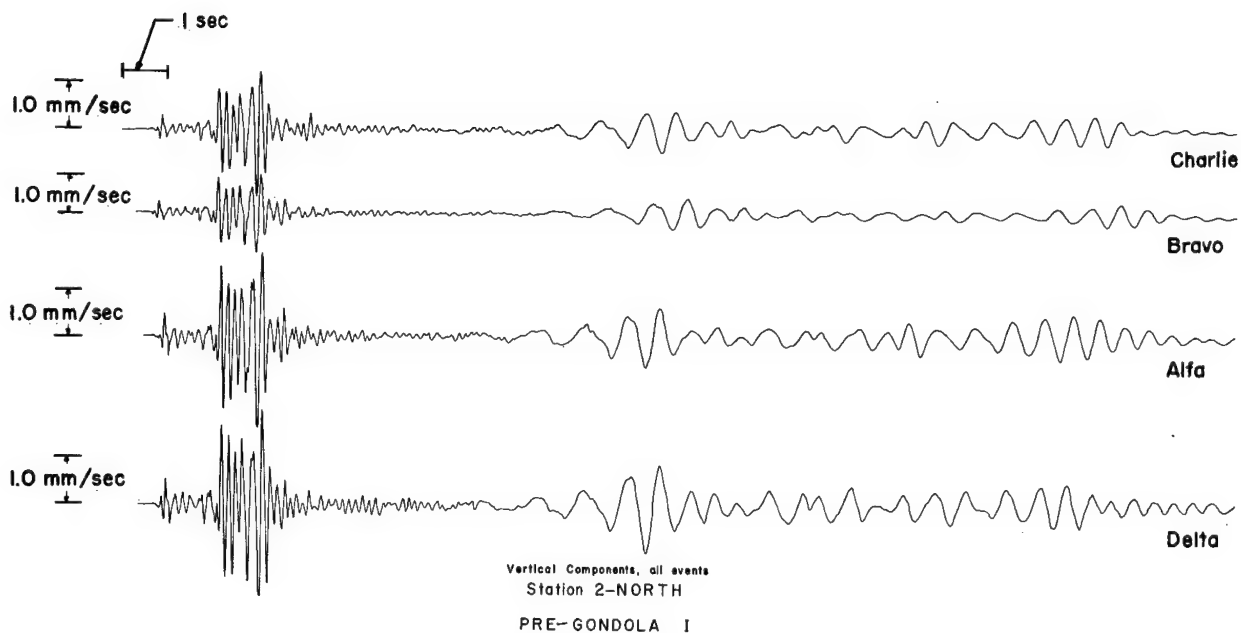


Fig. 61b. Vertical component at Station 2BN for Pre-Gondola I (all events).

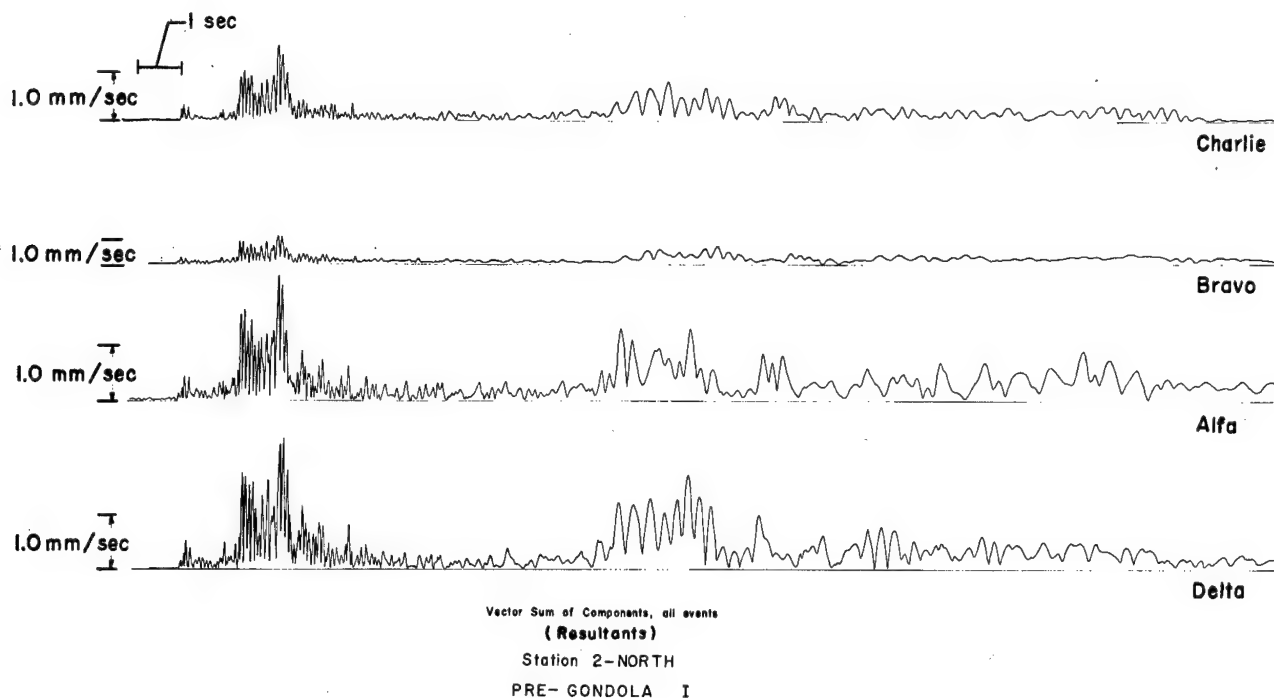


Fig. 61c. Resultant velocity at Station 2BN for Pre-Gondola I (all events).

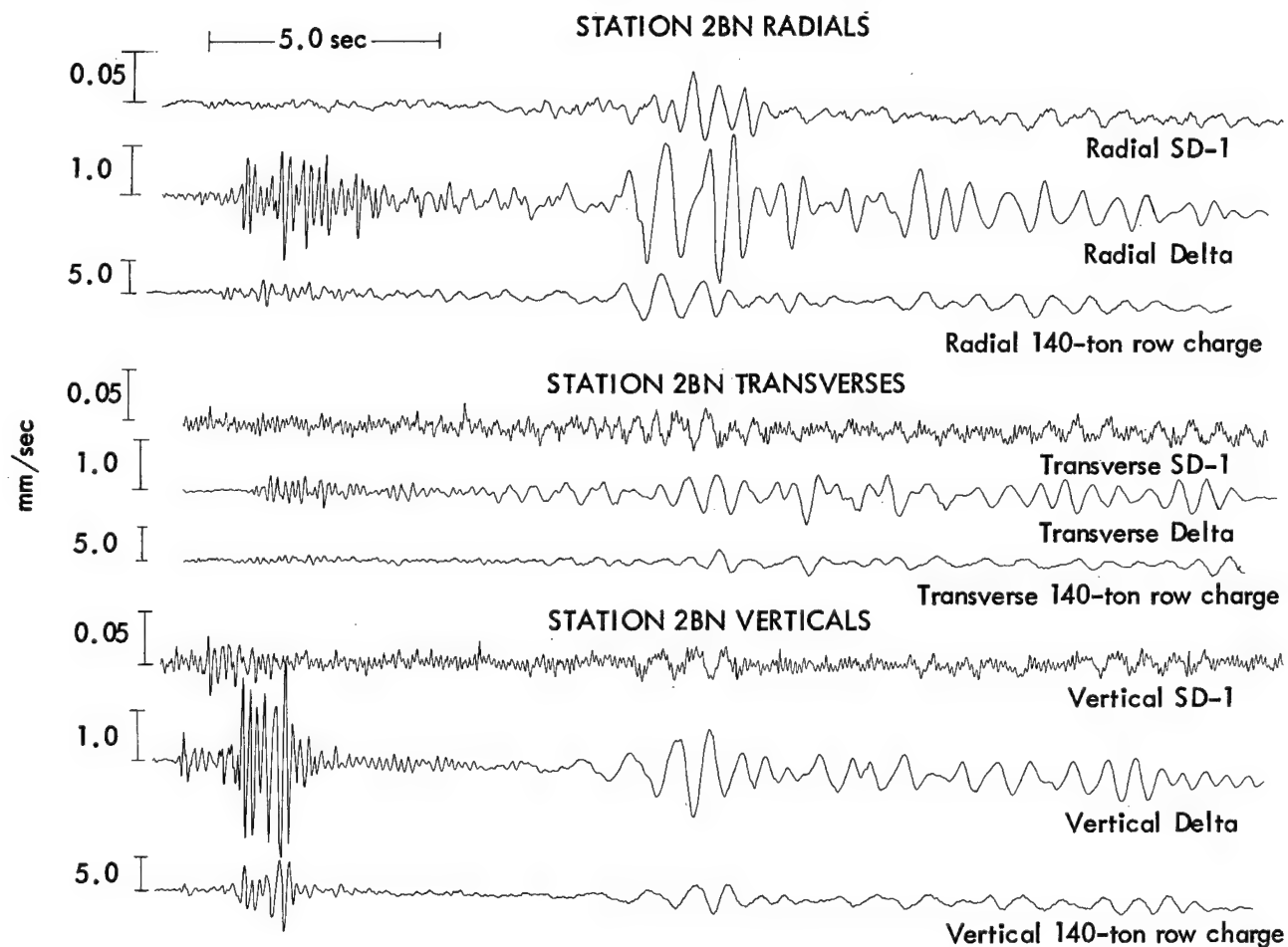


Fig. 62. Signals recorded at Station 2BN for three different yields (0.5- and 20-ton single bursts and 140-ton row charge).

Analysis of Results, Discussion, and Interpretation

TIME HISTORY VARIANCES

A comparison of the signals for the Pre-Gondola series of events revealed two primary facts. The first is that variations in yield and depth of burst had little effect upon the general appearance of the signals at any given station except for amplitude. Figures 61 and 62 illustrate this fact very well. These figures would indicate that the source varied only in amplitude and very little else.

The second fact revealed is that in spite of efforts to instrument sites of similar properties, the signals at the various stations bear little resemblance to each other. For instance, the large early vertical arrivals at Station 2BN regularly consisted of 7 or 8 cycles of motion of nearly constant amplitude for all events. At Station 5N for both the Bravo Event and the 140-ton row charge this portion of the record for the vertical motion contained only a single cycle of very high amplitude motion and very little other motion. Thus when peak velocity is plotted as a function of distance (Figs. 7 and 8), Station 5N consistently appears high. When a least squares fit to the data is made, the scatter is large and considerable uncertainty exists about projecting the results to new sites.

There is no way to tell whether the differences in signals between stations is due to transmission path or local effects, or a combination of these.

Because of the unusual motion at Station 5N during the Bravo Event, when PNE-1105¹ was written, Station 5N

figures were neglected and a high slope for attenuation was given. When the motion at Station 5N from the 140-ton row charge showed the same peculiarities, it became obvious that new slopes should be calculated for Bravo. This new value for α (Bravo) of 1.54 is considerably lower than that reported in PNE-1105 ($\alpha = 2.45$) but shows good agreement with the α for the 140-ton row charge calculated for the same stations. The attenuation constants of 1.54 and 1.64 are lower than expected,⁶ but Station 5N strongly biases these numbers.

As was stated, the depth of burst seemed to affect little except amplitude (Fig. 61). A variation in yield for these studies also meant a variation in depth of burst, thus an even larger difference is noted in the signals shown in Fig. 62. Part of the difference in general appearance is due to the high level of background seismic noise in the records from the SD-1 Event which interferes with the comparison. Little more than these qualitative statements can be made concerning these records but they are significant statements nevertheless.

Although they are not shown, the records from the SD-2 Event are almost identical to those of SD-1 except in amplitude. The somewhat surprising result is that amplitudes were consistently higher for SD-2, which was decoupled, than for the coupled shot SD-1. Upon reflection this is not so surprising. It is a well known fact that an explosively driven metal plate will generate a higher pressure in a target if it is allowed to be driven across a gap of inches magnitude

as opposed to being initially in contact with the target.⁷ The reason is that the gap allows for the potential energy of the explosive to be changed into the kinetic energy of the metal plate, resulting in a higher initial pressure in the target. Since the explosive in the SD-2 shot was contained in a 1/8-in. thick wall aluminum sphere, 4-3/4 in. smaller in radius than the cavity, it is possible that the resulting higher pressure at the cavity wall could cause a higher percentage of the explosive energy to be coupled into the elastic seismic signal.

VELOCITY IN THE FREQUENCY DOMAIN

General Behavior

The CFPV method does only a partial job of spectral analysis in that it does a frequency separation of the signal but fails to give any information concerning the total energy contained in each frequency. The reason is that a single cycle of motion gives the same value of amplitude as a continuous sine wave, whereas the two signals are vastly different in terms of power, etc. Because of the greatly varying time history for different stations, the CFPV method is unable to clarify to any great degree the relationships between transmitted signal and received signal.

A review of Figs. 9 through 25 illustrates the important capabilities of the CFPV method. A signal usually contains several significant frequencies of motion related to the specific modes of wave propagation with characteristic wave periods. The CFPV gives an indication of what these frequencies are, though only one or two peaks are discernible in most of the figures.

In general the vertical shows two peaks; one at 2 or 3 Hz due to late arrivals, and the other at about 8 Hz due to early arrivals. The radial and transverse do not always show two main frequencies. The higher frequency is usually smaller in amplitude than the lower and is sometimes missing entirely. The maximum motion is usually found in either the low-frequency, late arrivals of the radial wave or in the high-frequency, early arrivals of the vertical motion.

The correlation of the CFPV's at the different stations for the same event is better than for the time history signals themselves. The general shape of the CFPV's is fairly consistent except at Station 5N where that single cycle pulse greatly distorts the CFPV of the vertical. This record from Station 5N illustrates one of the main failings of the CFPV method.

Range Dependence

As was done for the peak value alone, a plot of the peak value at each frequency or CFPV vs distance (taken from Figs. 19 through 25) may be made and an α be calculated from a best fit to the points. The equation is

$$\text{CFPV}(f) = V_p(f) = K_f R^{-\alpha(f)}.$$

(These plots are not shown.) When these α 's are plotted against frequency, the curve in Fig. 26 is produced. Theory and investigations have shown that α should be a function that varies fairly smoothly and that increases with frequency.⁸ It is therefore surprising to note that the curves in Fig. 26 are far from smooth and, even

more surprising, they decrease with an increase in frequency. This does not appear to be any failing of the CFPV method since the same result is obtained by the PSD method (see Range Dependence in Power Spectral Density section). It therefore appears to be inherent in the signal. A possibility is that background noise, both seismic and electronic, may be contributing factors but no conclusion can be drawn until further studies are made.

Source Configuration

Good consistency is shown in the CFPV method when the same station measures events at the same SGZ. This is shown by comparing the CFPV's of the various components for Stations 2BN and 6W on the SD-1 and SD-2 Events. These are shown in Figs. 11, 12, 13, 16, 17, and 18.

There appears to be no significant change in frequency peaks as the source coupling is changed. But the unusual result of higher amplitudes at nearly all frequencies for the decoupled event is again apparent. It is obvious that this effect of increase in seismic signal amplitude occurs only for small distances between inner and outer spheres at the source. Eventually, as this void space is increased beyond some value, the effect will be to lower the pressure on the cavity wall thus decreasing the seismic signal.

Yield Dependence

Only two points are available to compare CFPV's at different yields. The point for SD-1 (0.5-ton) is shown in Fig. 9, and the point for the 140-ton row charge is shown in Fig. 19. There appears to be a general shift in the curves to lower frequencies at the higher yields, though the shift is small,

being only about 30 to 50% for a factor of 280 in yield. Such a small shift may be related to the actual depth of burst, and one should be careful in trying to extend this to the completely contained case.

The amplitudes are different by approximately $\times 100$. This is only a crude estimate of the ratio since an accurate one is not possible due to the shapes of the curves. A scaling factor of $\beta = 0.8$ is given by the equation:

$$A_1/A_0 = (W_0/W_1)^\beta$$

$$100 = (280)^\beta$$

$$\text{or } A = kW^{0.8} = kW^\beta$$

where W is the yield.

POWER SPECTRAL DENSITY AND SEISMIC ENERGY

General Characteristics

The PSD's for all stations analyzed are much more consistent than CFPV's. This is to be expected since the PSD method is an averaging process, and the problems exemplified by Station 5N are overcome.

Since it is an averaging technique, the length of record analyzed becomes important because a single pulse will give a smaller PSD(f) for a longer length of record analyzed. The total energy, however, is independent of the length of record. For this reason the two following steps were taken to insure consistency. The total length (in seconds) of record was made the same when possible so that visual comparisons of PSD's would be objectively correct. This length of record was 32 sec for all stations and all events except for Stations 2BN and 6W on the

SD-1 and SD-2 Events. The latter records were only 24 sec long. Numerical calculations were made, whenever a choice was possible, on integrated PSD or total energy in a signal or station (E or $\sum E$).

The radial and transverse components consistently show a pronounced peak at 1 to 3 Hz with smaller peaks at 6 to 8 Hz. The vertical also shows a most pronounced peak at 1 to 3 Hz and several strong peaks at 6 to 10 Hz.

Source Configuration

A comparison of the PSD's for the SD-1 and SD-2 Events, component by component at Stations 2BN and 6W, are shown in Figs. 31 through 38. These show a remarkable repeatability for the two events with only the amplitudes varying. This variance is again an increase of signal strength for a small decoupling factor. Enough has already been said of this phenomenon and the results of the PSD method are consistent with other analysis techniques.

Depth of Burst

Figures 47 through 50 show the PSD's component by component at Station 2BN for the four 20-ton events. These events differed only in depth of burst. Again these figures show little variation except in amplitude, a fact not unexpected since the actual time histories are so similar. When the PSD is integrated over frequency to obtain E , and E is summed over components to give the $\sum E$ received at the recording site, a dependence upon actual depth of burst becomes apparent. This is shown graphically in Fig. 59.

The datum point for the Bravo Event shown in Fig. 59 was low, and reasons

for this were discussed at length in PNE-1105.¹ Suffice it to say here that there is good evidence that Bravo vented early and coupled less efficiently than it should have. For this reason it has been neglected in the following analysis.

The straight line in Fig. 59 is a least squares fit to the three points, Delta, Alfa, and Charlie. It is doubtful that the real curve is a straight line, but three points do not give enough clues to warrant any other choice. As a first approximation then, the linear fit to a semilog plot is made. For obvious reasons this curve must flatten out at very deep depths and thus should not be extended to containment cases.

It is the contention of the author that this dependence of total station seismic energy ($\sum E$) on depth of burst is a result of the difference in time for the expanding cavity to communicate with the atmosphere. This contact with the atmosphere causes a sudden drop in cavity pressure and, in effect, an end to its capability to generate seismic signals. Thus the longer a positive pressure (i. e., greater than overburden) exists in the cavity, the longer will be the time during which cavity growth and motion can radiate energy into the earth and hence the greater the energy coupled into the seismic signals.

By extending the straight line in Fig. 59 one is able to read directly the value of E at Station 2BN for 20 tons at any depth of burst within the limits of a few meters to nearly complete containment.

Yield Dependence

The variation of PSD with yield for the components and resultants at Station 2BN is shown graphically in Figs. 27 through

30. These figures illustrate the good reproducibility of PSD for three different events.

In order to understand the yield dependence of the value of $\sum E$ for the cratering case, the depth of burst effect must be removed. This is done by using the results of the previous section and the curve from Fig. 59. The procedure is as follows. Values of $\sum E$ for all events are normalized to some standard depth (in this case the 0.5-ton optimum depth) by multiplying the measured $\sum E$ by the ratio of the 0.5-ton point to the actual depth of burst point. This new value or $\sum E'$ is the $\sum E$ which would result if the event were detonated at the shallower depth. The $\sum E'$ is independent of depth of burst within the limits mentioned in the previous section. If the measurement were made at Station 2BN for Pre-Gondola events this $\sum E'$ would also be independent of range. A plot of such events would give the yield-E dependence.

The calculated values for the 20-ton events are:

$$\begin{aligned}\sum E_A &= 16.9 \times 10^{-2} (7.7/151) \\ &= 8.65 \times 10^{-3} \text{ (Alfa Event)} \\ \sum E_C &= 6.34 \times 10^{-2} (7.7/64) \\ &= 7.62 \times 10^{-3} \text{ (Charlie Event)} \\ \sum E_D &= 20.3 \times 10^{-2} (7.7/214) \\ &= 7.8 \times 10^{-3} \text{ (Delta Event)}\end{aligned}$$

To calculate for the row charge (three 20-ton and two 40-ton charges), each charge must be treated separately and multiplied by its proportion of the total. Thus

$$\begin{aligned}\sum E &= 1.45 \left[2 \left(\frac{40}{140} \right) \left(\frac{7.7}{287} \right) + 3 \left(\frac{20}{140} \right) \left(\frac{7.7}{108} \right) \right] \\ &= 6.64 \times 10^{-2} \text{ (140-ton event)}\end{aligned}$$

These numbers are plotted in Fig. 60 along with $\sum E$ for the SD-1 Event, and a straight line fit to the points is made (for SD-1, $\sum E = \sum E'$). The slope of this line is $\alpha = 1.11$. If all of the variables except yield had truly been normalized out, a slope of 1.0 or less would be expected. Considering the few numbers of points used in the depth of burst curve, this close agreement is quite good. It is reasonably safe to conclude that the total energy scales as the first power of yield in this range, and that the difference (between 1.0 and 1.11) lies in the inaccuracy of the curve in Fig. 59.

Range Dependence

A comparison of the separate components at all stations is shown in Figs. 39 to 42 for the Bravo Event and in Figs. 43 to 46 for the 140-ton row charge. Agreement of the curves as a function of range is fair for Bravo and better for the 140-ton event. The best consistency is in the resultant shown in Fig. 46.

A plot of the peak energy density ($\text{PSD}(f)_{\text{max}}$) for each component and resultant vs range is shown in Fig. 51 for Bravo and in Fig. 52 for the 140-ton row charge. The lines are best fits to the peak resultant values. The attenuation slopes of 4.01 and 3.71 are in fair agreement with each other.

An excellent agreement results between the two events when E and $\sum E$ are plotted (Figs. 53 and 54). The two attenuation slopes for $\sum E$ are $\alpha = 3.55$ and $\alpha = 3.53$ for the two events (see the next section for a discussion of these values).

Attenuation of the energy in each frequency band is not made very clear by

PSD results. The attenuation slope for each frequency is shown in Fig. 55 for Bravo and in Fig. 56 for the 140-ton event for three components. The resultants from the two events are compared in Fig. 57.

Although there is good agreement between events it is still not clear why $\alpha(f)$ is not a simple function of frequency and why α decreases as frequency increases.⁸

Comparison of Analysis Methods

It is clear from the above discussion that the CFPV method reveals more about the nature of the incoming seismic signal than a simple peak velocity determination. Likewise the PSD method reveals even more information than CFPV, and the results appear to be more consistent with the mean deviation of various stations being smaller for this latter method.

An interesting and encouraging result is obtained by comparing $\sum E$ slopes to peak velocity slopes. Let us reason as follows: (1) the peak velocity, on the average (i. e., for many stations and events) will be proportional to the signal attenuation, and (2) average energy is proportional

to average velocity squared. It then follows that the slope of the peak velocity curve should be one half the slope of the energy curve. From the foregoing:

$$\begin{aligned} 1/2 \alpha \text{ (total energy, Bravo)} &= 1.76 \\ 1/2 \alpha \text{ (total energy, 140-ton)} &= 1.76 \\ \alpha \text{ (peak velocity, Bravo)} &= 1.54 \\ \alpha \text{ (peak velocity, 140-ton)} &= 1.64 \\ \alpha \text{ (peak velocity, average)} &\approx 1.6 \end{aligned}$$

Other investigators have found α 's for peak velocity ranging from 1.5 to 2.0 with a rather generally accepted average of about 1.8.^{1,6,8} Thus the α of 3.55 for energy attenuation seems to be an excellent number.

A comparison of $1/2 \alpha(f)$ from the resultant PSD(f) and α for the CFPV on the 140-ton event shows good agreement at nearly all frequencies (Fig. 58). Since these methods are different in approach, the results support the validity of each method in that they accurately describe the content of the signal. They do not explain why the high frequencies attenuate (apparently) more slowly than the low frequencies.

Conclusions

From the foregoing the following conclusions may be made:

1. Peak velocity, CFPV, and PSD are all valuable tools provided one understands their limitations and applicability. However, for consistency in describing the transmitted signal in spite of station differences, PSD is the best of the three methods. In fact, its good consistency in correlating with yield suggests two possibilities:

- a. This might be a valuable diagnostic tool to determine yields of underground explosions
- b. This technique might be applied to earthquake records and be the basis for an earthquake magnitude scale.

(In fact, I might even be so bold as to call this scale the "Power power earthquake magnitude scale"—albeit, somewhat facetiously).

2. The total station energy ($\sum E$) of the transmitted seismic signal over the ranges of 0.5 to 140 tons and probably higher varies as the first power of the yield.

3. Varying the absolute depth of burst affects the transmitted seismic signal at cratering depths to a marked extent. In terms of energy, a factor of 2 for a small change in depth of burst is not unusual and might be important in selecting a depth for a future cratering event.

4. The total station energy ($\sum E$) in a seismic signal over the intermediate range for frequencies of 0.5 to 20 Hz goes as the -3.55 power of range

$$\sum E = \sum E_0 R^{-3.55}.$$

5. The effect of geologic differences in transmission path and local geologic columns causes gross differences in the time dependent appearance of the ground motion. These geologic differences are not as effective in altering PSD or the total energy arriving at the station when the geologic and geophysical properties of various stations are similar. A conclusion as to what would be the result for large differences in transmission path and local geologic properties cannot be made on the basis of this work, and further study is needed.

References

1. D. V. Power, Intermediate Range Ground Motions: Project Pre-Gondola I, Lawrence Radiation Laboratory, Livermore, Rept. PNE-1105, May 1967.
2. A. J. Eardley, Structural Geology of North America, Chapter 5, (Harper and Row, New York, N. Y., 1962) 2nd ed.
3. D. L. Watson, Procedure for Recording Ground Motion Velocity from Underground Nuclear Explosions, Nevada Operations Office, Las Vegas, Rept. NVO-1163-93, August 1967.
4. R. F. Beers, Inc., Investigation of Salmon Ground Motions and Effects, Nevada Operations Office, Las Vegas, Rept. NVO-1163-51, April 1965.
5. R. B. Blackman and J. W. Tukey, The Measurement of Power Spectra, (Dover Publications, New York, N. Y., 1958).
6. Environmental Research Corp., Preliminary Interoceanic Canal Ground Motion Report, Nevada Operations Office, Las Vegas, Rept. NVO-1163-117, July 1967.
7. R. S. Bradley, High Pressure Physics and Chemistry, Vol. II (Academic Press, New York, N. Y., 1963), p. 228.
8. J. E. White, Seismic Waves; Radiation, Transmission, and Attenuation, Chapter 3, (McGraw-Hill Book Co., N. Y., 1965).

Appendix A

A Discussion of the Transmission of Seismic Signals and their Measurement

The most universally used method of determining the ground motion from an underground explosion is to measure with a transducer a dynamic coordinate of some finite part of the earth as a function of time. Ordinarily the coordinate is displacement, velocity, or acceleration. In theory any two may be obtained from a third by integration or differentiation. In practice this is difficult because of inherent noise, instrument drift, instabilities of numerical methods, etc. It is also usually not possible to measure all three directly due to the financial expense and instrument capabilities. The usual compromise is to use the best instrument suited for the magnitude of motions and to do the best one can with analysis techniques available. For the intermediate range (a few to a few hundred kilometers), velocity gauges are the usual choice.

The time-dependent motion that occurs at any given surface location is the result of a transmitted signal which has had a very complicated, and for the most part unknown, past. This motion is not one signal but many, each arriving via a separate path from the source. Thus there are direct arrivals traveling exclusively in the near surface material while other signals are reflected and refracted from the deeper layers of the earth's crust. In addition to various paths there are several modes of wave motion, such as compressional, shear, Rayleigh, and Love waves each traveling at different

velocities. Finally, for each path, there are numerous interfaces and impedance mismatches with attendant reflections and alterations in the signal. Certain geologic and geometric structures, particularly near the surface, may act as wave guides or resonating structures. Finally, the signal which the investigator obtains is not the ground motion but is the response of some mechanical system to that ground motion.

The total path a signal travels may be divided into four areas: (1) source, which for our case includes variations in the explosive (such as yield and immediate surrounding area including shape and volume of source cavity), the immediate surrounding earth material, and the relationship to the nearest interfaces and impedance changes, specifically depth of burst; (2) the so-called transmission path which extends to all the earth except those areas immediately surrounding the source and the recording stations; (3) the receiving site which may include a few to several hundred feet of surface material below and around the transducer; and (4) the transducer which includes itself and the problems associated with the recording, retrieval, and reduction of data.

If one wishes to study the effect of some variable upon the transmitted signal, all things should be held constant except that variable. This is not entirely possible since the so-called variables are not completely independent of each other. As

a specific example, a sine wave source S_1 of amplitude A_1 and frequency f_1 may be transmitted through some transmission path T_1 to a receiving site with amplitude R_1 . If now a new sine wave source S_2 of the same amplitude A_1 but new frequency f_2 is transmitted over the same path T_1 , one would expect a sine wave of amplitude R_1 and frequency f_2 to be received at the distant point. This however, will not be the case if T_1 transmits one frequency, say f_1 , better than another or f_2 . The transmission path may also have amplitude dependencies.

The problem is further complicated if the source is a complex of frequencies and amplitudes. It is a little bit like a photographer trying to figure out how much light to put on his subject when he doesn't know what his lens opening is or what speed film is in the camera.

It would seem to be almost hopeless to accomplish anything against such odds.

However some hope does exist. If the nonlinearities in the problem are made as small as possible they might be ignored. Since the Pre-Gondola series of events makes it readily possible to study the source, it is the uncertainties in the transmission path, local effects, and transducer effects which are of concern.

The transducer is the easiest problem. Although it is nonlinear below 1 Hz, its response is well known and understood. It has already been mentioned in body of the report that it was believed that the geology in northeastern Montana is very uniform. By choosing a radial path in a direction of little structural relief (in both surface and subsurface) and by selecting station locations over what appeared to be similar geologic columns it is possible to minimize the effects of local geology and transmission paths.

Appendix B

A Discussion of Comb Filter Peak Velocity and Vector Addition Analysis Techniques

A simple measure of a seismic signal is to measure the maximum amplitude without regard to its frequency. An improvement is to separate a time history into its frequency components and to measure the peak amplitude in each frequency.

To do this by analog methods requires a filter which passes only a single frequency and eliminates all others. Mathematically, the response of such a filter is represented by a Dirac-delta function. An infinite array of these filters would be required to determine the entire spectrum in a signal.

Obviously, a device with an infinite array of filters does not exist, but a finite array can be made to approximate it to a sufficient degree of accuracy. Filters exist which pass a given frequency with a ratio of 1.0 and, on either side of this center frequency, pass information with a ratio of less than 1.0. A series of such filters (called comb filters), set at appropriate frequencies, gives an approximation to the actual spectral content of a signal. This approximation is improved as the attenuation on either side of the center frequencies increases and as the number of filters increases.

It is necessary to have filters which span the frequency content of a seismic signal. Due to the inherent characteristics of large explosives the meaningful frequencies are below 20 Hz. Transducer characteristics further limit the recorded

signals to frequencies greater than some minimum. For the case of a 1-cycle velocity geophone the sensitivity drops off sharply below 1.0 Hz and seismic frequencies of less than 0.5 Hz are usually considered as "lost" to this type of instrument.

Let us return now to the method of measuring just the peak motion in a signal regardless of frequency. A mechanical-electrical transducer is usually constrained to a single degree of freedom in order to reduce the complexity of its behavior. However, a point in space has three degrees of freedom (three-translational coordinates) and a body in space has six degrees of freedom (three translational and three rotational coordinates). For motions in the "intermediate" range the rotational motions may be ignored as they are infinitesimal compared to the translational.

The standard transducer array measures motions in three directions which then comprise an orthogonal, rectangular coordinate system. This means that an arbitrary spatial motion is not measured directly. Each transducer measures only the component of motion parallel to its degree of freedom. To regain the actual motion one must transform back to the spherical coordinate system to obtain the magnitude (R) and the directional angles. This is done by the following well known relationships

$$\begin{aligned}
|\text{Res}| &= |\vec{x} + \vec{y} + \vec{z}| \\
&= |\hat{x}\hat{i} + \hat{y}\hat{j} + \hat{z}\hat{k}| \\
&= [(x \cdot x + y \cdot y + z \cdot z) \\
&\quad \times (\hat{i} \cdot \hat{i} + \hat{j} \cdot \hat{j} + \hat{k} \cdot \hat{k})]^{1/2} \\
&= (x^2 + y^2 + z^2)^{1/2} \\
\theta &= \cos^{-1} \left[\frac{x}{(x^2 + y^2)^{1/2}} \right] \\
\phi &= \tan^{-1} \left[\frac{(x^2 + y^2)^{1/2}}{z} \right]
\end{aligned}$$

In all of the above equations the variables x , y , z , Res , θ , and ϕ are functions of time and hence can be operated upon jointly only if time is the same for all variables in a given calculation. This is achieved readily if x , y , and z are recorded simultaneously on the same tape. All subsequent operations are done in a similar manner, and the time relationship between components is held fixed. However, in actual practice one complication arises due to the manner in which the data are digitized for these studies. The digitizer can read only one channel at a time; hence x , y , and z must be read sequentially as the tape passes over the head. This results in a small time difference ($\Delta\tau$) between x_i and y_i of 0.0005 sec for this

system. Although this is an exceedingly small error it can be made smaller still by digitizing x , y , z , y , x ; x , y , z , y , x ; x , etc. Thus the output is $x(t)$, $y(t + \Delta\tau)$, $z(t + 2\Delta\tau)$, $y(t + 3\Delta\tau)$, $x(t + y\Delta\tau)$, etc. Then

$$\begin{aligned}
x_i &= \frac{x(t_i) + x(t_i + 4\Delta\tau)}{2} \approx x(t_i + 2\Delta\tau) \\
y_i &= \frac{y(t_i + \Delta\tau) + y(t_i + 3\Delta\tau)}{2} \\
&\approx y(t_i + 2\Delta\tau)
\end{aligned}$$

$$z_i = z(t_i + 2\Delta\tau)$$

Since no periods anywhere near 0.005 are present in the data, x_i , y_i , and z_i are extremely accurate (indeed, much more accurate than necessary in this case; however, the computer code used for these studies was written so as to be much more generally applicable). This code was written for the IBM 7094 and provides three outputs:

1. A graphical plot of x_i , y_i , z_i , $|\text{Res}_i|$, $(\text{Res})^2$, θ_i and ϕ_i vs time scaled to proper values.
2. A printed output giving the actual numbers.
3. A digital tape suitable as input for the PSD code.

Appendix C

A Discussion of the Power Spectral Density Code

The power spectral density is a measure of the energy per unit frequency in a given time history and is a function of frequency. By definition then:

$$\text{PSD}(f) = \frac{\Delta E}{\Delta f}$$

and a measure of the total energy is given by

$$E = \int_0^{\infty} \frac{\Delta E}{\Delta f} df = \int_0^{\infty} \text{PSD}(f) df$$

= total energy.

In principle the $\text{PSD}(f)$ can be calculated with integral methods (see Ref. 5 for a complete discussion of theory). In practice one can not handle an integral directly by digital methods since it requires an infinite number of points in the calculation. There are several techniques utilizing a finite number of points which approximate the PSD. The method used here is the one suggested by Blackman and Tukey.⁵

The accuracy of this method is good but care must be taken in choosing the lag length (ΔT), the number of lags (N), and the time between successive data points in a given signal ($\Delta \tau$) all with respect to the frequencies present in the data. The data contain information primarily between 0.5 and 20.0 Hz, the low frequencies being filtered out by the mechanical response of the system and the high frequency noise being electronically filtered out. The parameters for this work done in this study were:

$$\Delta T = 0.01 \text{ sec}$$

$$\Delta \tau = 0.0025 \text{ sec}$$

$$N = 300$$

The equations given by Blackman and Tukey are as follows:

The auto covariance is given by

$$A_{\ell} = \frac{1}{I - \ell} \sum_{i=1}^{I-\ell} x_i x_{i+\ell}$$

for $\ell = 0, 1, \dots, N$; and I is the total number of data points in a record.

Then the power spectrum is given by

$$P_k = \frac{1}{N} \left[A_0 + A_N + 2 \sum_{m=1}^{N-1} A_m \cos \left(\frac{km\pi}{N} \right) \right]$$

for $k = 0, 1, \dots, N$

Since the above is an estimate, Blackman and Tukey recommend smoothing by the following process:

$$P'_0 = \frac{1}{2} (P_0 + P_1)$$

$$P'_N = \frac{1}{2} (P_{N-1} + P_N)$$

$$P'_k = \frac{1}{4} (P_{k-1} + P_{k+1}) + \frac{1}{2} P_k$$

Now P'_k is the approximate energy in a given frequency band. To obtain the energy density or $\text{PSD}(f)$ we must divide by the Δf or frequency band width, where

$$\Delta f = \left(\frac{1}{2} \right) \left(\frac{1}{\Delta T} \right) \left(\frac{1}{N} \right)$$

Then

$$\text{PSD}(f) = P'_k (2\Delta TN)$$

The total energy in a component then is

$$E = \int_0^\infty \text{PSD}(f) df \approx \sum_{k=0}^N \frac{P'_k \Delta f}{\Delta f} = \sum_{k=0}^N P'_k$$

Since the PSD is calculated on three mutually orthogonal coordinates (x, y, and z) the energy in each coordinate is mutually isolated and independent of the other two coordinates. Thus one method of calculating the resultant PSD(f) is simply to sum three components or

$$\text{PSD}(f)_{\text{resultant}} = \sum \text{PSD}(f)_i$$

for i = x, y, and z.

A measure of the total energy for all three components is just the sum of E or

$$\sum E = \sum E_i \quad \text{for } i = x, y, \text{ and } z,$$

or

$$\sum E = \sum_{k=0}^N (\text{PSD}(f)_{\text{resultant}}) \Delta f.$$

The code (PSD) developed to do the above calculations was written for the CDC 3600 computer and utilized a tape written by the IBM 7094 from the VECTOR code. The output is in two forms: visual (PSD(f) vs frequency plots) and digital (numeric printout).

DISTRIBUTION LIST
(TID-4500, Category UC-35)

No. Copies

1 AEC ALBUQUERQUE OPERATIONS OFFICE
1 AEC BETHESDA TECHNICAL LIBRARY
25 AEC DIVISION OF PEACEFUL NUCLEAR EXPLO-
SIVES
1 AEC LIBRARY, WASHINGTON
1 AEC MISSION TO THE IAEA
5 AEC NEVADA OPERATIONS OFFICE
1 AEC NEW YORK OPERATIONS OFFICE
1 AEC PATENT OFFICE
5 AEC SAN FRANCISCO OPERATIONS OFFICE
1 AEC SAVANNAH RIVER OPERATIONS OFFICE
1 AEC SCIENTIFIC REPRESENTATIVE, BELGIUM
1 AEC SCIENTIFIC REPRESENTATIVE, ENGLAND
1 AEC SCIENTIFIC REPRESENTATIVE, JAPAN
1 AEROSPACE CORPORATION, SAN BERNARDINO
(AF)
1 AIR FORCE AERO PROPULSION LABORATORY
(APE)
1 AIR FORCE FOREIGN TECHNOLOGY DIVISION
1 AIR FORCE INSTITUTE OF TECHNOLOGY
1 AIR FORCE SCHOOL OF AEROSPACE MEDICINE
1 AIR FORCE WEAPONS LABORATORY
1 AMES LABORATORY (AEC)
1 ARGONNE NATIONAL LABORATORY (AEC)
8 ARMY ABERDEEN PROVING GROUND
1 ARMY CHIEF OF ENGINEERS
1 ARMY ELECTRONICS COMMAND
1 ARMY ENGINEER DIVISION
5 ARMY ENGINEER NUCLEAR CRATERING GROUP
6 ARMY ENGINEER WATERWAYS EXPERIMENT
STATION
1 ARMY MATERIEL COMMAND
1 ARMY MEDICAL FIELD SERVICE SCHOOL
1 ARMY MEDICAL RESEARCH UNIT
1 ARMY MOBILITY EQUIPMENT RESEARCH AND
DEVELOPMENT CENTER
1 ARMY NUCLEAR DEFENSE LABORATORY
1 ARMY PICATINNY ARSENAL
1 ARMY ROCKY MOUNTAIN ARSENAL
1 ARMY SURGEON GENERAL
1 ARMY WALTER REED MEDICAL CENTER
1 ATOMIC POWER DEVELOPMENT ASSOCIATES, INC.
(AEC)
2 ATOMICS INTERNATIONAL (AEC)
1 BABCOCK AND WILCOX COMPANY, WASHINGTON
(AEC)
2 BATTELLE MEMORIAL INSTITUTE (AEC)
1 BATTELLE-NORTHWEST (AEC)
1 BROOKHAVEN NATIONAL LABORATORY (AEC)
2 BUREAU OF MINES, BARTLESVILLE (INT)
1 BUREAU OF MINES, DENVER (INT)
1 BUREAU OF MINES, LARAMIE (INT)
6 BUREAU OF RECLAMATION (INT)
1 DEPARTMENT OF AGRICULTURE NATIONAL
LIBRARY
1 DOD DASA LIVERMORE
1 DOD DASA RADIOBIOLOGY RESEARCH INSTITUTE
1 DOD DASA SANDIA
1 DOD DASA WASHINGTON
1 DU PONT COMPANY, AIKEN (AEC)
1 DU PONT COMPANY, WILMINGTON (AEC)
1 EG&G, INC., ALBUQUERQUE (AEC)
1 EG&G, INC., LAS VEGAS (AEC)
5 EL PASO NATURAL GAS COMPANY
8 ENVIRONMENTAL RESEARCH CORPORATION
(AEC)
1 ENVIRONMENTAL RESEARCH CORPORATION,
LAS VEGAS (AEC)
1 ENVIRONMENTAL SCIENCE SERVICES
ADMINISTRATION, LAS VEGAS (COMM.)
1 ENVIRONMENTAL SCIENCE SERVICE
ADMINISTRATION, MARYLAND (COMM.)

No. Copies

1 FRANKFORD ARSENAL (P-D LABS.)
1 GENERAL DYNAMICS/FORT WORTH (AF)
1 GENERAL ELECTRIC COMPANY, CINCINNATI
(AEC)
1 GENERAL ELECTRIC COMPANY, SAN JOSE (AEC)
1 GEOLOGICAL SURVEY, DENVER
1 GEOLOGICAL SURVEY, FLAGSTAFF (INT)
1 GEOLOGICAL SURVEY, MENLO PARK (INT)
1 GEOLOGICAL SURVEY (PECORA) (INT)
1 GULF GENERAL ATOMIC INCORPORATED (AEC)
2 HOLMES AND NARVER, INC. (AEC)
1 HUGHES AIRCRAFT COMPANY, FULLERTON
(ARMY)
1 INSTITUTE FOR DEFENSE ANALYSIS (ARMY)
1 ISOTOPIES, INC. (AEC)
1 JET PROPULSION LABORATORY (NASA)
1 LAWRENCE RADIATION LABORATORY,
BERKELEY (AEC)
4 LAWRENCE RADIATION LABORATORY,
LIVERMORE (AEC)
2 LOS ALAMOS SCIENTIFIC LABORATORY (AEC)
5 LOVELACE FOUNDATION (AEC)
1 MATHEMATICA (AEC)
1 MUESER, RUTLEDGE, WENTWORTH AND
JOHNSTON (AEC)
1 MUTUAL ATOMIC ENERGY LIABILITY
UNDERWRITERS (AEC)
1 NASA JOHN F. KENNEDY SPACE CENTER
1 NATIONAL BUREAU OF STANDARDS (LIBRARY)
1 NATIONAL INSTITUTES OF HEALTH (HEW)
1 NATIONAL REACTOR TESTING STATION (INC)
(AEC)
1 NAVY ATOMIC ENERGY DIVISION
1 NAVY OFFICE OF NAVAL RESEARCH (CODE 422)
2 NAVY ORDNANCE LABORATORY
1 NAVY ORDNANCE SYSTEMS COMMAND
1 NAVY POSTGRADUATE SCHOOL
1 NAVY RADIOLOGICAL DEFENSE LABORATORY
1 NAVY SHIP SYSTEMS COMMAND HEADQUARTERS
NRA, INC.
4 OAK RIDGE NATIONAL LABORATORY (AEC)
1 OCEANOGRAPHIC SERVICES, INC. (AEC)
1 OHIO STATE UNIVERSITY (OCD)
3 PUBLIC HEALTH SERVICE, LAS VEGAS (HEW)
1 PUBLIC HEALTH SERVICE, MONTGOMERY (HEW)
1 PUBLIC HEALTH SERVICE, ROCKVILLE (HEW)
1 PUBLIC HEALTH SERVICE, WINCHESTER (HEW)
1 PUERTO RICO NUCLEAR CENTER (AEC)
1 PURDUE UNIVERSITY (AEC)
1 RADIOPTICS, INC. (AEC)
2 REYNOLDS ELECTRICAL AND ENGINEERING
COMPANY, INC. (AEC)
4 SANDIA CORPORATION, ALBUQUERQUE (AEC)
1 SANDIA CORPORATION, LIVERMORE (AEC)
1 SOUTHWEST RESEARCH INSTITUTE (AEC)
1 STANFORD UNIVERSITY (AEC)
1 TENNESSEE VALLEY AUTHORITY
1 UNION CARBIDE CORPORATION (ORGD) (AEC)
1 UNIVERSITY OF CALIFORNIA, DAVIS,
TALLEY (AEC)
1 UNIVERSITY OF MICHIGAN (VESIAC) (ARMY)
1 UNIVERSITY OF ROCHESTER (KAPLON) (AEC)
1 UNIVERSITY OF TENNESSEE (AEC)
1 UNIVERSITY OF WASHINGTON (AEC)
1 WASHINGTON STATE UNIVERSITY (AEC)
1 WESTINGHOUSE ELECTRIC CORPORATION,
MC KENNA (AEC)
66 AEC DIVISION OF TECHNICAL INFORMATION
EXTENSION
25 CLEARINGHOUSE FOR FEDERAL SCIENTIFIC
AND TECHNICAL INFORMATION